UNIVERSITÄT HAMBURG
DEPARTMENT PHYSIK

Measurement of the Z Boson production with the ATLAS Experiment at the LHC

Dissertation
zur Erlangung des Doktorgrades
des Department Physik
der Universität Hamburg

vorgelegt von
Mikhail Karnevskiy
aus Leningrad

Hamburg
2012

Gutachter der Dissertation:	PD. Dr. Alexandre Glazov PD. Dr. Thomas Schörner-Sadenius
Gutachter der Disputation:	PD. Dr. Alexandre Glazov Prof. Dr. Johannes Haller
Datum der Disputation:	24. Mai 2012
Vorsitzender des Prüfungsausschusses:	Prof. Dr. Caren Hagner
Vorsitzender des Promotionsausschusses:	Prof. Dr. Peter Hauschildt
Leiterin des Departments Physik:	Prof. Dr. Daniela Pfannkuche
Dekan der MIN-Fakultät:	Prof. Dr. Heinrich Graener

Abstract

The inclusive and single differential in Z boson rapidity bins cross sections for the $pp \to Z/\gamma^* \to e^+e^-$ process are measured with the ATLAS detector at the LHC. The data are taken in 2010 at a center-of-mass energy of $\sqrt{s} = 7$ TeV and correspond to an integrated luminosity of 36.2 pb^{-1}. Several types of systematic uncertainties, including pileup effects, efficiency corrections and differences in Monte-Carlo generators are considered. The dominant uncertainty comes from the electron identification efficiency correction. All results are in agreement with the muon channel analysis and with theoretical predictions.

The calibration of the ATLAS electromagnetic calorimeter using $Z \to e^+e^-$ events is performed for all sub-detectors up to $|\eta| = 4.9$ in bins of electron η. Several tests of the calibration method as well as studies of the systematic uncertainties are presented. Total uncertainties of the calibration factors do not exceed 2% for the region where the cross section is measured.

The electron identification and isolation efficiency measurements are studied using a tag-and-probe method. The results are in agreement with the other ATLAS measurement. The dominant systematic uncertainty, which comes from the background subtraction, is estimated using several fit methods.

Zusammenfassung

Die vorliegende Arbeit stellt eine Messung des inklusiven und differenziellen Wirkungsquerschnitts der Reaktion $pp \to Z/\gamma^* \to e^+e^-$ mit dem ATLAS-Detektor am LHC vor. Der differenzielle Wirkungsquerschnitt ist als Funktion der Z-Boson-Rapidität bestimmt worden. Die zugrundeliegenden Daten wurden bei einer Schwerpunktsenergie von $\sqrt{s} = 7\,\text{TeV}$ im Jahr 2010 aufgezeichnet. Sie entsprechen einer integrierten Luminosität von $36{,}2\,\text{pb}^{-1}$. Systematische Unsicherheiten von z.Bsp. Pileup-Effekten, Effizienzunsicherheiten und Unterschiede in verschiedenen Monte-Carlo-Generatoren wurden berücksichtigt. Den grösten Beitrag stellt die Unsicherheit auf die Identifikationseffizienzkorrektur dar. Die Ergebnisse dieser Arbeit sind mit den Resultaten aus der Analyse des Myon-Kanals sowie theoretischen Vorhersagen in Übereinstimmung.

Weiterhin wurde das elektromagnetische Kalorimeter des ATLAS-Dektors, inklusive aller Subdetektoren bis zu einer Rapidität von $|\eta| = 4{,}9$, mit Hilfe von $Z \to e^+e^-$-Ereignissen kalibiert. Methoden zur Verifikation der Kalibration sowie die Bestimmung der systematischen Unsicherheiten werden präsentiert. Die Gesamtunsicherheit der Kalibrationsfaktoren ist im Bereich der Wirkungsquerschnittsmessung nie gröser als $2\,\%$.

Zur Bestimmung der Identifikations- und Isolationseffizienzen wurden die $Z \to e^+e^-$-Ereignisse mit einer Tag-and-Probe-Methode untersucht. Die Ergebnisse sind mit den offiziellen ATLAS-Messungen kompatibel. Weiterhin wurde der Untergrund, welcher den grösten Beitrag zur systematischen Unsicherheit liefert, mit verschiedenen Fit-Methoden bestimmt.

Contents

CHAPTER 1

Thesis overview

of the Parton Distribution Functions (PDFs) determined based on HERA measurements in absolute four momentum transfer squared (Q^2).

The prediction of the Z cross sections as a function of boson rapidity at the LHC requires an extrapolation of the Parton Distribution Functions (PDFs) determined based on HERA measurements in absolute four momentum transfer squared (Q^2). Thus the measurement of the cross sections for the process $pp \to Z/\gamma^* \to e^+e^-$ is a test of the validity of the QCD evolution into the region of high Q^2 at small Bjorken x. Also it provides a check of the PDFs estimated using HERA data.

Experimentally, the signature of the $Z \to e^+e^-$ process is quite clear with a small background contamination. The electron pair from this process can be used for the off-line calibration of the ATLAS electromagnetic (EM) calorimeter.

1.1 Thesis organization

This thesis summarizes measurement of the Neutral Current (NC) Drell-Yan cross section in the electron channel. The data were collected with the ATLAS detector at the LHC in 2010. Monte Carlo (MC) simulations were used for acceptance corrections.

This thesis shows a comparison of the predictions based on PDFs obtained using HERAPDF 1.0 and others with the experimental data. The basics of the cross-section measurement are presented, using a combined efficiency and acceptance correction which accounts for the higher order QED and finite resolution effects. New methods are introduced for the calibration of the EM energy scale and for the determination of efficiencies. Finally, the extension of the Z boson measurement to the forward region with the rapidity range of $|y_Z| < 3.6$, corresponding to an x range from 0.00036 to 0.48, is presented.

The thesis is organized as follows:

Chapter 2. Brief introduction to the SM, to pp physics and to Z boson production is given. This chapter also provides a motivation for the $Z \to e^+e^-$ cross-section measurement.

Chapter 3. The CERN accelerator complex with LHC is shortly described.

Chapter 4. Description of the ATLAS detector and its relevant sub-components is presented. The physics program of the ATLAS experiment is outlined. The ATLAS data acquisition system and computing strategy are discussed as well.

Chapter 5. The ATLAS data with their luminosity which were collected in 2010 and used for this thesis are described.

Chapter 6. The MC samples obtained with different MC generators are discussed. The full chain of MC production in the ATLAS experiment is shown. A study of the pileup effect and reweighting of the Z boson transverse momentum $p_{T,Z}$ is presented. These studies contribute to paper of the measurement of the Z boson transverse momentum [1].

Chapter 7. The method of the cross-section extraction and the binning definition are presented. Studies of bin-migration effects are performed.

Chapter 8. The ATLAS event reconstruction for EM objects, which includes trigger performance, electron reconstruction and identification, is described.

Chapter 9. The event selection for $Z \to e^+e^-$ analysis is discussed. Central-Central (CC) and Central-Forward (CF) selections are introduced.

Chapter 10. The analysis framework which was developed for presented analysis is described.

Chapter 11. Studies of the background are presented. Several methods for background estimation are discussed.

Chapter 12. The method of the off-line calibration of the EM calorimeter is explained and calibration results are presented. The systematic uncertainties of the calibration are discussed as well. Resolution of the EM calorimeter is estimated. Presented calculations contribute to electron performance paper [2].

Chapter 13. The electron trigger, identification, reconstruction and isolation efficiencies are described. Measurements of the isolation and identification efficiencies are performed and comparisons with the official ATLAS prescription are presented.

Chapter 14. Inclusive and single differential cross-section measurements in bins of di-electron rapidity are presented. The background estimation, efficiency determination, acceptance measurement and systematic uncertainties are discussed. The differential cross sections in different channels are combined and compared with theoretical predictions. The presented measurement contribute to the ATLAS paper of the inclusive W and Z cross-section measurement [3].

Chapter 15. A summary of the main results of this thesis is given.

CHAPTER 2

Theoretical introduction

First section of this chapter gives an introduction to the Standard Model (SM) of particle physics. Theory of high energy pp collisions in parton model approximation is shortly described in the next section. Two last sections describe a production and decay of Z bosons at the LHC and show a Leading Order (LO) calculation of the $Z \to l^+l^-$ cross section.

2.1 The Standard Model

The SM of particle physics describes the matter in terms of fundamental particles and their interactions. There are two classes of fundamental particles: fermions and bosons. Fermions (e.g. electrons) are particles which have half-integer spin and describe the matter part of the theory. Bosons (e.g. photons) are integer-spin particles. Up to now, only gauge bosons (in a list of fundamental particles), which mediate the fundamental interactions [4], were found. However, the SM predicts also a Higgs boson, which is necessary for consistency of the theory. The list of fundamental particles with their masses, electric charges, spins and third components of weak isospin, I_3 is presented in Tab. 2.1.

The interaction of the fundamental particles is governed by four fundamental interactions: the gravitational, electromagnetic (EM), weak, and strong. The SM consistently describes EM, weak and strong interactions. The gravitation could not yet be included into this model. However, since the gravitation is weaker by ~ 40 orders of magnitude than the EM interaction for energies achieved experimentally, it can be neglected. The fundamental fermions which can interact via the strong force are called quarks; the others are called leptons.

The mathematical concept which is used to describe the behavior of fundamental particles is a quantum field theory. A first significant attempt was performed by P. Dirac, who suggested a Lorentz-invariant extension [5] of the Schrödinger equation. It can be expressed by the Lagrange density for free particles with mass m,

$$L = i\Psi\gamma_\mu\partial^\mu\Psi - m\bar{\Psi}\Psi, \tag{2.1}$$

where Ψ is a four-dimensional object, called spinor, γ^μ are the Dirac matrices, and m is the rest mass of the fermion. The application of the Euler-Lagrange formalism to Eq. 2.1 leads to

Particle	mass [MeV]	charge [e]	spin [$\hbar$]	I_3
Quarks				
u	2.4	2/3	1/2	1/2
d	4.8	-1/3	1/2	-1/2
c	1.27×10^3	2/3	1/2	1/2
s	104	-1/3	1/2	-1/2
t	171.2×10^3	2/3	1/2	1/2
b	4.2×10^3	-1/3	1/2	-1/2
Bosons				
γ	0	0	1	
g	0	0	1	
Z^0	91.2×10^3	0	1	
$W^{\pm}$	80.4×10^3	± 1	1	
Leptons				
e	0.511	1	1/2	-1/2
μ	105.7	1	1/2	-1/2
τ	1.777×10^3	1	1/2	-1/2
ν_e	$< 2.2 \times 10^{-6}$	0	1/2	1/2
ν_μ	< 0.17	0	1/2	1/2
ν_τ	< 15.5	0	1/2	1/2

Table 2.1: The list of fundamental particles with their masses, electric charges, spins and third components of weak isospin, I_3.

the Dirac equation for non-interacting particles:

$$(\gamma^\mu p_\mu - m)\Psi(x) = 0, \tag{2.2}$$

where p_μ is the momentum operator $i\partial_\mu$. The Dirac equation describes relativistic spin-$\frac{1}{2}$ particles and predict the existence of anti-matter. In order to allow the creation and annihilation of particles, a quantization of the field Ψ is needed. This leads to a theory of free fermions, i.e. fermions which do not interact.

The next is the inclusion of interactions. It is believed nowadays that the so-called gauge-theories form the basis of the connection between particles and their interactions. The gauge theory is a type of field theory in which the Lagrangian is invariant under a continuous group of local transformations. A simple example of this transformation can be presented by the local U(1) symmetry group, which leads to the following transformation:

$$\Psi(x) \rightarrow e^{i\alpha(x)}\Psi(x). \tag{2.3}$$

Since all observable values are real, the physics theory should not depend on complex phases like $e^{i\alpha(x)}$. Therefore it would be naturally to require that the Lagrange density in Eq. 2.1 is

invariant under the transformation Eq. 2.3. This assumption leads to

$$L = \bar{\Psi}(i\gamma_\mu \partial^\mu - m)\Psi + e\bar{\Psi}\gamma_\mu A^\mu \Psi - \frac{1}{4} F_{\mu\nu} F^{\mu\nu} \tag{2.4}$$

with $F_{\mu\nu} = \partial_\mu A_\nu - \partial_\nu A_\mu$. A vector field A_μ had to be introduced to achieve this invariance, i.e. the local gauge symmetry. The term $e\bar{\Psi}\gamma_\mu A^\mu \Psi$ represents the interaction of the fermion field Ψ with the vector field A_μ. The term $F_{\mu\nu}F^{\mu\nu}$ is the kinetic energy of the vector field and has the same structure as in Maxwell's equation of EM interactions. The Lagrange density in Eq. 2.4 is locally $U(1)$-gauge invariant. A canonical quantization [6] of the fields Ψ and A_μ leads to a theory, called Quantum Electro-Dynamics (QED), which describes the interaction of fermions via the exchange of the quanta of the EM field A_μ. These quanta are known as photons [7]. Since the theory does not contain a mass term $m^2 A_\mu A^\mu$, the photon must be a massless gauge boson in the theory.

The theory of strong interactions, called Quantum-Chromo Dynamics (QCD) is based on a locally $SU(3)$-gauge invariant Lagrange density [8] and describes the interactions between quarks and gluons which make up hadrons. Each quark [9–11] is a triplet of the QCD gauge group, which implies three quantum numbers (which play the role of a charge of the strong interaction) called red, blue and green. The gauge bosons in QCD are called gluons. Since the $SU(3)$ is a non-Abelian group, they carry color charges themselves (see Tab. 2.1). As a consequence, the gluons do not only interact with quarks, but also among themselves. It is believed nowadays that the self-interaction can explain what is commonly known as a feature of the QCD that is confinement [12]. Confinement describes the fact that color-charged objects cannot be observed individually but only in combinations, which are color-neutral. Colorless objects consisting of one quark and one anti-quark are called mesons, objects consisting of three quarks are called baryons (e.g. proton, neutron).

The unification of theories of the EM and weak force [13], requiring a $SU(2)\times U(1)$ invariant Lagrange density, leads to an isotriplet of vector fields W^i_μ with a coupling strength g and a single vector-field B^0_μ with a coupling strength g'. The bosons, which correspond to these fields are massless, which is inconsistent with the experimental observations.

The masses of the gauge bosons of the weak interaction introduce a theoretical problem, since writing a mass term in the Lagrange density would break its gauge invariance, which is an essential feature of the theory. A solution of this problem was formulated by Higgs and Kibble, and is based on a spontaneous breaking of the electroweak (EW) gauge symmetry [14].

The spontaneous symmetry breaking causes the W^0 and B^0 bosons to coalesce together into two different bosons (the Z^0 boson and the γ), and W^1 and W^2 into $W^\pm$ as follows:

$$\gamma = B^0 \cos\theta_W + W^0 \sin\theta_W \qquad Z^0 = -B^0 \sin\theta_W + W^0 \cos\theta_W,$$
$$W^\pm = \frac{W^1 \mp iW^2}{\sqrt{2}}, \tag{2.5}$$

where θ_W is the so-called weak mixing angle ($\sin^2\theta \sim 0.231$ [15]). The predicted Higgs-field leads to a dynamical mass generation of the W and Z bosons. The experimental values of W

and Z boson masses are 80.398 GeV and 91.1876 GeV [15][1].

The photon field and the Z boson field can be interpreted as an orthogonal combination of the two neutral gauge fields, which correspond to bosons W^0 and B_0. The corresponding charge of the $SU(2)$ group is called weak isospin and labeled with I. The charge of the $U(1)$ group is called weak hyper-charge and labeled with Y. The electric charge can be defined by these terms as $Q = I^3 + \frac{Y}{2}$. Z and W bosons carry a weak-charge themselves and therefore do not only interact with fermions but also among themselves.

The local $SU(3)_C \times SU(2)_L \times U(1)_Y$ gauge symmetry is an internal symmetry that essentially defines the SM, theory which describes the EW and strong interaction. Here C denote the color charge, L shows that only left handed fermion included in the SM, and Y stands for the electroweak hyper-charge.

The fermions of the SM are classified into six quarks and six leptons plus the corresponding anti-particles. They can be grouped into three generations, which transform identically under the gauge groups but differ in mass. The particles of the second and third generations decay via the weak interaction in particles of the first generation. The quantum numbers of the quarks and leptons and their masses are shown in Tab. 2.1.

One approach to calculate the interaction of particles in the framework of the SM is by using the perturbation theory. The expansion parameters for the perturbation theory are the coupling constants of the chosen interaction. Perturbation theory can be successfully applied to the EW part of the theory, since corresponding dimensionless coupling constant are enough small and each next order provide a small correction to the previous orders. This is in general not justified for the QCD due to its large coupling constant. The dimensionless coupling constant of the strong interaction $\alpha_s = \frac{g_s^2}{4\pi}$ is order of 1, which is much higher than the dimensionless coupling constant of the EM or the weak interaction at the energy of interaction order of 1 GeV. In particular, the confinement effect cannot be described by perturbation theory and so far no other approach has been proven to result in a successful theoretical description of this effect.

A further interesting property of the SM is the dependence of the coupling constants on the energy scale Q^2 of the interaction. Fig 2.1 schematically illustrate behavior of the coupling constant α_s of QCD, which vanishes at high Q^2. When the energy scale becomes order of several GeV or higher,α_s becomes small enough for perturbative calculations [16].

Soon after the formulation of QED it was discovered that divergent integrals appear [17] in perturbative calculations. A solution to this problem is a technique called renormalization: physical quantities can be defined in a way that emerging infinities are canceled by appropriate counter terms. It was proven by Gerardus 't Hooft that this procedure can be successfully applied in all gauge theories [18]. This is the reason why it is crucial that the masses of the weak vector bosons are generated dynamically and not by just inserting their masses in the corresponding Lagrangian, which would destroy the gauge invariance.

[1] These bosons are so-called resonance particles. They have a very short time of life (order of 10^{-25} sec), where the uncertainty principle $\Delta T \Delta E > h$ becomes significant. These particles characterized by not only mass but also a so-called full width $\Gamma = \frac{h}{T_{\text{life time}}}$, which is 2.1 GeV for W and 2.5 GeV for Z.

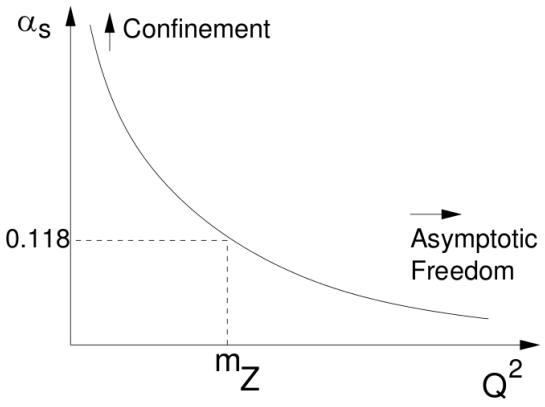

Figure 2.1: Schematic illustration of the dependence of the coupling α_s of the strong interaction on Q^2. Region of high Q^2 corresponds to low coupling of strong interaction, that can be interpreted as asymptotic freedom. Calculations can be done perturbatively, in this region.

The SM has been extensively tested in many experiments. Not a single serious contradiction has been discovered so far and hence it is one of the best theories in the history of physics. Nevertheless, it is believed that the SM cannot be the final theory of particle physics, because of several questions and problems. The first problem is an inclusion of the gravitational force. In addition, cosmological observation suggest presence of the so-called dark matter and dark energy which are not accounted in the SM. The existing of the Higgs boson is still unconfirmed, however it could be clarified with new LHC data.

2.2 Theory of pp collisions

A proton-proton collision at very low energies can be approximately described as an elastic scattering of two electrically charged extended objects. At higher energies, the inner structure of the proton becomes visible and can be investigated.

Since the proton is not a fundamental particle, the perturbative approach, which was shortly described in the previous section, can not be applied to calculations of proton-proton collisions. However, when the transferred squared momentum Q^2 in a collision experiment is much larger than that in the interaction between quarks (or simply larger than the rest mass of the proton), collisions can be described by so-called parton model (Feynman [19]). In this model, the proton consist of a collection of so-called "partons" (quarks and gluons). Additionally, the proton is in a reference frame where it has infinite momentum – an approximation which is valid in high-energies collision. Thus, the motion of patron is slowed by time dilation, and the hadron charge distribution is Lorentz-contracted, so that incoming partons will be scattered "instantaneously and incoherently" (they do not interact among themselves during the process of scattering).

Each parton carries a fraction x of the hadron momentum. To be precise, there is a certain probability of finding an individual parton f with momentum xp (p is the proton momentum). This probability can by denoted as $q_f(x)$. The functions $q_f(x)$ are called Parton Distribution

Functions (PDFs). Within this model, the proton-proton scattering can be considered as an elementary scattering of the partons weighted with q_f.

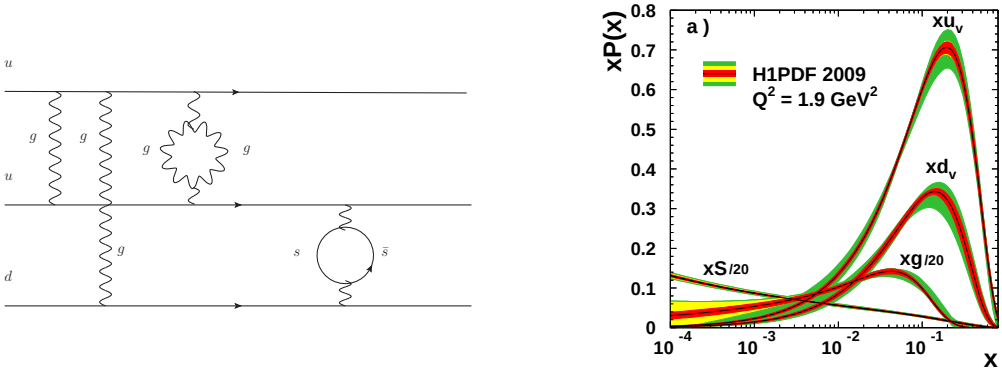

Figure 2.2: Left: Schematic illustration of three valence quarks forming a proton and interacting via the exchange of gluons. Quark anti-quark pairs can also appear as a loop on this diagram. Right: Parton distributions as determined by the H1PDF 2009 QCD fit at $Q^2 = 1.9$ GeV^2 [20] the gluon and sea-quark densities are downscaled by a factor 0.05.

The quarks which determine the quantum numbers of hadrons are the so-called "valence" quarks (uud in the case of the proton). Strong interactions between the partons lead to an additional production of gluons and quark-anti-quark pairs (see Fig. 2.2 left). Hence, the proton consists not only of three valence quarks, but also of a "sea" of further gluons and quarks. It is not yet possible to calculate the PDFs for the proton by perturbative approach and hence the knowledge of the PDFs relies (mainly) on deep inelastic scattering experiments. An illustration of an actual measurement of the PDFs for the proton is shown in Fig. 2.2, right.

The description of the pp collision can be conceptually divided into several stages, as illustrated in Fig. 2.3. The hard scattering describes the actual sub-process between two partons. The calculation of this process can be performed by perturbation theory at so-called tree-level, and in some cases also at higher orders.

Since the partons are electrically and/or color charged, they are accompanied by emission of gluons and photons both before and after the boson vertex giving rise to initial and final state parton showers, respectively. Corresponding corrections can be calculated perturbatively or, using the DGLAP evolution equations, with parton shower approach [21]. The shower evolution is stopped when reaching a fixed energy scale of the branching parton, which is usually about 1 GeV, i.e. well above the confinement regime.

When the energy of the particles decreases below 1 GeV the so-called hadronization is started. In this process colorless hadrons are formed from colored objects.

2.3 Z boson production in pp collisions

Z boson production in high energy pp collision can be mainly described by the Drell-Yan mechanism. In the Drell-Yan [4, 22] mechanism one quark from one of the protons, and an anti-quark from the other annihilate into a vector boson (photon, W or Z) with a large

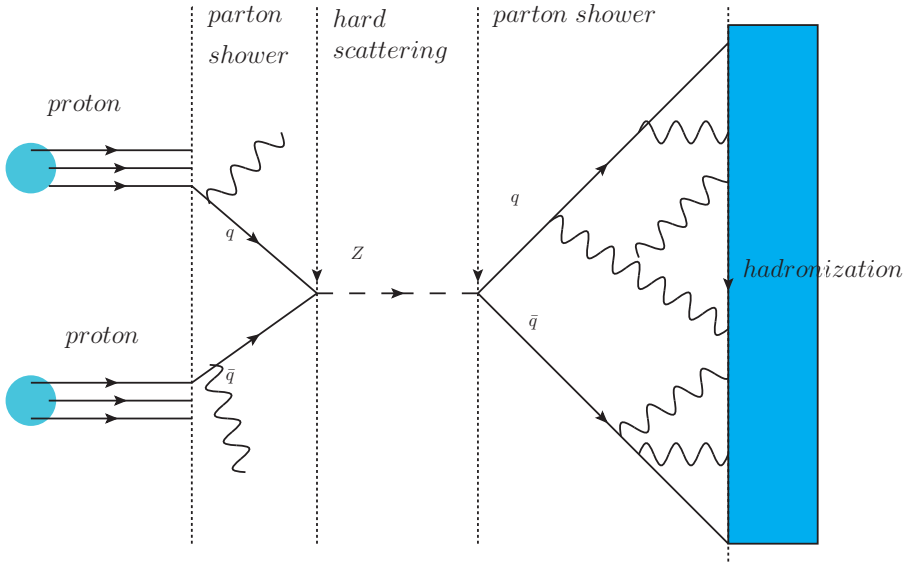

Figure 2.3: Hard scattering process of two partons producing a Z boson with a decay into two quarks, which are subsequently decaying into color-neutral hadrons (hadronization). The figure shows conceptual division of the proton-proton interaction into initial and final state radiation, hard scattering process and hadronization.

invariant mass squared (see Fig. 2.4). The vector boson subsequently decays into a lepton pair. Symbolically this process can be written as: $q\bar{q} \to (Z/\gamma)X \to l^+l^-X$ or $q\bar{q} \to W^\pm X \to l^\pm \nu X$.

If we denote momentum of the protons p_1, p_2 and fraction of the proton momentum carried by partons x_1, x_2 then

$$Q^2 = (x_1 p_1 + x_2 p_2)^2 = M^2_{Z,W,\gamma} \tag{2.6}$$

where M is the invariant mass of the boson. The total energy squared of the hadron-hadron collision is $s = (p_1 + p_2)^2$. Therefore, neglecting hadron masses, Eq. 2.6 can be rewritten as $Q^2 \simeq x_1 x_2 s$.

The variable Q^2 is not the only one that can be singled out to analyze Drell-Yan scattering. Another commonly used variable is the so-called rapidity, which is a Lorentz-invariant for boosts along the colliding particles z-direction and can be defined in terms of observable variables by

$$y = \frac{1}{2} \log \frac{E + p_z}{E - p_z}, \tag{2.7}$$

where E is the overall energy of the particle and p_z is the momentum of the particle in z-direction.

In LO approximation x can be written as $x_{1,2} = Me^{\pm y}/\sqrt{s}$, where $s = 4E_p^2$ is the center-of-momentum system (cms) energy squared. Therefore one may represent the kinematic ranges of deep inelastic scattering experiments and Drell-Yan measurements in a common x, Q^2 plane as it is illustrated in Fig. 2.5. The kinematic range of the Z and W measurements is extended towards lower x by the LHC due to the large cms.

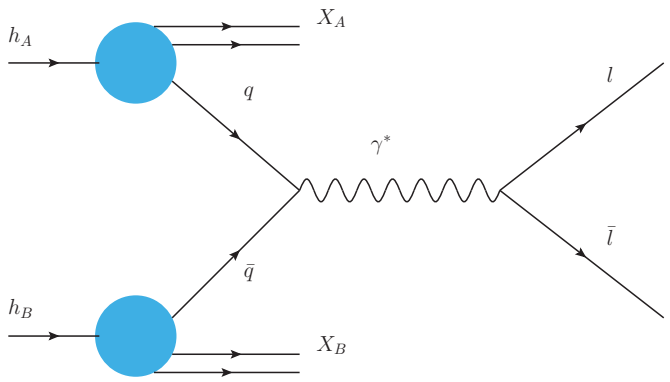

Figure 2.4: Drell-Yan process: a quark from one hadron and an anti-quark from the other hadron annihilate into a vector boson (photon, W or Z) with a large invariant mass squared. The vector boson subsequently decays into a lepton pair. Quarks of each proton do not interact among themselves.

The minimum rapidity y is equal to $y = \ln(2E_p/M) = 4.34$ for $M = M_Z$ for a beam energy of 3.5 TeV, corresponding to x values of $x = e^{-4.34}M/2Ep = 0.00017$ for Z production. The center of the rapidity distribution, $y = 0$, corresponds to $x = 0.013$ for Z production. The accessed x range is essentially covered by the measurements of PDFs from the H1 and ZEUS experiments.

The LO of the double differential Drell-Yan scattering cross section can be written as [23]

$$\frac{d^2\sigma}{dMdy} = \frac{4\pi\alpha^2(M)}{9} 2MP(M)\Phi(x_1, x_2, M^2). \tag{2.8}$$

Here $P(M)$ and Φ are a propagator term and the parton distribution term, respectively. The cross section implicitly depends on the x values of the incoming quark q and the anti-quark $\bar{q}$.

The cross section is a sum of the contributions from photon and Z exchange as well as an interference of them. In case of photon exchange, the propagator and the parton distribution term are given by

$$P_\gamma(M) = \frac{1}{M^4},\ \Phi_\gamma = \sum_q e_q^2 F_{q\bar{q}}, \tag{2.9}$$

$$F_{q\bar{q}} = x_1 x_2 (q(x_1, M^2)\bar{q}(x_2, M^2) + q(x_2, M^2)\bar{q}(x_1, M^2)), \tag{2.10}$$

where e_q is the electric charge of quarks. This contribution is suppressed for large M by the $\frac{1}{M^4}$ term.

The cross-section formula for the γZ interference term can be written as

$$P_{\gamma Z}(M) = \frac{k_Z v_e (M^2 - M_Z^2)}{M^2((M^2 - M_Z^2)^2 + (\Gamma_Z M_Z)^2)},\ \Phi_{\gamma Z} = \sum_q 2e_q v_q F_{q\bar{q}}, \tag{2.11}$$

$$v_f = I_3^f - 2e_f \sin^2\theta,\ a_f = I_3^f\ [f = e, q],$$

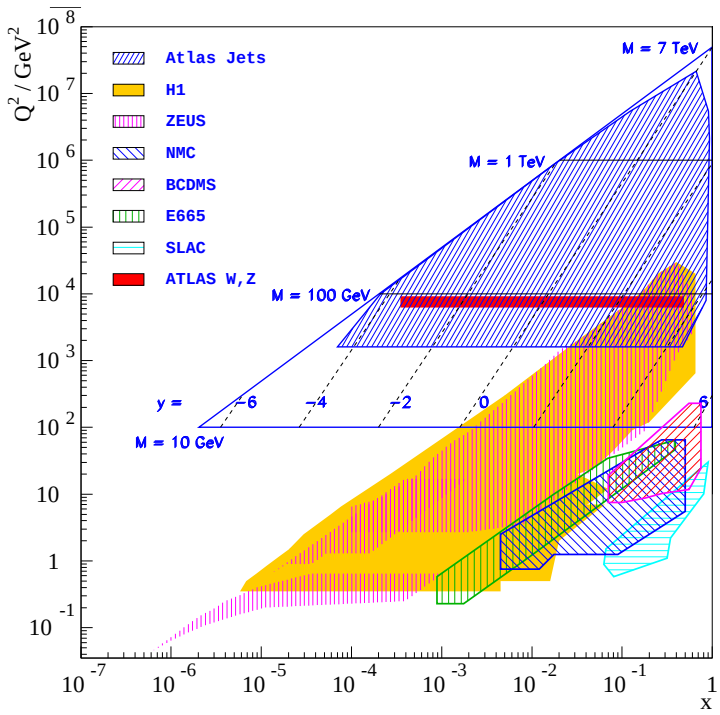

Figure 2.5: The kinematic plane of DIS in Q^2, x bins for HERA and for fixed target experiment and their equivalent in Drell-Yan scattering in M^2, y at the Tevatron and the LHC (for 7 TeV)

$$k_Z = \frac{1}{4\sin^2\theta\cos^2\theta},\ \cos\theta = \frac{M_W}{M_Z}. \tag{2.12}$$

The interference contribution is proportional to the vector coupling of the electron v_e. Since $I_3^e = -1/2$ and $\sin^2\theta$ is close to $1/4$, v_e is small. Therefore, for cross section integrated in the lepton decay angle the γZ contribution is also small. One also sees in Eq. 2.11 that the interference cross-section contribution changes sign from positive to negative if the mass increases and passes M_Z.

A cross-section formula for the pure Z exchange part, in which the vector and axial-vector couplings enter as sums $v^2 + a^2$ can be written as:

$$P_Z(M) = \frac{k_Z^2(v_e^2 + a_e^2)}{(M^2 - M_Z^2)^2 + (\Gamma_Z M_Z)^2},\ \Phi_Z = \sum_q (v_q^2 + a_q^2) F_{q\bar{q}} \tag{2.13}$$

The cross section as a function of the invariant mass integrated over y and lepton decay angle is illustrated in Fig. 2.6, which is dominated by the Z resonance. The calculation was done using the vector and axial-vector constants from Tab. 2.2 and the MRST2004nlo PDFs. At about $M = 70$ GeV the photon and the Z exchange parts are equal. At high masses, beyond 200 GeV, the photon exchange part becomes again larger than the Z exchange part.

The PDF decomposition corresponding to photon and Z exchange is shown in Fig. 2.7. The main contribution comes from the u and d quarks. For the Z exchange the d-quark distribution is higher than u for the central rapidity region and lower for the forward. It can be explained

Particle	vector	axial
u	0.192	0.5
d	-0.346	-0.5
c	0.192	0.5
s	-0.346	-0.5
t	0.192	0.5
b	-0.346	-0.5
e	-0.038	-0.5
μ	-0.038	-0.5
τ	-0.038	-0.5
ν_e	0.5	0.5
ν_μ	0.5	0.5
ν_τ	0.5	0.5

Table 2.2: The list of vector and axial coupling constants for fermions were calculated using Eq. 2.12. $\sin^2\ \theta$ was assumed to be equal to 0.231.

by the contribution of valence quarks, which dominates the "sea" quarks for the low x (forward rapidity).

Therefore the differential cross-section measurement in boson rapidity bins under the mass peak provides a test of the PDFs for u and d quarks. The measurement in the forward rapidity region is more sensitive to u quark distribution. A contribution of s quarks to the Z cross section for the central rapidity is also not negligible, and therefore also the corresponding PDFs could be tested in this measurement.

The discussed scheme can provide only a simplified picture of Z boson production and does not fully describe the kinematic of the bosons, which can be found in an experiment, where Z boson, produced in proton-proton collision have both transverse and longitudinal momentum relative to the beam direction.

The transverse momentum can be explained by initial parton transverse momenta and the production of gluons and quarks along with the gauge boson. The longitudinal momentum of the Z is mostly arise from the initial momentum imbalance of the partons involved in the hard interaction. One of the approaches, which can provides a simplified description of the Z boson kinematics is higher-order corrections to the lowest-order Drell-Yan cross section.

First of this correction is the fact that PDFs depend on Q^2, and should be noted as $q_F(x, Q^2)$. Secondly, there are virtual gluon corrections, namely the radiative corrections to the $f\bar{f}\gamma$ vertex. Their interference with the tree level diagram (see Fig. 2.8 (a,d)), gives corrections in the order of $\alpha_s(Q^2)$.

Also there is a possibility that in $q\bar{q}$ scattering an extra gluon is radiated:

$$q\bar{q} \to l^+l^- + g. \tag{2.14}$$

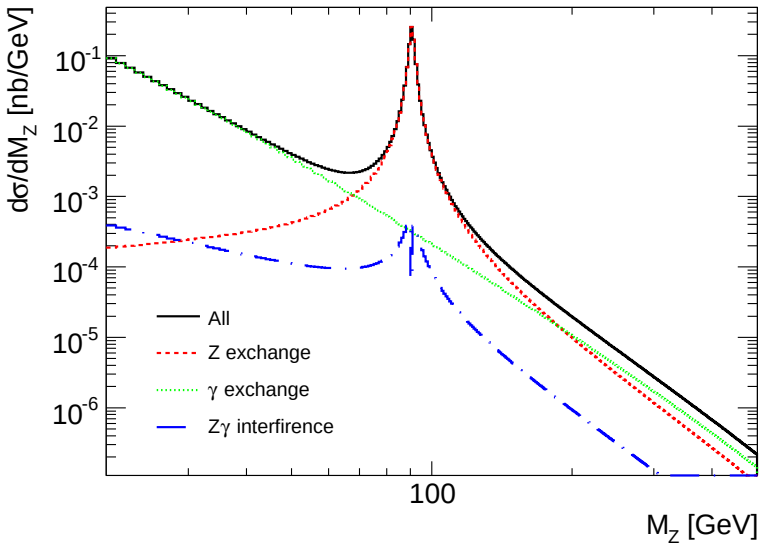

Figure 2.6: $Z \to e^+e^-$ cross section as a function of the invariant mass integrated over the boson rapidity y_Z. At small M the cross section is dominated by the pure photon contribution (green curve). In the resonance region the Z part (red curve) determines the cross section. At large M, the γ and Z contribute similarly to the cross section. The γZ interference contribution (blue curve) is shown in absolute, which is small due to the small vector coupling of the electron ν_e.

This process can be presented in Fig. 2.8 (b,e). Since the initial hadrons contain gluons, in addition to quarks and anti-quarks, gluon initiated processes

$$\begin{aligned} g + \bar{q} &= l^+l^- + \bar{q}, \\ g + q &= l^+l^- + q \end{aligned} \tag{2.15}$$

also contribute to the cross section (see Fig. 2.8 (c,f)).

2.3.1 Z boson decay

The Z boson has a very short lifetime (less than 10^{-24} sec, calculated from its width) and decays into quark or lepton pairs. About 70% of all Z bosons decay into a quark and an anti-quark. Although this channel has the largest branching fraction, it is impossible to select a clean sample of Z events since the background from other QCD process overwhelms the signal. The Z boson can also decay into a lepton and an anti-lepton; the branching fraction into each charged lepton pair is about 10% and into neutrino pair is about 20% [24]. Since coupling of the leptons to gauge bosons are flavour-independent [1], Z boson has the same branching fraction for each charged lepton. The charged lepton channels can be easily used to select a clean sample of Z events.

[1] This property is called lepton universality and has been tested in many experiments [25].

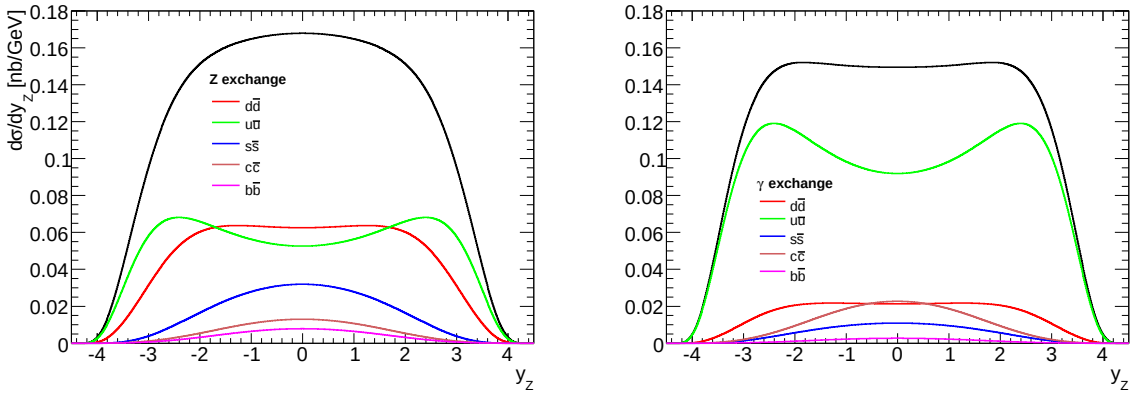

Figure 2.7: The PDF structure of the cross section at $\sqrt{s} = 7$ TeV for Z (left) and γ (right) exchange. The u and d quarks provide the main contribution to the cross section.

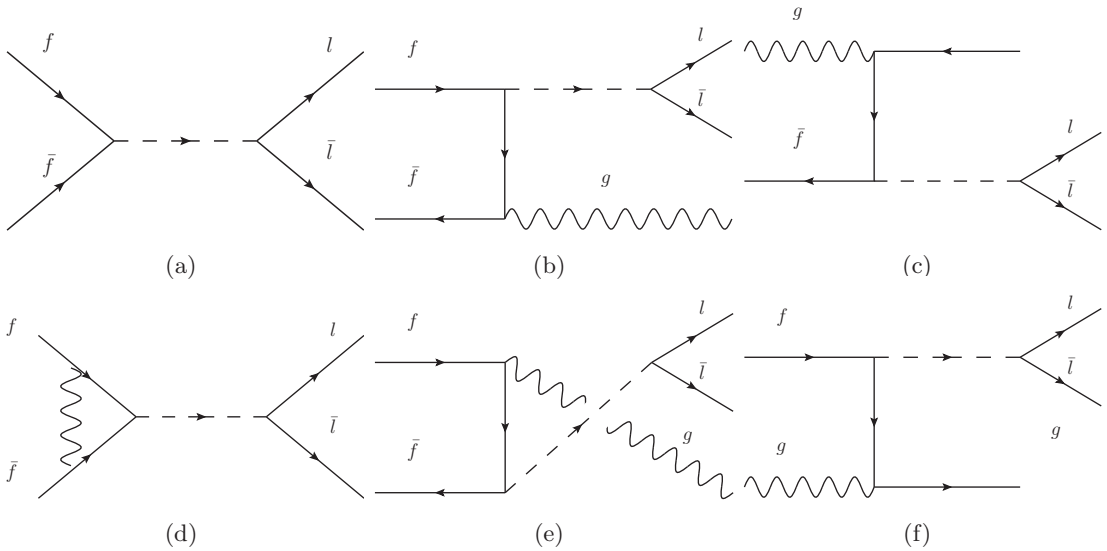

Figure 2.8: LO and NLO Feynman diagrams for the Z boson production. Interference between the tree level Drell-Yan process (a) and the one including the one loop radiative correction to the $\gamma q\bar{q}$ vertex (d). (b,e): $q\bar{q} \to l^+l^- + g$. (c,f): Gluon and $f, \bar{f}$ initiated Drell-Yan scattering.

CHAPTER 3

The LHC (Large Hadron Collider)

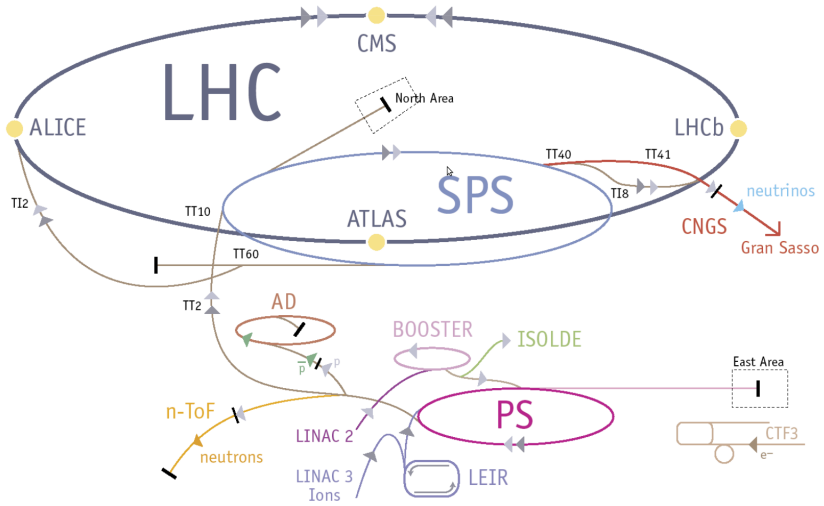

Figure 3.1: The CERN accelerator complex, within the LHC machine at the end of accelerating chain. Each of the LHC's injectors has its own experimental hall, where the beams are used for experiments at the lower energy. The full chain of the proton acceleration includes Linac2 (up to 50 MeV), Booster (up to 1.4 GeV), Proton Synchrotron (PS, up to 25 GeV), Super Proton Synchrotron (SPS, up to 450 GeV) and large ring of the LHC (up to 3.5 TeV on 2010-2011 year.)

The process of the protons acceleration at the CERN accelerator complex (see Fig. 3.1) is shortly described below. The protons, obtained from the hydrogen atoms by stripping orbiting electrons, and pre-accelerated by Linac2 are injected into the PS Booster (PSB) at the energy of 50 MeV. The booster accelerate them to 1.4 GeV. Then beam follows to the Proton Synchrotron (PS) where it is accelerated to 25 GeV. The protons are then sent to the Super Proton Synchrotron (SPS) where they are accelerated to 450 GeV. They are finally transferred to the LHC (in both directions), where they are accelerated for 20 minutes to their nominal energy of 3.5 TeV[1]. Then after a preparation (e.g. squeezing of the beam, aimed to maximize instantaneous luminosity) the collisions start. Colliding beams are delivered to experiments for a couple of hours (up to 20 hours). [26].

[1]The designed beam energy 7 TeV is not reached yet

The proton beams in the LHC are organized in bunches. Under the nominal operation condition, each proton beam has 2808 bunches, with 10^{11} protons per bunch. The bunch spacing of 25 ns corresponds to a frequency of 40 MHz [27]. Large density of bunches in a beam and particles in a single bunch provide a large luminosity, but also produce a so-called pileup effect, when several proton-proton collisions occur in one event. This effect will be discussed further (see Sec. 6.4).

There are 6 experiments installed at the LHC: A Large Ion Collider Experiment (ALICE), A Toroidal LHC ApparatuS (ATLAS), a Compact Muon Solenoid (CMS), a Large Hadron Collider beauty (LHCb), the Large Hadrone Collider forward (LHCf) and the TOTal Electic and Diffractive cross-section Measurement (TOTEM). ALICE, ATLAS, CMS and LHCb are installed around the four interaction points of the LHC accelerator.

ATLAS and CMS are the general purpose experiments, designed to coverer the wide range of high energy physics goals. Despite similarities in the physcics program, they have significantly different experimental design. ALICE is a detector specialized in analysis of heavy-ion collisions. LHCb specialized in a study of the interactions involving b-quarks. LHCf is a small experiment that measures particles, produced close to the beam direction. TOTEM measures the total cross section of the pp interaction.

3.1 Luminosity

The instantaneous luminosity L relates the cross section σ of a given process to the corresponding event rate as $R = L \times \sigma$. Therefore, luminosity is by definition a process-independent quantity which is completely determined by the properties of the colliding beams. An absolute luminosity of the collisions can be expressed in terms of the beam properties as [28]

$$L = \frac{n_b f_r n_1 n_2}{2\pi \Sigma_x \Sigma_y}, \tag{3.1}$$

where n_1 and n_2 are the numbers of particles in the two colliding bunches and Σ_x and Σ_y characterize the widths of the horizontal and vertical beam profiles, n_b is a number of bunches per beam, and f_r is the revolution frequency.

The designed instantaneous luminosity of the LHC is 10^{34} cm^{-2}s^{-1}. After technical problems in November 2008 [29] the LHC did not operate until 2009. The operation in 2010 started very safely at the center-of-mass energy $\sqrt{s} = 7$ TeV and low instantaneous luminosity of 10^{27} cm^{-2}s^{-1} in order to avoid any possible damage. During the data taking the luminosity was increased twice every 2-3 weeks and reach 10^{32} cm^{-2}s^{-1} at the end of the year. This explains, why most part of ATLAS data were collected during the last weeks of the 2010 (see Fig. 3.2).

The luminosity is independently determined by several detectors and multiple algorithms, each having different acceptance, systematic uncertainties and sensitivity to background. The first measurement of the delivered luminosity[1] had 11% systematic uncertainty [31], but later this calculation was improved to the uncertainty of 3.4% [32].

[1] Delivered luminosity is a luminosity which corresponds to the rate of events produced by ATLAS detector.

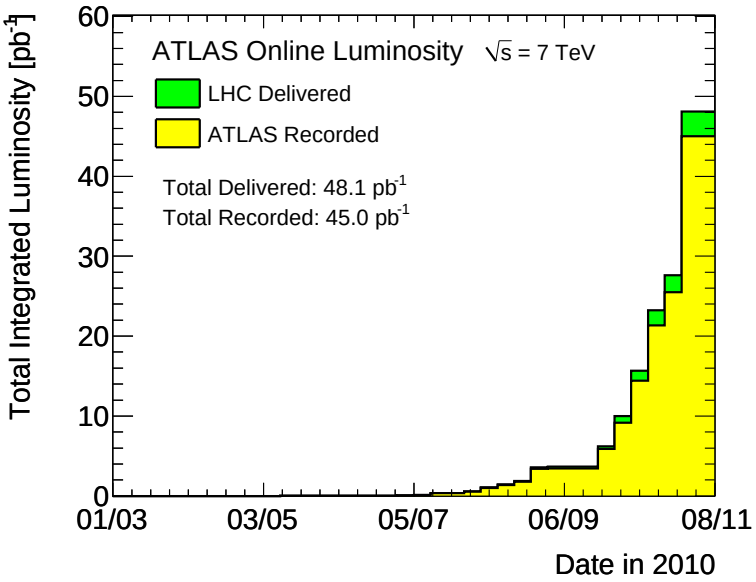

Figure 3.2: The integrated luminosity (in pb^{-1}) which was collected during the 2010 year of the LHC operation [30].

CHAPTER 4

The ATLAS Experiment

ATLAS is a large international collaboration of several thousand physicists from more than thirty nations. The ATLAS experiment was designed to cover the full physics potential of the LHC and it is supposed to be in operation for roughly two decades. The ATLAS collaboration is divided into subgroups, e.g. "e/gamma", "Standard Model", "SUSY", "Higgs", "B-physics" and many others, which perform different physics analyses, e.g. measurement of the Z and W cross sections in electron and muon channels, searching for the Higgs boson and new physics, measurements of quark properties, or studying the detector effects, e.g. energy calibration of the electromagnetic and hadronic calorimeters, measurement of the reconstruction, identification and trigger efficiency for different particles, and detector alignment using tracks.

The ATLAS detector, which is described in the first section of this chapter, provides precise measurements of various physical quantities, e.g. charge, transverse momentum and energy of charged leptons, photons and jets as well as the missing transverse energy. Last two sections describe a computer strategy which allows to store, distribute between the institutes - members of ATLAS and analyze the data.

4.1 Detector description

The ATLAS detector has a cylindrical shape, which is centered around the beam-pipe. Heavy particles are expected to decay into stable particles shortly after their production. Therefore it is not possible to prove the existence or measure the properties of heavy particles directly, but instead to measure their stable [1] decay products. These stable (or long living) decay particles are electrons, photons, muons and hadrons. Since quarks are colored objects, they are hadronizing shortly after their production and appear as concentrated shower of mesons and hadrons in the detector, which are called jets. Neutrinos cannot be detected within the ATLAS detector due to their small interaction cross section with any matter. Their existence in an event can be concluded by a quantity called missing energy, which is the amount of energy needed to balance the energy in one event. Therefore the detector must cover a hermetically

[1] ATLAS defines particles as "stable" if $\tau > 10^{-8}$ sec, they still may decay by GEANT

closed area around the interaction to ensure that no stable particles can escape without being detected.

The shape of the detector already implies a coordinate system. The center of the experiment, i.e. the collision point, is chosen as origin, the beam-direction is defined as the z-axis, the azimuthal angle in the x- and y-plane is labeled as ϕ. The polar angle θ, is defined by $\arctan\frac{r}{\theta}$, where $r = \sqrt{x^2 + y^2}$ is the minimal distance to the z-axis.

Rapidity y can be simplified in the limit of vanishing masses to

$$\eta = -\log(\tan(\frac{\theta}{2})), \tag{4.1}$$

which is called pseudo-rapidity. Transverse momentum p_T is defined as a momentum transverse to the z-axis.

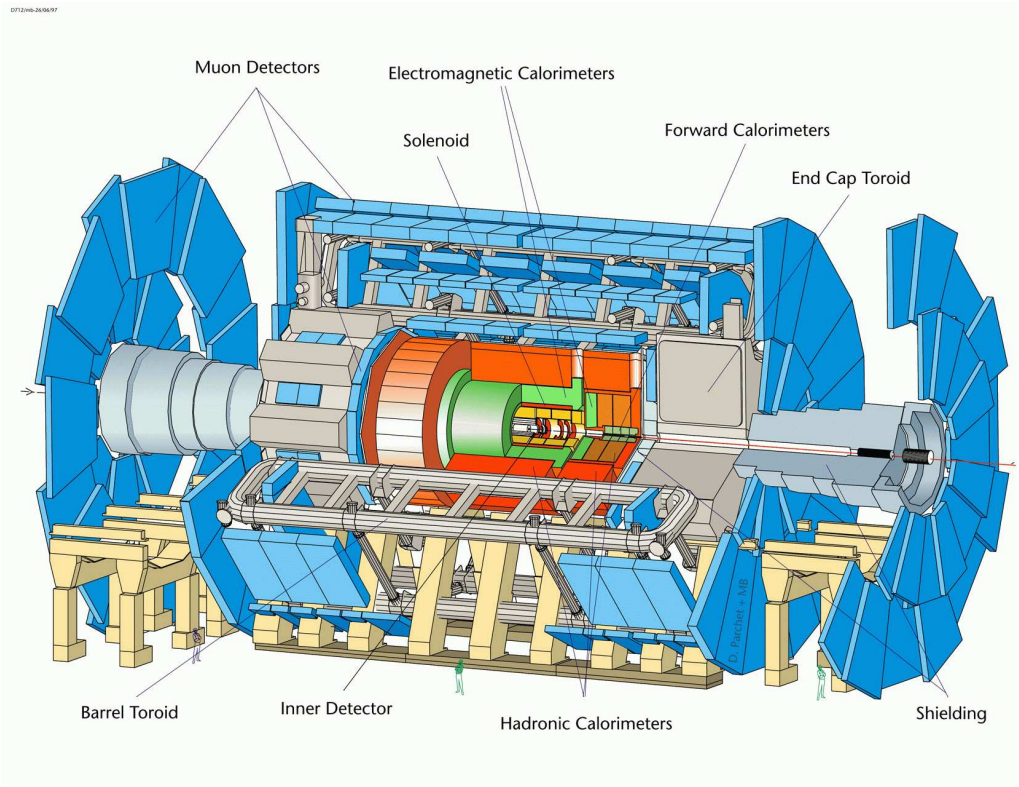

Figure 4.1: A schematic drawing of the ATLAS detector which has three sub-detectors, starting from the inner to the outer: inner detector, calorimetric system, muon spectrometer [33].

A schematic drawing of the ATLAS detector is shown in Fig. 4.1 [34]. ATLAS has three sub-detectors starting from the inner to the outer:

- Inner detector: tracking and measurement of the charge and the transverse momentum of charged particles.
- Calorimetric system: identification of electrons, photons and hadrons and measuring of their energy.

- Muon spectrometer: identification, tracking and the measurement of charge and momentum of muons.

The ATLAS detector is nominally forward-backward symmetric with respect to the interaction point. Each sub-detector can be divided into three parts: the barrel region and two end-cap regions. The barrel region has usually a cylindrical form, while the endcap-region consists of one or more discs which close the barrel region from both ends.

The magnet configuration comprises a thin superconducting solenoid surrounding the inner-detector cavity, and three large superconducting toroids (one barrel and two end-caps) arranged with an eight-fold azimuthal symmetry around the calorimeters.

The inner detector is immersed in a 2 T solenoidal field. Pattern recognition, momentum and vertex measurements, and electron identification are achieved with a combination of discrete, high-resolution semiconductor pixel and strip detectors in the inner part of the tracking volume, and straw-tube tracking detectors with the capability to generate and detect transition radiation in its outer part.

High granularity liquid-argon (LAr) EM sampling calorimeters, with excellent performance in terms of energy and position resolution, cover the pseudo-rapidity range $|\eta| < 3.2$. The hadronic calorimetry in the range $|\eta| < 1.7$ is provided by a scintillator-tile calorimeter, which is separated into a large barrel and two smaller extended barrel cylinders, one on either side of the central barrel. In the end-caps ($|\eta| > 1.5$), LAr technology is also used for the hadronic calorimeters, matching the outer $|\eta|$ limits of end-cap EM calorimeters. The LAr forward calorimeters provide both EM and hadronic energy measurements, and extend the pseudo-rapidity coverage to $|\eta| = 4.9$.

The calorimeter is surrounded by the muon spectrometer. The air-core toroid system, with a long barrel and two inserted end-cap magnets, generates strong bending power in a large volume within a light and open structure. Multiple-scattering effects are thereby minimized, and excellent muon momentum resolution is achieved with three layers of high precision tracking chambers.

4.1.1 Magnet System

Magnetic fields bend the trajectory of charged particles proportional to their field strength [34]. A stronger magnetic field implies a stronger bending of the particle tracks, which enhances the precision of the momentum measurement. The magnet system is separated in two parts: the central solenoid magnet system and the toroid magnet system.

The central solenoid magnet system provides a magnetic field for the Inner Detector. The magnet system is based on superconducting NbTi magnets and cooled down to 4.5 K in a cryostat, which is shared with the calorimeter to minimize the usage of material. The magnet system has a diameter of 2.5 meters and is 5.3 meters long. It is shorter by 80 cm than the Inner Detector, which leads to an non-uniform magnetic field. The field strength is 2 T at the interaction point and 0.5 T at the end of the Inner Detector. A precise knowledge of the field distribution is necessary to provide a precise measurement of the transverse momentum.

The toroid magnet system provides the magnetic field for the Muon Spectrometer. It covers an η -range up to 2.7 and has an average magnetic field strength of 0.5 T. The magnetic field lines are toroidal, which suggests also the name of the magnet system, and are perpendicular to the magnetic field of the solenoid magnet system.

The magnetic field is created by eight superconducting coils in the barrel and by two toroids with eight coils each in the end-cap region. The inner radius in the barrel region is about 5 m, the outer radius is about 10.7 m. These large extensions of the magnetic field allow a track measurement with a long lever arm and hence also improve the precision of the momentum measurement. The magnet coils are not placed in iron, which would increase the magnetic field strength, but are surrounded by air to minimize multiple scattering effects. This is the reason why the toroid magnet system is also labeled as air-core toroid system.

4.1.2 Inner detector

The inner detector is the closest subsystem to the interaction point and therefore has high importance [35, 36]. Its tasks is the precise reconstruction of the trajectories (tracks) of charged particles and both primary and secondary vertex measurements. Knowing the trajectory and the magnetic field in the inner detector, one can calculate the charge, the initial momentum, the direction of flight and the impact parameter of charged particles.

The design of the inner detector must fulfill several requirements to allow an optimal search for rare physics processes. The track reconstruction efficiency of the inner detector should be larger than 90%. The design of the inner detector ensures a coverage in $|\eta|$-direction up to 2.5 and a full ϕ-coverage.

A rather large problem of the inner detector is the high multiplicity of charged particles per collision, which leads to many overlapping tracks and therefore introduces ambiguities in the track reconstruction. The idea to minimize this problem is the combination of a high precision measurement of few points and a nearly continuous low precision measurement of many points along the particle trajectory.

The inner detector consists of three independent sub-detectors (see Fig. 4.2).

- The pixel detector has a very high granularity and allows a high precision measurement of three dimensional interaction points along the particle trajectory.
- The silicon strip detector, or semi conducting tracker (SCT), measures at least four three dimensional space-points along the trajectory also to high precision.
- The straw tracker, or transition radiation tracker (TRT), provides on average 36 measurements in the bending plane of the particle.

4.1.3 Calorimeter

The calorimetric system of the ATLAS measures the energy and position of particles by sampling the energy deposit in the calorimeter. The main goal is the identification of photons, electrons and jets as well as determination of missing transverse energy.

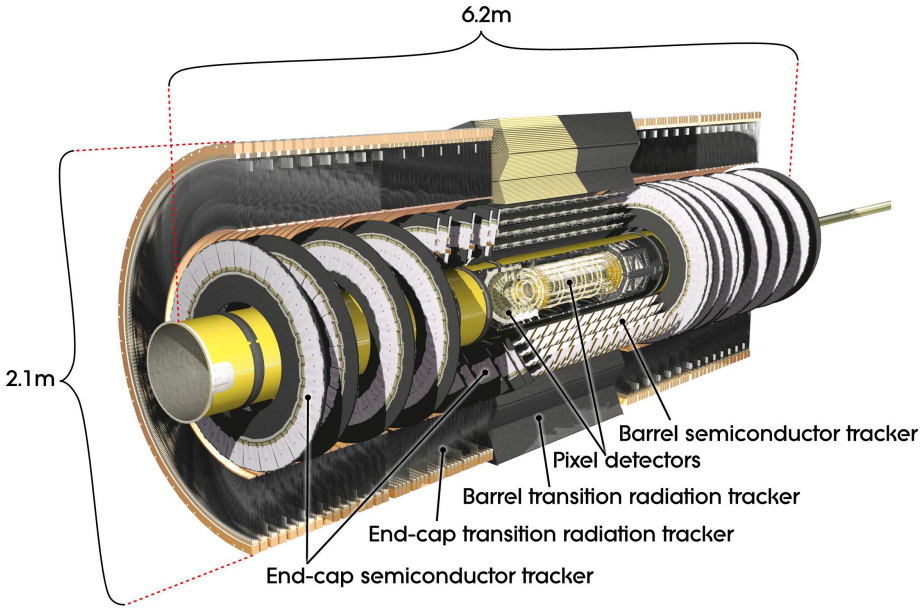

Figure 4.2: The inner detector of the ATLAS. The inner detector provide precision reconstruction of the tracks and both primary and secondary vertex measurements [34].

A view of the sampling calorimeters is presented in Fig. 4.3. The calorimetric system consists of one barrel, two end-cap parts which cover the area up to $|\eta| < 3.2$ and forward calorimeter is placed at $3.1 < |\eta| < 4.9$. Each of these sub detectors is fully ϕ symmetric and coverage all around the beam axis.

The calorimetric system itself has two basic components: The inner component is the EM calorimeter for the measurement of electrons and photons, the outer component is the hadronic calorimeter for the measurement of hadrons.

The particles, which are propagated from the interaction through the tracking system come to the calorimeter. The calorimeter is designed in order to absorb most part of their energy. A propagation particle through the calorimeter have the shower structure. Different particles can be identified due to the shape of their showers. The EM showers are shorter than hadronic showers, therefore the EM calorimeter is closer to beam pipe than hadronic calorimeter.

Each shower consists of hits - a small region of the calorimeter which provides a response from the particle interaction. Each hit normally consists of the several cells of the calorimeter - smallest structure element of the calorimeter, which can provide a signal response.

More part of both hadronic and EM calorimeter is dead material. This material just absorb the energy from the particle and do not produce any signal response. The full energy of the particle can be reconstructed by ratio of the energy which is absorbed in active and dead material and need to be corrected by the calibration.

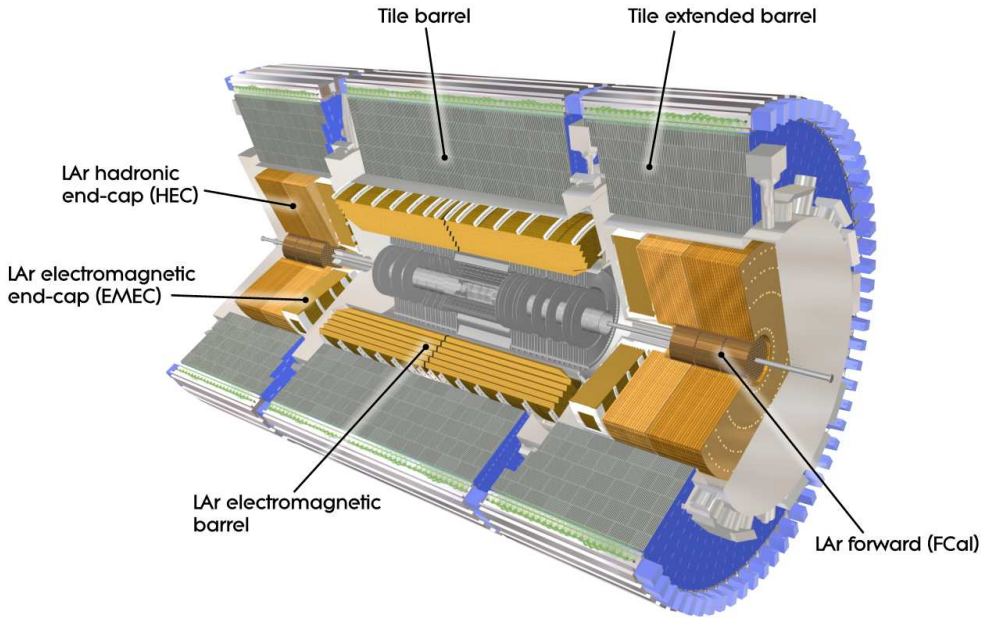

Figure 4.3: The calorimeter system of the ATLAS [34]. The calorimetric system itself has two basic components: The inner component is the EM calorimeter for the measurement of electrons and photons, the outer component is the hadronic calorimeter for the measurement of hadrons.

4.1.3.1 EM Calorimeter

The EM Calorimeter makes use of the interaction of electrons and photons with matter. The most important effect for electrons at high energies is bremsstrahlung which leads to the production of an additional photon. The probability of the interaction depends on the square of the number of protons of the nucleus Z, i.e.

$$\sigma \; Z^2 E_e, \tag{4.2}$$

where E_e is the energy of the electron. The photons themselves produce electron pairs via pair production, which is the dominant process for high energetic photons. Its cross section depends also on Z^2 , via

$$\sigma \; Z^2 \ln E_\gamma, \tag{4.3}$$

where E_γ is the photon's energy. This leads to a cascade of electrons and photons.

An accordion geometry has been chosen for the absorbers and the electrodes of the barrel (EM barrel = EMB) and end-cap EM (EM end-cap = EMEC) calorimeters (see Fig. 4.4). This geometry provides naturally a full coverage in ϕ without any cracks, and a fast extraction of the signal at the rear or at the front of the electrodes. This design ensures that approximately all tracks transverse the same amount of material. The first layer is finely segmented along η, however the coarser granularity of the first layer in the edge zones of the EMB and EMEC. The second layer collects the largest fraction of the energy of the EM shower, and the third layer collects only the tail of the EM shower and is therefore less segmented in η [37].

The active material of the EM calorimeter is liquid argon, which fills the gap between lead absorber plates. The accordion structure plates have a constant gap in the EMB and increases with radius in the end-caps. The liquid argon is kept in the same cryostat as the inner detector solenoid to save additional material of the EM calorimeter.

The readout electrodes are located in the gaps between the absorbers and consist of three conductive copper layers separated by insulating polyimide sheets. The two outer layers are at the high-voltage potential and the inner one is used for reading out the signal via capacitive coupling.

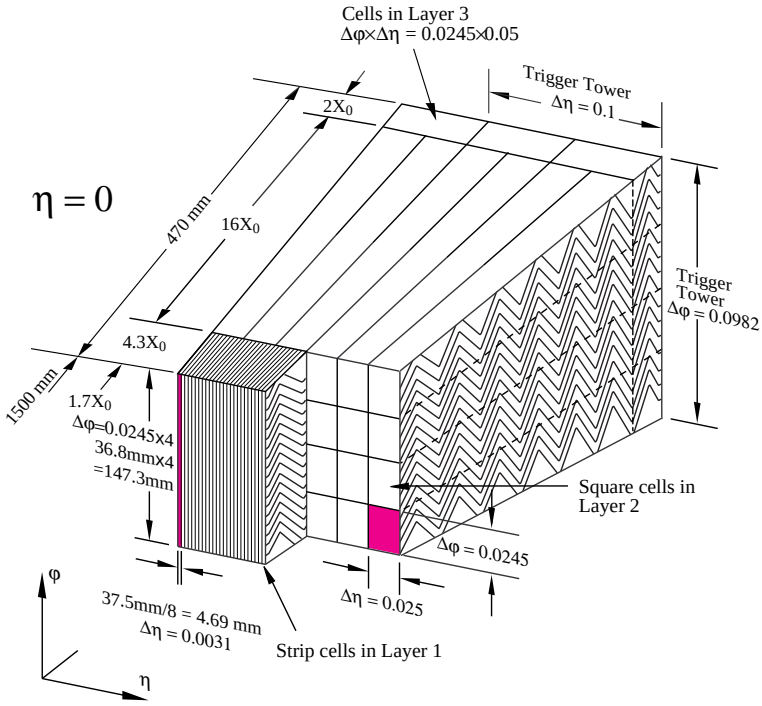

Figure 4.4: The sketch of a EMB module [34]. The accordion structure and their granularity is clearly shown with size of cells.

Details of the calorimeter geometry is important for cross-section calculation and especially for calibration of the EM calorimeter. The EMB is made of two half-barrels, centered around the z-axis. One half-barrel covers the region $0 < \eta < 1.475$ and the other $-1.475 < \eta < 0$. The length of each half-barrel is 3.2 m, their inner and outer diameters are 2.8 m and 4 m respectively. The EMB calorimeter is complemented with a liquid-argon pre-sampler detector, placed in front of its inner surface, over the full η-range.

For ease of construction, each half-barrel has been divided into 16 modules, each covering a $\Delta\phi = 22.5^o$. The total thickness of a module is at least 22 radiation lengths (X_0), increasing from $22X_0$ to $30X_0$ between $|\eta| = 0$ and $|\eta| = 0.8$ and from $24X_0$ to $33X_0$ between $|\eta| = 0.8$ and $|\eta| = 1.3$.

The pre-sampler is a separate thin liquid-argon layer, which provides shower sampling in front of the active EM calorimeter and inside the barrel cryostat. The required segmentation is $\Delta\eta \times \Delta\phi = 0.025 \times 0.1$

The EMEC calorimeters consist of two wheels, one on each side of the EMB, covers the region $1.375 < |\eta| < 3.2$. In the transition region between the EMB and the EMEC calorimeters, the material in front of the calorimeter amounts to several X_0. In order to improve the energy measurement in this region, a liquid-argon pre-sampler is implemented in front of the EMEC, covering the range $1.5 < |\eta| < 1.8$.

Each end-cap calorimeter consists itself of two co-axial wheels: Inner Wheel (IW) and Outer Wheel (OW). The boundary between the inner and the outer wheel, which is 3 mm wide and located at $|\eta| = 2.5$, is mostly filled with low-density material. Each end-cap wheel is further divided into eight wedge-shaped modules without introducing any discontinuity along the azimuthal angle owing to the accordion geometry. The total active thickness of an EMEC is greater than 24 X_0 except for $|\eta| < 1.475$. The thickness increases from 24 to $38X_0$ as $|\eta|$ increases from 1.475 to 2.5 (outer wheel) and from 26 to 36 X_0 as $|\eta|$ increases from 2.5 to 3.2 (inner wheel).

The precision region in the EMEC $1.5 < |\eta| < 2.5$ is divided in depth into three longitudinal layers, with transverse size of the projective cell in the middle layer $\Delta\eta \times \Delta\phi = 0.025 \times 0.025$. Each end-cap pre-sampler, with granularity $\Delta\eta \times \Delta\phi = 0.025 \times 0.1$, consists of 32 identical azimuthal sectors or modules.

The energy of incident electron or photon can be determined in this way, since the number of produced electrons is proportional to the energy of incident electrons or photons. The data are compared to an estimate of the energy resolution in one cell by [38]:

$$\frac{\delta E}{E} = \frac{10.0\%}{\sqrt{E}} \oplus 0.25\% \oplus \frac{0.045 \text{ GeV}}{E}\% \tag{4.4}$$

where the energy is measured in GeV and $\oplus$ indicates addition in quadrature. For the purpose of this comparison, first term is 10%, which is the typical stochastic term for an EM shower, second term is 0.25% for the local constant term, and lest term 45 MeV is the noise measured from a single sample for the considered cell in high gain. The second "constant" term dominates at high energy, so it especially important to minimize.

4.1.3.2 Hadronic calorimeter

The hadronic calorimeter is designed for reconstruction and energy measurement of particle jets, and the measurement of the missing transverse energy in an event. Hadronic jets are longer than EM jets since the interaction length is ten times larger than for EM jets. Due to the larger interaction length of hadrons, more material is needed in the hadronic calorimeter.

The ATLAS hadronic calorimeter contains the tile calorimeter, the liquid-argon Hadronic End-cap Calorimeter (HEC) and the liquid-argon Forward Calorimeter (FCal).

The tile calorimeter is placed directly outside the EM calorimeter envelope. Its barrel covers the region $|\eta| < 1.0$, and its two extended barrels the range $0.8 < |\eta| < 1.7$. It is a sampling calorimeter using steel as the absorber and scintillating tiles as the active material. The read out of the tiles is achieved with optical fibers. Readout cells are formed by a cluster of tiles

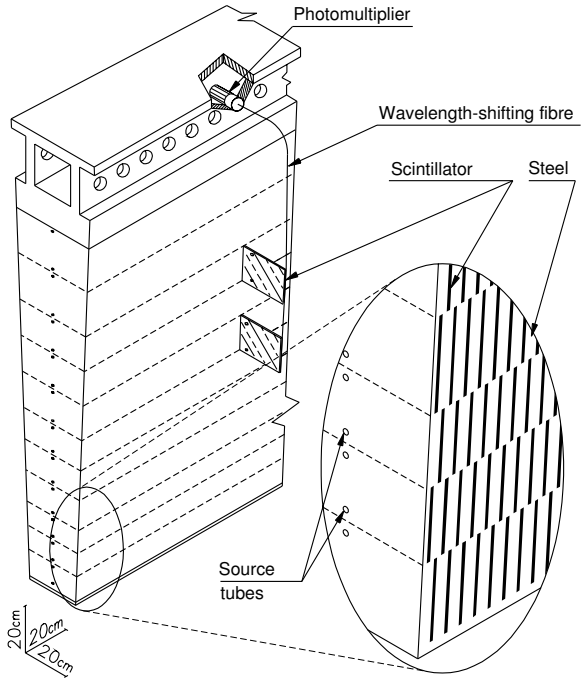

Figure 4.5: The sketch of a tile module of the hadronic calorimeter [34].

and are projective to the interaction point. They provide a granularity of $\Delta\eta \times \Delta\phi = 0.1 \times 0.1$ (see Fig. 4.5).

The HEC consists of two independent wheels per end-cap, located directly behind the end-cap EM calorimeter and sharing the same LAr cryostats. To reduce the drop in material density at the transition between the end-cap and the forward calorimeter (around $|\eta| = 3.1$), the HEC extends out to $|\eta| = 3.2$, thereby overlapping with the forward calorimeter. Similarly, the HEC η range also slightly overlaps that of the tile calorimeter ($|\eta| < 1.7$) by extending to $|\eta| = 1.5$.

The end-cap part of the hadronic calorimeter uses copper plates as absorber material and liquid argon as ionization material. The barrel as well as the end-cap part is segmented into three independent layers.

The FCal are located in the same cryostats as the end-cap calorimeters and provide coverage over $3.1 < |\eta| < 4.9$. As the FCal modules are located at high η, they are exposed to high particle fluxes. This has resulted in a design with very small liquid-argon gaps, which have been obtained by using an electrode structure of small-diameter rods, centred in tubes which are oriented parallel to the beam direction.

Each FCal is split into three 45 cm deep modules: one EM module (FCal1) and two hadronic modules (FCal2 and FCal3) (see Fig. 4.6). To optimise the resolution and the heat removal, copper was chosen as the absorber for FCal1, while mainly tungsten was used in FCal2 and FCal3, to provide containment and minimise the lateral spread of hadronic showers.

The FCal1 layer is made of copper plates stacked one behind the other. An electrode consists of a co-axial copper rod and copper tube separated by a precision, radiation-hard plastic fiber wound around the rod.

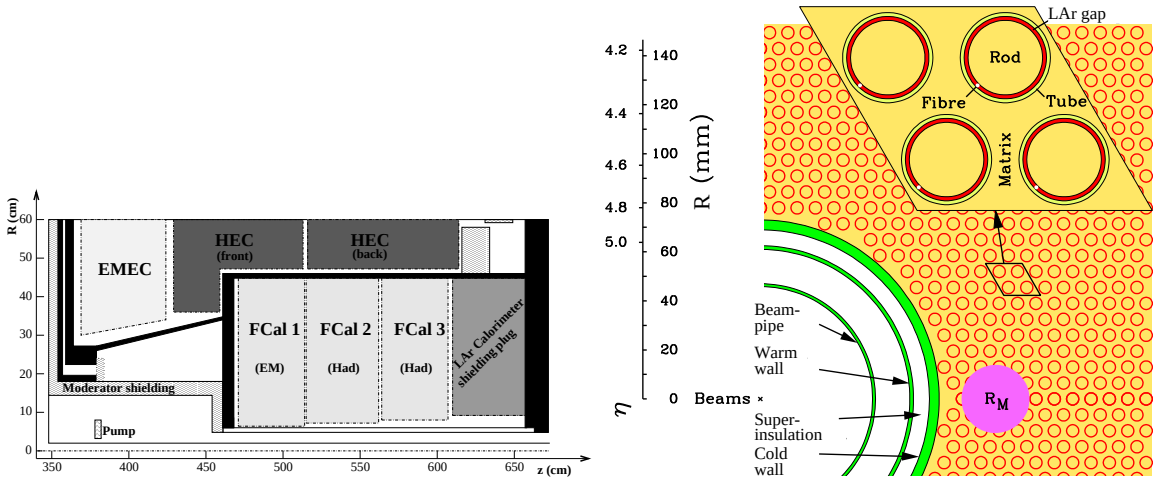

Figure 4.6: Three FCal modules located in the end-cap cryostat (left) and the matrix of copper plates and tubes with rods of the FCal1 (right) [34].

The hadronic modules FCal2 and FCal3 are optimised for a high absorption length. This is achieved by maximising the amount of tungsten in the modules. These modules consist of two copper end-plates, which are spanned by electrode structures, similar to the ones used in FCal1, except for the use of tungsten rods instead of copper rods.

4.1.4 Muon System

The ATLAS muon system (see Fig. 4.7) is focused not only on the identication of muons but primarily a precise stand-alone measurement and triggering of high energetic muons. This independence of the muon spectrometer from the other sub detectors provides good discovery potential at the TeV scale.

The muon system has following structure:

- large barrel toroid: Magnetic field in barrel region,
- smaller end-cap magnets: Magnetic field in end-cap region,
- Monitored Drift Tube (MDT) chambers: Precise muon tracking,
- Cathode Strip Chambers (CSCs): Precise muon tracking in the forward region,
- Resistive Plate Chambers (RPCs): Trigger chamber is the barrel region,
- Thin Gap Chambers (TGCs): Trigger chambers in the end-cap region.

Measurement is based on the magnetic deflection of muon tracks in the large superconducting air-core toroid magnets, instrumented with separate trigger and high-precision tracking chambers. Over the range $|\eta| < 1.4$, magnetic bending is provided by the large barrel toroid. For $1.6 < |\eta| < 2.7$, muon tracks are bent by two smaller end-cap magnets inserted into both

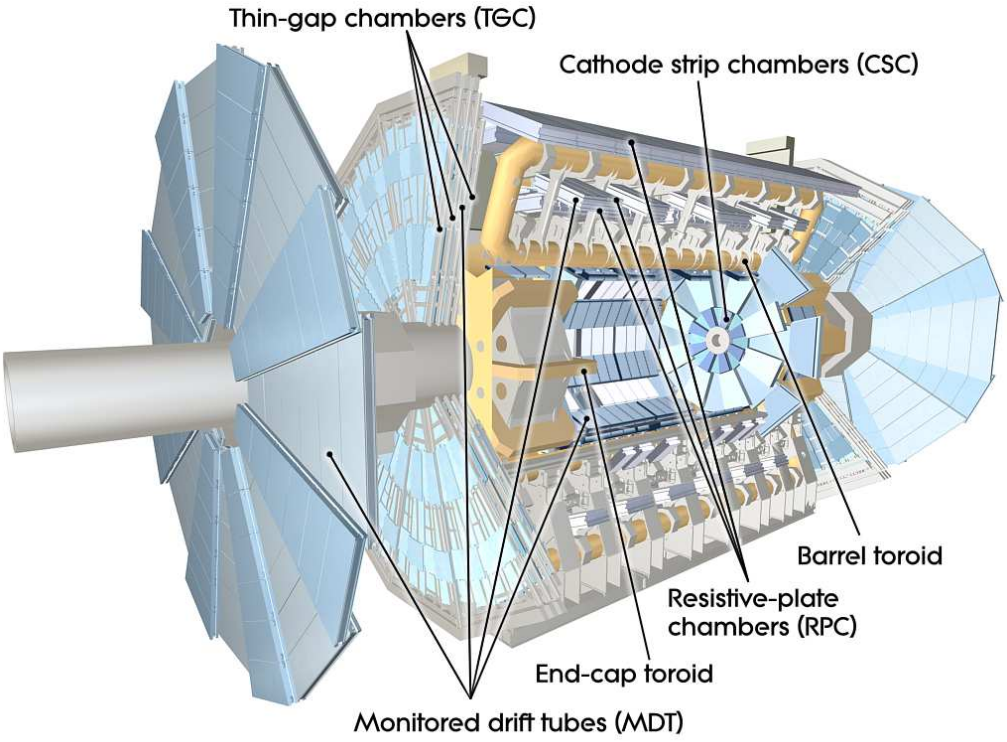

Figure 4.7: The Muon system of the ATLAS detector [34].

ends of the barrel toroid. Over $1.4 < |\eta| < 1.6$, usually referred to as the transition region, magnetic deflection is provided by a combination of barrel and end-cap fields.

The trigger system covers the pseudo-rapidity range $|\eta| < 2.4$. Resistive Plate Chambers (RPC's) are used in the barrel and Thin Gap Chambers (TGC's) in the end-cap regions.

4.1.5 Trigger System

The estimated time between candidate collision at the LHC is up to 25 ns, which provides 40 MHz of the collision rate. The data-size of one recorded collision is in the order of 1 Mb. These regime can give in total 40 Tb/s which is too high for the modern computer technology. The goal of the ATLAS trigger system is to reduce the rate of candidate collisions from 40 MHz to 100 Hz without a loss of interesting physics events, in order to be handled by the ATLAS computer system, which requires 100 Mb/s [39, 40].

The trigger consists of three levels of event selection: Level-1 (L1), Level-2 (L2), and event filter (EF) (see Fig. 4.8). The L2 and event filter together form the High-Level Trigger (HLT). The L1 trigger is implemented as hardware devices in the detector, while the HLT is almost software.

The L1 trigger searches for high transverse-momentum muons, electrons, photons, jets, and τ-leptons decaying into hadrons, as well as large missing and total transverse energy. Its selection is based on information from a different subset of detectors. Using the limited

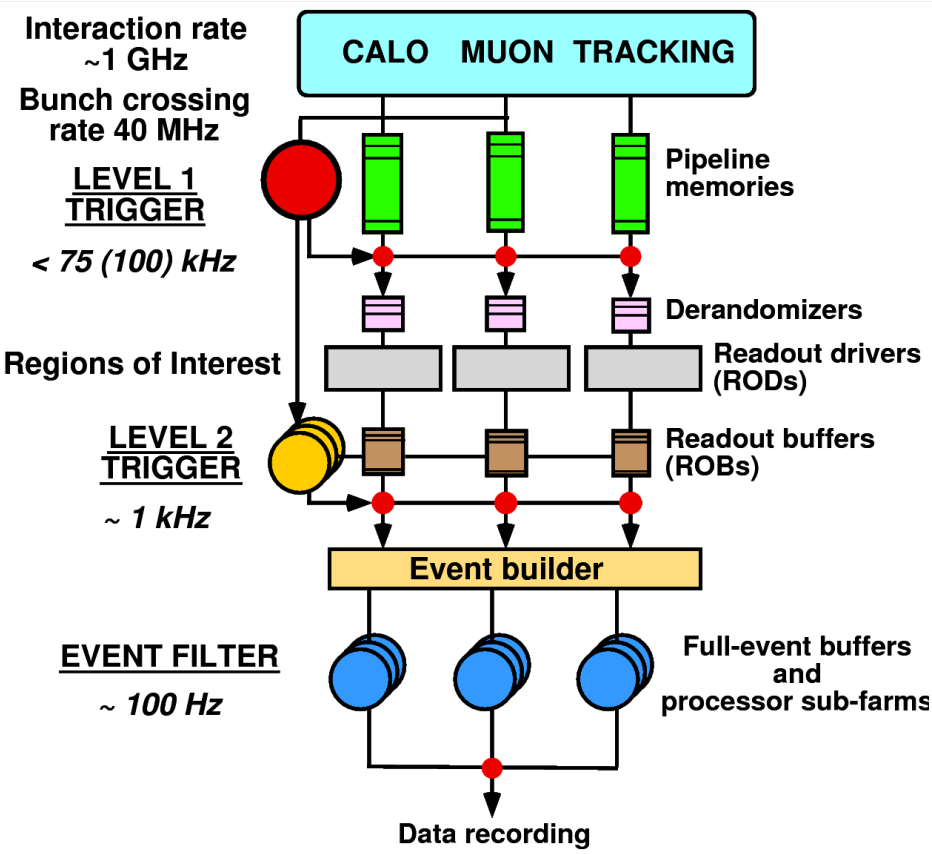

Figure 4.8: The trigger system of the ATLAS, which is consists of three levels of event selection: Level-1, Level-2, and event filter [39].

amount of the detector information it make a decision in less than 2.5 μs reduce the rate to about 75 kHz.

The L1 trigger also defines one or more so-called Regions-of-Interest (RoI's) for each event. The RoI it's a geographical coordinates in η and ϕ, of those regions within the detector where its selection process has identified interesting features. The L1 trigger passes the event information within the RoIs from the read-out buffers (ROBs) to the L2-trigger.

The L2 trigger uses RoI information on coordinates, energy, and type of signatures to limit the amount of data which must be transferred from the detector readout. The L2 trigger reduces the event rate to below 3.5 kHz, with an average event processing time of approximately 40 ms. The principal component of the L2 trigger is the L2 processing farm, where the event selection is executed. The system is designed to provide an event rejection factor of about 30, with an average throughput per farm node of about 200 Hz.

If an event passes the L2 trigger requirements, all information of one event is collected from the ROBs by the so-called Event Builder (EB) and passed to the third trigger level, which is called Event Filter (EF), which reduces the event rate to roughly 200 Hz. Its selections are implemented using off-line analysis procedures within an average event processing time of the order of four seconds.

Unlike the L2 trigger, these tasks are based on standard ATLAS event reconstruction and analysis applications. The steering of the event selection is the same as L2. For those events passing the selection criteria, a subset of the data generated during the event analysis is appended to the event data structure, enabling subsequent off-line analysis to be seeded by the results from the event filter.

At the end of event selection, a tag, which classified physics stream of this event, is added. Events which are accepted by the EF are written to mass-storage devices and available for further off-line-analysis.

ATLAS data acquisition is performed in several streams: muon, "e/gamma", jet, tau, "minimum bias", L1Calo. The streams differ from each other with a different sets of triggers which need to be satisfied. For example, "e/gamma" stream contains all events which were selected by the electron or photon triggers. Different streams are used for different analysis. "E/gamma" stream are used, for example, for electron channels of Z and W analysis; muon stream for muon channel of Z and W analysis and so on.

There are several different electron and photon triggers. Each trigger provides a rate of the event flow. Since the maximum rate, which can be accepted by data acquisition system, is limited, some triggers which have rate higher than this maximum need to be pre-scaled. If a trigger has a pre-scaled factor 5, it means that only one in five events is accepted.

The trigger rate depends on tightness of the selection criteria of this trigger and the instantaneous luminosity of the collision. Tab. 4.1 shows trigger rate dependence on the selection criteria [41].

Trigger	Requirement	Rate at L=10^{30} cm^{-2}s^{-1}
L1 EM2	$E_T > 2$ GeV	1282
L1 EM5	$E_T > 5$ GeV	142
L1 EM10	$E_T > 10$ GeV	21
L1 EM14	$E_T > 14$ GeV	8
EF e15 Medium	$E_T > 15$ GeV, Medium	0.21
EF 2e10 Loose	2 electrons, $E_T > 10$ GeV, Loose	0.013

Table 4.1: The trigger rates for electron triggers, which are normalized to luminosity $L = 10^{30}$ cm^{-2}s^{-1}. The terminology 2e10 Loose, means: 2 electron objects with $E_T > 10$ GeV at EF and "Loose" identification requirements. Triggers with very high rates need to be pre-scaled.

4.2 Computing model

ATLAS works with large amount of data and need a sufficient computer facilities to process this data. For the LHC, storage and processing requirements exceed by far the capacities available at a single site and hence a new approach was chosen, which is commonly known under the LHC Computing Grid (LCG) [42, 43]. This computing grid provides an infrastructure for the storage of data and the necessary computing power for the physics analyses and simulations.

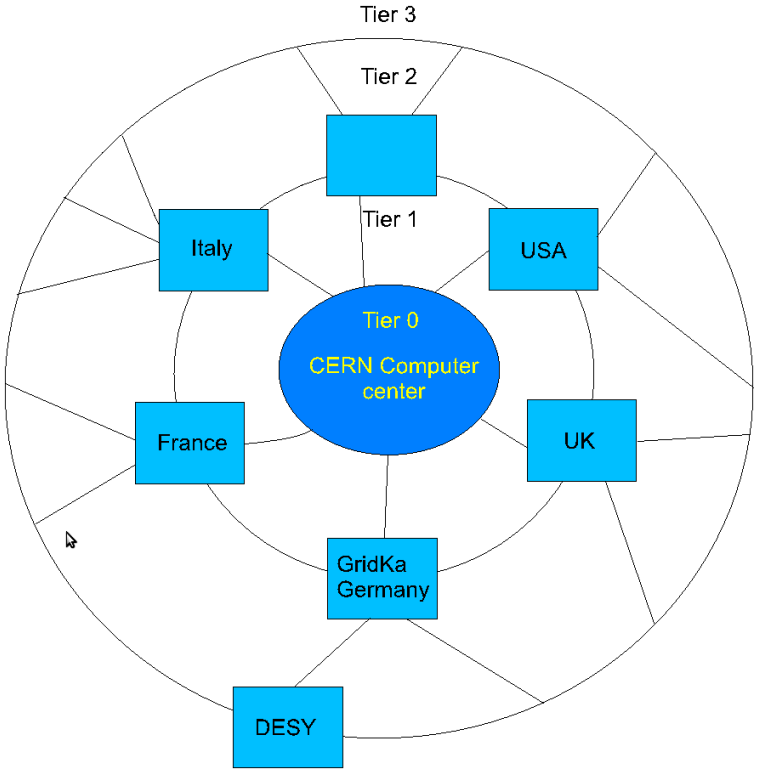

Figure 4.9: The tier structure of the LHC computer grid.

The data distribution follows a so-called tier-structure (see Fig. 4.9). The LHC data is recorded in a first step on tape at so-called tier-0 center at CERN. From there, it is further distributed to worldwide tier-1 centers (e.g. GridKa@FZK), which stores also a large CERN computer center part of data and provides a twenty-four hour support. The tier-2 centers store only a small part of data since they are designated for user specific physics analysis and simulation. The grid is accessed via the lowest hierarchy level (tier-3), which are small computer clusters or individual PCs of physicists.

Tier-structure has several advantages. First several copies of data exists, which ensures safekeeping of data. The single tier centers are independent from each other which minimizes the critical points in the infrastructure. A further advantage is the cost sharing for maintenance and support through the several national computer centers.

4.3 Software framework

The ATLAS software framework for processing the experimental data is called Athena [44]. The architecture underlying Athena is the GAUDI architecture originally developed by the LHCb. This architecture has been extended through collaboration with ATLAS, and an experiment neutral or kernel implementation, also called GAUDI, has been created. Athena is then the sum of this kernel framework, together with ATLAS-specific enhancements. The latter includes the event data model and event generator framework and some other software.

Athena provides an integrated communication between various software applications, called algorithms, within the framework. The principle functionality of an algorithm is to take input data, manipulate it and produce new output data. Each algorithm contains three main parts: initialize, execute and finalize. Initialize and finalize are called once per run. Execute part is called several times ones for each event. Therefore Athena process data event by event. All algorithms have access via the so-called storegate to data of other algorithms, for example the event information or the detector description.

Athena framework contains also so-called services. The services are generally sizeable components that are setup and initialized once at the beginning of the job by the framework and used by many algorithms as often as they are needed. It is not desirable in general to require more than one instance of each service. Services cannot have a state because there are many potential users of them so it would not be possible to guarantee that the state is preserved in between calls.

The message service is an example of additional services that are available to an algorithm. Each service is provided by a component and the uses of these components is via an interface. In general a component implements more than one interface. For example, the event data store service implements another interface called IDataManagerSvc, which is used by the application manager to clear the store before a new event is read in.

The Athena framework allows a dynamic loading of libraries and is organized in form of plug-in modules and allows a flexible configuration of various algorithms which should be executed. The configuration is done via the so-called JobOption file which allows a user specification of the algorithms via python scripting.

For data storage, plotting and processing histograms Athena use Root Framework. Root was developed for particle physics experiment and focused for processing, storage and visualization of large amount of data (up to Tb) [45]. All ATLAS data are stored in one of the Root format, which provide a size compressing and fast access of the data. Root is also used to create figures for presentations, notes and papers in ATLAS collaboration.

Usually so-called TTree format is used to store event information. In TTree information stored event by event in basic Root classes (like Float, Double, Bool, Integer) or in user defined classes. If information is stored in basic classes, it can be easily visualized by any Root tool, like TBrowser (graphic user interface to access information in Root file) or CInt (C++ interpretor). If information stored in user defined class it can be easily restored from Root file as corresponding object in memory.

THist and TGraph Root classes are used to store histograms and graphics. They contain only summary of the events information, like number of entries per bin. These and many other classes are used to to visualize results.

The RooFit [46] is a Root library provides a toolkit for modeling the expected distribution of events in a physics analysis. In presented thesis this library was used to perform fits.

CHAPTER 5

Data sample

The basic time unit for storing luminosity information for later use is the Luminosity Block (LB) [28]. The time length of a luminosity block depends on the machine luminosity, but for $\mathcal{L}_{\text{beam}} \sim 10^{31}$ cm^{-2}s^{-1} it is 60 or 120 seconds. The integrated luminosity can be calculated by following equation:

$$L_{\text{int}} = \sum_i \Delta t_i \cdot \mathcal{L}_i. \tag{5.1}$$

Here i runs over all valid luminosity blocks in which the trigger is configured, Δt_i is the lifetime of the trigger item for luminosity block i, $\mathcal{L}_i$ is the estimated average luminosity over luminosity block i.

During 2010, the ATLAS detector collected about 45 pb^{-1} (1 pb^{-1} = 10^{36} cm^{-2}) of data. The luminosity collection is presented in Fig. 3.2. The 2010 data are split into periods (from A to I) and sub-periods. The periods are shown in Tab. 5.1. Each period differs from the others by the detector condition and the instantaneous luminosity, which increased from 10^{27} cm^{-2}s^{-1} to 10^{32} cm^{-2}s^{-1} (see Sec. 3.1). For the presented analysis, the "e/gamma" stream was used. We did a pre-selection based on the this and that the preselected sample contained 1.3 M events, dominated by QCD background. Due to the increased luminosity from period A to I, the trigger rate changed. In the analysis, an L1 trigger named L1_14 with a nominal threshold $E_T > 14$ GeV and a high-level trigger EF_e15_Medium with a threshold $E_T > 15$ GeV and medium electron identification requirement were used for periods A–E3 and E4–I respectively as lowest not pre-scaled triggers. Both triggers are highly efficient with respect to the off-line selection employed.

During the data taking some parts of the detector could be disabled due to some reason (like parts of the tracker due to problems with the high voltage). The corresponding part of the data should not be used for a physics analysis and are excluded by the so-called Good Run List (GRL), which contains the numbers of good runs and LBs [47]. For this thesis the "WZjets_allchannels" GRL was used. The integrated luminosity, which is calculated with respect to this GRL, is 36.2 ± 1.2 pb^{-1}. The data are taken from the "Autumn Reprocessing", i.e. processed with Athena release 16.

Period	Run Range	Calendar date	Lumi [pb^{-1}]	Max Lumi [$cm^{-2}s^{-1}$]	Trigger
A	152166-153200	30.3–22.4	0.4×10^{-3}	2.5×10^{27}	L1_EM14
B	153565-155160	23.4–17.5	9.0×10^{-3}	6.8×10^{28}	L1_EM14
C	155228-156682	18.5–23.6	9.5×10^{-3}	2.4×10^{29}	L1_EM14
D	158045-159224	24.6–28.7	0.3	1.6×10^{30}	L1_EM14
E	160387-161948	29.7–18.8	1.4	3.9×10^{30}	L1_EM14, EF_e15_Medium
F	162347-162882	19.8–21.9	2.0	1.0×10^{31}	EF_e15_Medium
G	165591-166383	22.9–07.10	9.1	7.1×10^{31}	EF_e15_Medium
H	166466-166964	08.10–23.10	9.3	1.5×10^{32}	EF_e15_Medium
I	167575-167844	24.10–29.10	23	2.1×10^{32}	EF_e15_Medium

Table 5.1: Data periods for 2010 data taking, with their delivered luminosities. Each period differ from others by detector conditions and instantaneous luminosity [30].

CHAPTER 6

Monte Carlo (MC) generators and samples

MC generators are used for obtaining the theoretical predictions for physics processes. These predictions are crucial to understand the measured data and to tune physics analyses. In the early phase of the ATLAS experiment, when no real data were available, MC simulations were used to study the expected sensitivity for various measurements and to tune the present algorithms to achieve an optimal preparation for the analysis of real data.

6.1 MC generators for ATLAS

MC generators for the LHC should describe the structure of hadrons, the parton showers, the actual hard scattering process, and the hadronization. Various MC event generator programs use different approximations during the different steps, and therefore the theoretical prediction relies at least partially on the choice of the event generator. Event generator programs are shortly described below.

Pythia [48]: Pythia is an event generator, which is well tuned to data and therefore commonly used in high energy physics. It can simulate lepton-lepton, lepton-hadron and hadron-hadron interactions with a broad field of theoretical models, including super-symmetric [48] models or models with lepto-quarks. The hard scattering process is calculated in LO approximation. Higher-order corrections are approximated with the parton shower approach.

Herwig [49]: Herwig is a general-purpose MC event generator which includes the simulation of hard lepton-lepton, lepton-hadron and hadron-hadron scattering and soft hadron-hadron collisions in one package. It uses the parton-shower approach for initial- and final-state QCD radiation, including color-coherence effects and azimuthal correlations both within and between jets. In order to generate multiple-parton scattering events in hadron-hadron, photon-photon or photon-hadron events, the Jimmy [50] generator is used. Jimmy is a library of routines which should be linked with the Herwig.

MC@NLO [51]: This MC event generator allows one to incorporate Next-to-Leading Order (NLO) QCD matrix elements consistently into a parton shower. The output of the simulation

is further processed by the HERWIG event generator, which adds higher-order approximations of the parton showers and hadronization.

POWHEG [52, 53]: The POWHEG program is an event generator for heavy quark production in hadronic collisions. It is accurate up to NLO in QCD, and it can be interfaced to shower programs like HERWIG and PYTHIA, in such a way that both the leading logarithmic accuracy of the shower and the NLO accuracy are maintained in the output.

PHOTOS [54]: PHOTOS is a program which is used for generation of QED radiative corrections in decays of any resonances, simulated by a "host" MC generator. These QED corrections are known to affect measurements of the decay properties. PHOTOS is used combined with the other MC programs (PYTHIA, MC@NLO).

6.2 ATLAS chain of MC production

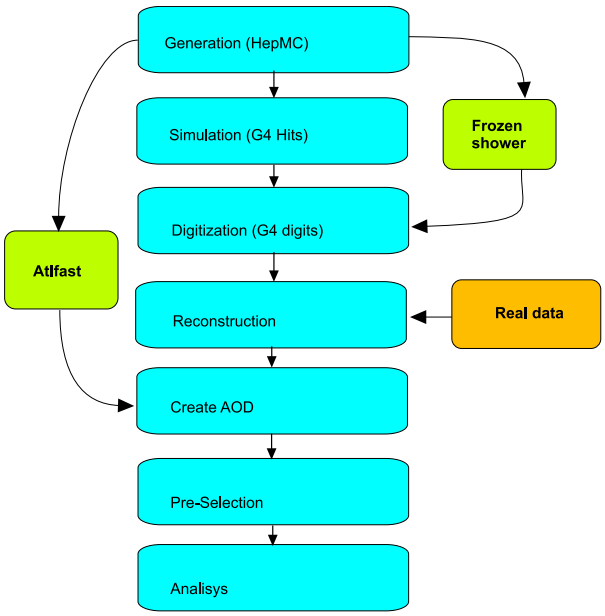

Figure 6.1: The full chain of the MC production in ATLAS. Two possible methods: ATLFast and Frozen-Shower of fast MC production are shown.

The full chain of the ATLAS MC production is shown in Fig. 6.1. This chain includes: generation, simulation, digitization, reconstruction, pre-selection and analysis. The first three steps are necessary only for the production of MC samples, while the others are common for MC and for real data.

The generation step includes the simulation of the proton-proton collision itself, i.e. the calculation of the momentum four-vectors of all particles which are produced in the collision. The generation is based on various MC generator programs. For certain purposes instead of a full MC generation this step can be substituted by the generation of single particles.

The simulation step consist in a propagation of all created particles through the detector material (tracker, calorimeter and muon system) from the place of generation (usually the

interaction point). The simulation is based on the GEANT4 program [55] and uses detailed description of the detector geometry and magnetic fields.

The digitization is a process where the GEANT4 hits from the simulation are subjected to the response of the detector in order to produce digital signals, such as times and voltages. Similar signal are produced in the real detector.

The reconstruction can use both the data from the detector or the output of the digitization step as input information. It includes various algorithms, e.g. for pattern recognition, track fitting or vertex determination. The output of the reconstruction part is so-called Event Summary Data (ESD) and Analysis Object Data (AOD) files. ESD includes a more detailed description of the event than AOD and therefore requires more disc space. In case of MC production, both AOD and ESD files contain generated information.

Each step of this chain could be run separately from others and provide output in ROOT format. Each next step normally uses output of the previous as an input.

The full chain (from generation to AOD creation) requires large CPU time (about 10 min per event). The longest step in this chain is the simulation. Since large statistics of MC samples is required for analysis, fast methods of MC production are useful. There are several approaches of this: ATLFAST, ATLFAST 2 [56, 57] or Frozen Shower (FS) [58].

6.3 Analysis samples

Tab. 6.1 shows the ATLAS MC samples which were used in the presented thesis. The main signal sample was generated with the MC@NLO event generator. The parton showers for all MC@NLO samples are calculated by HERWIG 6.5 with JIMMY 4.1.

Other samples, which are used for cross checks are produced by the POWHEG BOX (v1.0) generator, where events are showered using PYTHIA or HERWIG. The matrix elements for MC@NLO and POWHEG are calculated using the CTEQ 6.6 NLO PDFs [59]. Several background and signal samples are generated with the LO PYTHIA 6.4 and HERWIG 6.5 generators using MRST LO* PDFs [60]. This sample is used for studies of the systematic uncertainties of the electron energy calibration. All samples use the TAUOLA and PHOTOS packages [61, 62] for the simulation of τ decay and QED radiation, respectively. All MC samples are from "MC10 production" and are tuned to ATLAS data [63, 64].

The MC sample with additional passive material in front of the EM calorimeter represents a conservative estimate of the possible increases in the material budget based on various studies [65, 66]. The material budget for this sample is systematically varied adding:

- $0.05X_0$ of material to the inner detector,
- $0.2X_0$ of material in the pixel and SCT services,
- $0.15X_0$ at the end of the SCT/TRT end-caps and at inner detector endplate,
- $0.05X_0$ between the EMB pre-sampler and layer 1 of the LAr calorimeter,

- $0.1X_0$ in front of the LAr EMB calorimeter (in cryostat).

The cross sections given in the table are used to predict the luminosity and to normalize the MC samples. The background EW processes ($Z/\gamma^* \to \tau\tau$, $W \to e\nu$, $W \to \tau\nu$, WW, WZ, ZZ) cross-section values correspond to NNLO calculation are provided by a FEWZ program [67, 68] with a 5% uncertainty for the single boson samples and a 7% uncertainty for the di-boson samples. The $t\bar{t}$ cross section is taken from [69]; it was calculated at $m_t = 172.5$ GeV with a total uncertainty of 6%.

Sample	Data set	Generator	$\sigma * BR * \varepsilon_{\text{filter}}$[nb]	$N_{\text{evt}} \times 10^6$
		Signal		
$Z/\gamma^* \to ee$ ($m_{ee} > 60$ GeV)	106046	Pythia	0.99 ± 0.05	5
$Z/\gamma^* \to ee$ ($m_{ee} > 60$ GeV)	106087	MC@NLO	0.99 ± 0.05	5
$Z/\gamma^* \to ee$ ($m_{ee} > 60$ GeV)	113904	PowHeg Pythia	0.99 ± 0.05	5
$Z/\gamma^* \to ee$ ($m_{ee} > 60$ GeV)	126006	PowHeg Herwig	0.99 ± 0.05	5
$Z/\gamma^* \to ee$ Extra material	106046	Pythia	0.99 ± 0.05	1
		Background		
$Z/\gamma^* \to \tau\tau$ ($m_{ee} > 60$ GeV)	106052	Pythia	0.99 ± 0.05	5
$W \to e\nu$	106043	Pythia	10.46 ± 0.52	7
$W \to \tau\nu$	107054	Pythia	10.46 ± 0.52	2
$t\bar{t}$	105200	MC@NLO	$(0.16 \pm 0.01) \times 0.555$	1
WW	105985	Herwig	$44.9 \times 0.389 \times 10^{-3}$	0.25
WZ	105987	Herwig	$18.5 \times 0.310 \times 10^{-3}$	0.25
ZZ	105986	Herwig	$6.02 \times 0.212 \times 10^{-3}$	0.25

Table 6.1: Data and MC samples used in this thesis. The cross sections quoted are the ones used to normalize the estimation of expected number of events.

6.4 Impact of the pileup effect

A pileup effect is an effect of multiple collisions occurring in one accepted event. There are two types of pileup:

- In-time pileup: multiple collisions in the same bunch crossing. This component can be estimated by measuring multiple interaction points in the same event, e.g. the number of primary vertices,
- Out-of-time pileup: additional collisions in the neighboring bunch crossings.

Since the instantaneous luminosity during the 2010 data taking was much lower than the nominal, the pileup effect was small and can be well measured using the number of reconstructed

primary vertices. In the presented measurement each primary vertex is required to have more than 2 tracks. The primary vertex multiplicity is highly correlated with pileup condition, see for example Fig. 6.2 which shows it for different data taking periods. Increasing instantaneous luminosity from the period A to I caused clear increase of the vertex multiplicity.

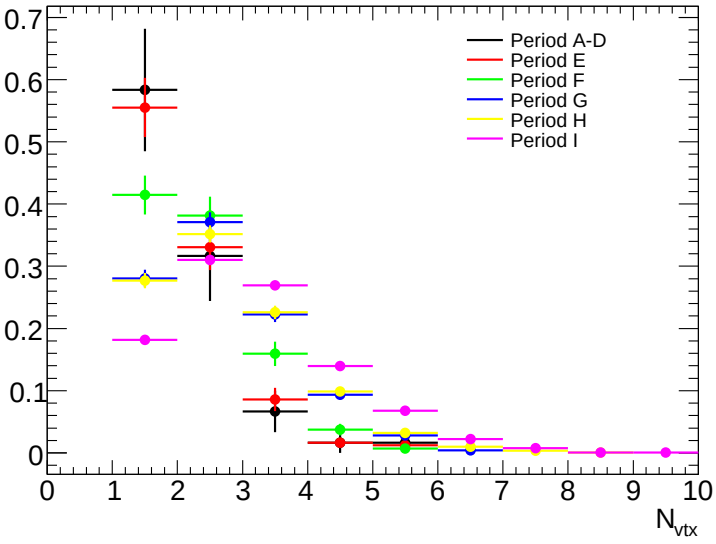

Figure 6.2: Distributions of the number of primary vertices for different periods of the 2010 data. Vertex multiplicity is increased from period A to I due to the increased instantaneous luminosity.

The pileup effects are added to MC by overlaying simulation of the hard interaction with simulation of soft inelastic scatterings. The pileup effects in MC can be corrected to data by reweighting the number of primary vertices. MC events with a vertex multiplicity N_{vtx} are reweighted by the scale factor $SF_{N_{\text{vtx}}}$ calculated as a ratio between the fraction of events with this vertex multiplicity in data and in MC. This reweighting can be done at different stages of the Z selection. The differences between correction factors at various stages can be considered as systematic uncertainties. Tab. 6.2 shows the resulting pileup reweighting factors. The weight for zero vertex event is set to 1.

A comparison of the number of primary vertices for data and MC before and after correction is presented in Fig. 6.3. These differences in the data and MC distributions are used to estimate systematic uncertainty of the cross-section measurement due to pileup effects. The reweighting factors were calculated using event with kinematic selection, while these factors are applied for events with the base $Z \to e^+e^-$ selection (see Sec. 9.2).

6.5 Z boson transverse momentum $p_{T,Z}$ reweighting

Analysis of the boson $p_{T,Z}$ distribution [1, 70] shows a significant discrepancy between data and the MC samples generated with the NLO generators MC@NLO and POWHEG. The description of the data provided by the LO PYTHIA samples is much better since they were

N_{vtx}	Event weight
0	1.000 ± 0.000
1	2.037 ± 0.012
2	1.236 ± 0.005
3	0.839 ± 0.004
4	0.631 ± 0.001
5	0.509 ± 0.002
6	0.431 ± 0.004
7	0.385 ± 0.006
8	0.382 ± 0.012
9	0.339 ± 0.020
10 or more	0.420 ± 0.039

Table 6.2: Pileup reweighting factors with statistical uncertainties. The weight 1 is set for zero-vertex events. The reweighting factors were calculated using events at kinematic selection (see Sec. 9.2).

tuned to Tevatron measurements. Therefore the NLO samples used in this thesis are always reweighted in $p_{T,Z}$. The reweighting is performed at the generator level before any selection and before QED radiation.

Uncertainty is estimated from data to MC $p_{T,Z}$ distribution comparison. For that, the exponential slope in $p_{T,Z}$ is varied within uncertainties allowed by the data. The resulting uncertainty on the cross section is less than 0.1%.

Fig. 6.4 shows a comparison of the $p_{T,Z}$ distributions for MC@NLO and Pythia (left) and their ratio (right). The calculation is performed in bins with logarithmically growing size. This reweighting significantly improves data-MC agreement for the $p_{T,Z}$ distribution. However the effect on the measured cross sections is small, typically less than 0.3%.

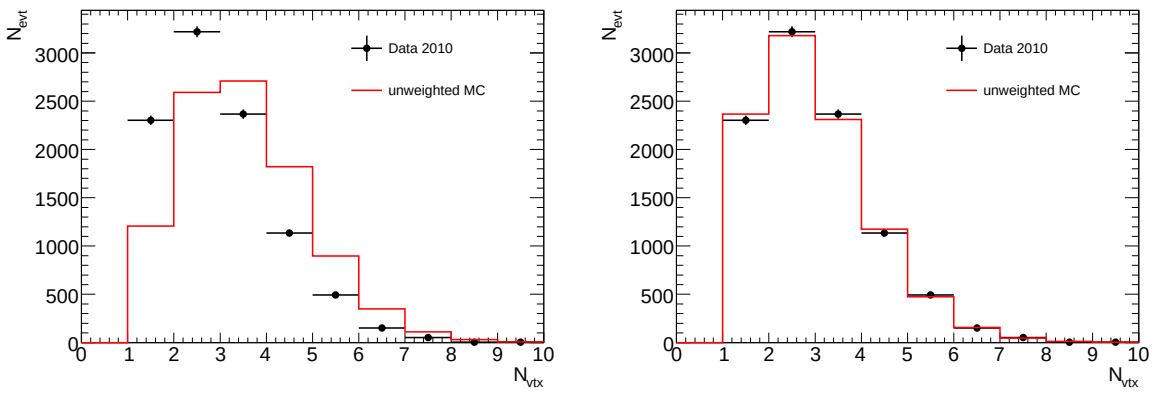

Figure 6.3: A comparison of the primary vertex multiplicity for data and MC before (left) and after (right) the reweighting. Base $Z \to e^+e^-$ selection for the CC analysis was applied (see Sec. 9.2). The MC is normalized to data by the integral under distribution.

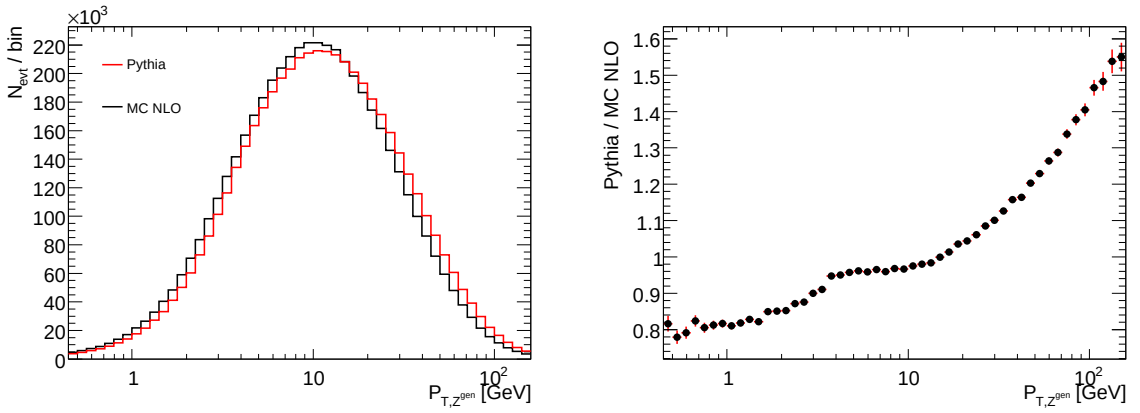

Figure 6.4: A comparison of the Z boson $p_{T,Z}$ distribution for MC@NLO and PYTHIA (left) and their ratio (right). The figures are performed in bins with logarithmically growing size. The ratio is used as reweighting factors. Uncertainties of the pileup reweighting factors are obtained from the finer binning.

CHAPTER 7

Cross-section $\sigma(Z \to e^+e^-)$ measurement

The cross sections are determined using the MC@NLO MC sample for a factorized acceptances (defined below). This acceptance is calculated for each cross-section bin. The method assumes that smearing and resolution effects are correctly described by the MC simulation. Differences in efficiency between data and MC simulation are applied as correction functions, using detector related variables (see Sec. 9.3).

This chapter describes a method for the integrated and single differential cross-section measurement. The binning in y_Z variable is introduced and bin-migration effects are investigated.

7.1 Measurement techniques

The $Z \to e^+e^-$ cross section is calculated using the following equation:

$$\sigma_{\text{total}} = \frac{N - B}{A_Z C_Z L_{\text{int}}}, \tag{7.1}$$

where

- N is the number of $Z \to e^+e^-$ candidates in the selected data sample,
- B is the number of background events in the selected data sample,
- A_Z and C_Z are the factorized acceptances, defined below,
- $L_{\text{int}} = 36.2$ pb^{-1} is the integrated luminosity with respect to the analysis trigger and GRL.

The so-called fiducial cross section is defined as:

$$\sigma_{\text{fidu}} = \frac{N - B}{C_Z L_{\text{int}}}; \tag{7.2}$$

it is measured only in the fiducial region corresponding to the geometrical acceptance of the detector. The fiducial region is defined by the following cuts for the CC analysis (see Sec. 9.2):

$$\begin{gathered}\text{both electrons: } p_{T,e} > 20 \text{ GeV},\\ \text{both electrons: } |\eta_e| < 2.47 \text{ excluding crack: } 1.37 < |\eta_e| < 1.52,\\ 66 < m_{ee} < 116 \text{ GeV}.\end{gathered} \tag{7.3}$$

and for the CF analysis:

$$\begin{gathered}\text{both electrons: } p_{T,e} > 20 \text{ GeV},\\ \text{central electron: } |\eta_e| < 2.47, \text{ excluding crack: } 1.37 < |\eta_e| < 1.52,\\ \text{forward electron: } 2.5 < |\eta_e| < 4.9,\\ 66 < m_{ee} < 116 \text{ GeV}.\end{gathered} \tag{7.4}$$

Here $p_{T,e}$ and η_e are the transverse momentum and pseudo-rapidity of the electron. For the A_Z factor calculations all cuts are applied using generated four-vectors (without smearing) and before FSR QED radiation. In the following, this kinematic reconstruction will be called "generated information" as opposed to "reconstructed information", which is derived from the detector measurements. The values of cut-threshold coincide with the threshold of cuts of the kinematic selection (see Sec. 9.2).

The total value of the selection acceptance was calculated using a signal MC sample and factorized in two terms A_Z and C_Z as follows:

$$A_Z = \frac{N_{\text{gen, fidu cuts}}}{N_{\text{gen, mass cut}}},\ C_Z = \frac{N_{\text{rec, analys. cuts}}}{N_{\text{gen, fidu cut}}}, \tag{7.5}$$

where

- $N_{\text{gen, fidu cuts}}$ — is the sum of event weights taken from generated level for events which have passed the fiducial cuts,
- $N_{\text{gen, mass cuts}}$ — is the sum of event weights of all generated events within the mass window [66-116] GeV
- $N_{\text{rec, anal cuts}}$ — is the sum of event weights after the reconstruction and analysis selection (see Sec. 9.2).

7.1.1 Binning definition

The $Z \to e^+e^-$ differential cross-section measurement was performed in bins of absolute di-electron rapidity $|y_Z|$ (see Tab. 7.1). The same bins were used for both CC and CF analyses.

Eq. 7.1 can be written for the differential (in y_Z bins) fiducial cross section as:

$$\frac{\Delta\sigma^i_{\text{fidu}}}{\Delta y^i_Z} = \frac{1}{\Delta y^i_Z}\frac{N^i - B^i}{C^i_Z L_{\text{int}}}, \tag{7.6}$$

where i is the bin number and Δy^i_Z is the width of bin i. N^i and B^i are the number of $Z \to e^+e^-$ candidates and the number of background events in selected data sample in bin i.

Boundaries	CC analysis	CF analysis
$0.0 < \|y\| < 0.4$	+	–
$0.4 < \|y\| < 0.8$	+	–
$0.8 < \|y\| < 1.2$	+	–
$1.2 < \|y\| < 1.6$	+	+
$1.6 < \|y\| < 2.0$	+	+
$2.0 < \|y\| < 2.4$	+	+
$2.4 < \|y\| < 2.8$	–	+
$2.8 < \|y\| < 3.6$	–	+

Table 7.1: Bins in $|y_Z|$ which are used for the CC and CF $Z \to e^+e^-$ cross-section measurements.

C_Z^i is defined by Eq. 7.1, but calculated in bin i. In this formula the cross section is unfolded by the bin-by-bin method. In this method the bin-migration effect, where the Z boson was generated in one bin but reconstructed in another, is not taken into account.

7.1.2 Studies of the bin-migration effect

The bin-by-bin unfolding method requires good detector resolution. The resolution is determined using MC samples where reconstructed electrons are required to be matched within ΔR_e [1] cone of 0.2 to a generated electron (the so-called truth matching). The resolution σ_{y_Z} can be estimated as a difference between generated and reconstructed Z boson rapidity $y_Z^{\text{gen}} - y_Z^{\text{rec}}$.

Fig. 7.1 shows σ_{y_Z} measured for MC events passing all selection criteria. Values in bins were calculated as the width of a Gaussian fit in each bin.

The resolution is about 40 (16) times smaller than the bin size for CC (CF) selection. This ensures that migration across bin boundaries is small.

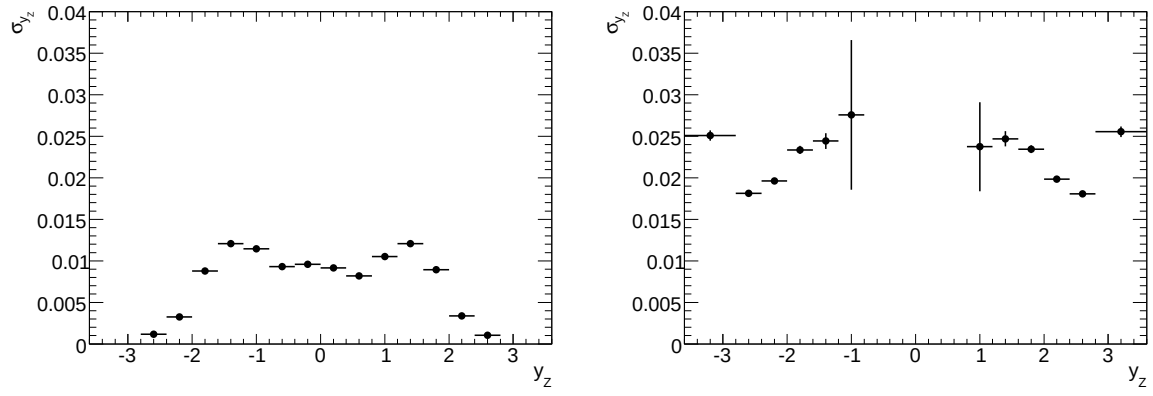

Figure 7.1: Resolution σ_{y_Z} estimated in y_Z bins for the CC (left) and CF (right) selections.

[1] $\Delta R_e = \sqrt{\Delta\eta_e^2 + \Delta\phi_e^2}$, where $\Delta\eta_e$ and $\Delta\phi_e$ are the difference between the generated and reconstructed pseudo-rapidity and ϕ of the electron, respectively.

Other criteria which can be used in order to quantify the bin-migration effect are the purity and stability. They are defined for each bin i as:

$$P^i = \frac{N^i_{\text{rec\&gen, all reco cuts}}}{N^i_{\text{rec, all reco cuts}}},\ S^i = \frac{N^i_{\text{rec\&gen, all reco cuts}}}{N^i_{\text{gen, all reco cuts}}}, \tag{7.7}$$

where

- $N^i_{\text{rec, all reco cuts}}$ — is the sum of event weights reconstructed in bin i,
- $N^i_{\text{gen, all reco cuts}}$ — is the sum of event weights generated in bin i,
- $N^i_{\text{rec\&gen, all reco cuts}}$ — is the sum of event weights which were generated and reconstructed in bin i.

Defined this way, the purity measures migrations into the bin, e.g. which fraction of the events reconstructed in the bin was also generated in the same bin. The stability is used to measure migrations out of the bin, e.g. which fraction of the events generated in the bin is also reconstructed in the same bin.

Studies of the purity and stability are performed for the CC and CF selections and shown in Fig. 7.2. For all bins the values exceed 85% indicating a low level of bin migrations.

7.1.3 Combination volume

Both the CC and CF fiducial differential cross-section measurements are extrapolated to a common combination volume in order to be combined and compared to theory. This extrapolation volume is defined without any η_e selection:

$$\begin{gathered}\text{both electrons: } p_{T,e} > 20 \text{ GeV},\\ 66 < m_{ee} < 116 \text{ GeV}.\end{gathered} \tag{7.8}$$

The cross section in the muon channel is calculated under the same conditions and can be combined with the electron channel as well. The extrapolation factor E which is used to extract the combination from the fiducial cross sections in $|y_Z|$ bins $\sigma^i_{\text{comb}} = \sigma^i_{\text{fidu}}/E^i$ (where i is the bin number) is defined as:

$$\begin{aligned}E^i_{\text{CC}} &= \frac{N^i_{\text{fidu\_CC}}}{N^i_{\text{comb}}},\\ E^i_{\text{CF}} &= \frac{N^i_{\text{fidu\_CF}}}{N^i_{\text{comb}}},\end{aligned} \tag{7.9}$$

where:

- N^i_{comb} — is the sum of event weights generated in bin i for event which have passed combination selection criteria,
- $N^i_{\text{fidu\_CC}}$ and $N^i_{\text{fidu\_CF}}$ — are the sums of event weights generated in bin i for event which have passed the CC and CF selections criteria respectively.

The value $C^i_{\text{comb}} = \frac{C^i_Z}{E^i}$ will be used in a following chapters as well.

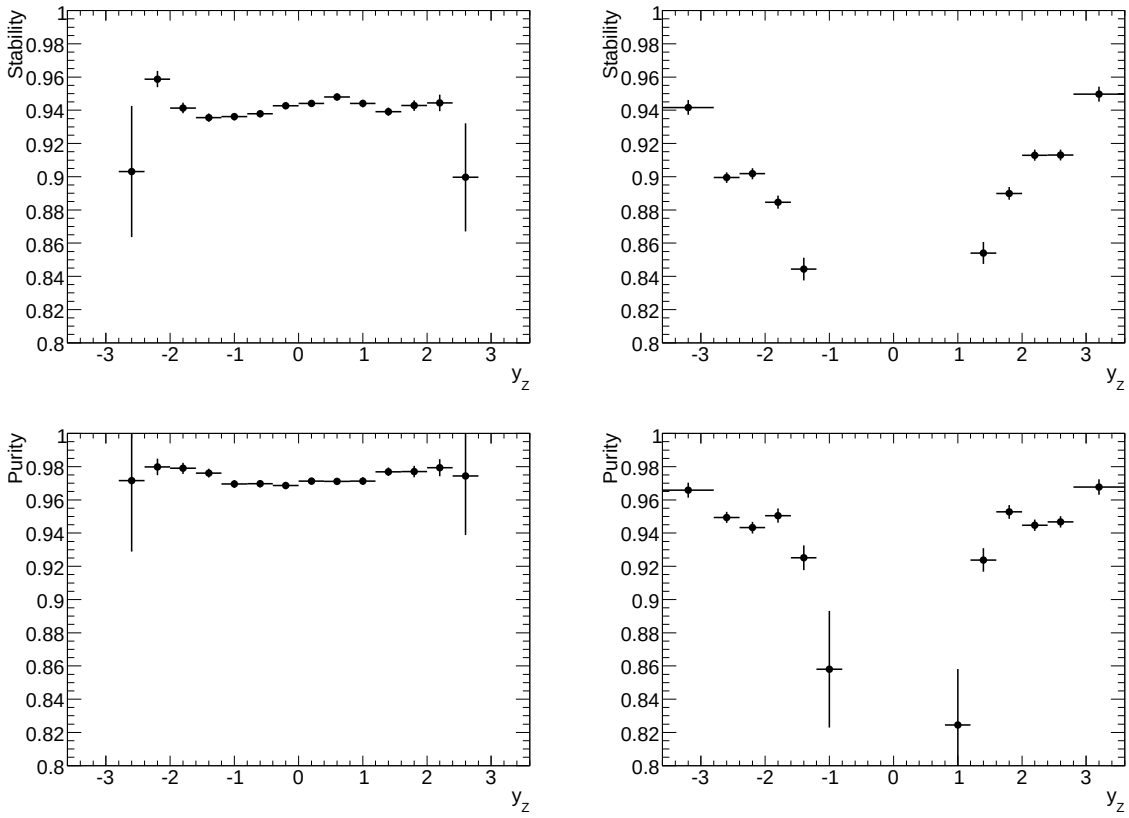

Figure 7.2: Stability (top) and purity (bottom) for the CC (left) and CF (right) selections. Both purity and stability are lower for the CF selection because in this case the resolution is worse.

CHAPTER 8

Event reconstruction

The reconstruction of $Z \to e^+e^-$ events requires two electron candidates to be reconstructed with high efficiency and low background contamination. In the present analysis the reconstruction of the electron candidates consists of the following steps: on-line selection (trigger), electron track and cluster reconstruction, electron identification and electron isolation requirement. This chapter contains a brief description of these steps.

The ATLAS group responsible for reconstructing and identifying electrons and photons is called "e/gamma" group. The same name was given to the ATHENA package used for EM objects performance measurements [2, 71–73].

8.1 Trigger (TG) performance

The trigger system in ATLAS consists of level 1 (L1), level 2 (L2) and event filters (EF) (see Sec. 4.1.5). The triggering of an EM object starts from the L1 trigger: it selects the EM object, that has transverse energy E_T above threshold deposited in the EM calorimeter in two adjacent towers of size $\Delta\eta \times \Delta\phi = 0.1 \times 0.1$ size. The algorithm of the L2 trigger includes a fast track reconstruction and a fast calorimeter reconstruction, which is similar to the off-line procedure. The EF uses the reconstruction and identification algorithms described below.

8.2 Electron reconstruction

ATLAS mainly uses two sub-detectors to reconstruct the electrons: the inner detector which is used for track reconstruction, and the LAr EM calorimeter which measures the energy in three longitudinal layers, with a pre-sampler layer in front.

Three different algorithms are used for electron reconstruction depending on the context [2, 72]. For each object the information about the algorithm used to reconstruct this object is stored in the "author" variable.

- **author=1**: Cluster-based algorithm with track-match. This algorithm is dedicated mostly to high $p_{T,e}$ isolated electrons. It is seeded by a reconstructed cluster with transverse energy above ~ 3 GeV from the EM calorimeter, and a matching track is searched

for among all reconstructed tracks which do not belong to a photon-conversion pair reconstructed in the inner detector.

- **author=2**: Track-based algorithm is dedicated to low $p_{T,e}$ electrons and electrons in jets. It is seeded by a track in the inner detector.

- **author=8**: Cluster-based forward algorithm without track match is used for electron reconstruction in forward region, where the track information is absent and therefore track matching could not be performed (inner detector provides track only for $|\eta_e| < 2.5$).

An electron candidate may be found with the standard (cluster based) and soft-electron (track based) algorithm at the same time. This overlap is approximately resolved when the AODs are constructed: if the track is common to a candidate soft-electron and a standard "e/gamma", then the objects are considered to be the same. These objects will have author=3.

The central electron reconstruction uses clusters reconstructed using fixed window algorithm. The first layer is made of strips and has the finest segmentation in η to separate photons from π^0 decays. The second layer has a coarser segmentation and contains most of the shower energy. The third layer ensures the measurement of the shower tail.

The cell with the maximum energy is searched within a small η and ϕ window around the extrapolation point: $\Delta\eta \times \Delta\phi = 3 \times 3$ in the pre-sampler, 3×1 in the strip compartment; 3×3 in the middle sampling; 3×1 in the back sampling. The EM shower shape variables are calculated with respect to these hot cells.

All tracks that pass the good quality cuts are extrapolated to the second sampling of the EM calorimeter. Around the extrapolated track a $\Delta\eta \times \Delta\phi = 3 \times 7$ cluster is created in the EMB and 5×5 in the EMEC.

The cluster energy is corrected for simulation of the calorimeter response in η and ϕ and for leakage outside the cluster in a given window. In the region between the EMB and EMEC calorimeters, the cluster energy is in addition corrected for energy losses using the energy deposit in the crack scintillators.

The forward electron reconstruction is based on a similar algorithm, but uses only the information from the calorimeters, as the tracking system is limited to $|\eta_e| < 2.5$. An electron candidate in the forward calorimeters is reconstructed if there is a cluster with $E_T > 5$ GeV.

8.3 Electron identification (ID)

The standard ID of high-$p_{T,e}$ electrons is based on many cuts which can all be applied independently [2, 72]. These cuts have been optimized in several η_e and $p_{T,e}$ bins. The cut decisions for each individual cut in this list are written in the so-called "IsEM" bit mask which can provide "loose", "medium" and "tight" level of electron ID, providing flexibility in the analysis. The "IsEM" bit mask is available for each reconstructed electron.

- **ID "Loose"** performs a simple electron ID based only on limited information from the calorimeters. Cuts are applied on the hadronic leakage and to the shower shape

variables, derived from only the middle layer of the EM calorimeter. This set of cuts provides excellent ID efficiency, but low background rejection.

- **ID "Medium"** improves the quality by adding cuts on the strips in the first layer of the EM calorimeter and on the tracking variables. These cuts are effective in rejecting $\pi \to \gamma\gamma$ background. The tracking variables include the number of hits in the pixels, the number of silicon hits (pixels plus SCT) and the transverse impact parameter. The medium cuts increase the jet rejection by a factor of 3-4 with respect to the loose cuts, while reducing the ID efficiency by $\sim$10%.

- **ID "Tight"** makes use of all the particle-ID tools currently available for electrons. In addition to the cuts used in the medium set, cuts are applied on the number of vertexing-layer hits (to reject electrons from conversions), on the number of hits in the TRT, on the ratio of high-threshold hits to the number of hits in the TRT (to reject the dominant background from charged hadrons), on the difference between the cluster and the extrapolated track positions in η_e and ϕ_e , and on the ratio of cluster energy to track momentum.

Forward electrons ($|\eta_e| > 2.5$) can only use information from the calorimeters, which makes it impossible to distinguish between electrons and photons.

Variables used to discriminate between electrons and hadrons are defined as the topological-cluster moments [1] or combinations of them. Electron ID is performed in two $|\eta_e|$ bins: the EMEC-IW and the FCAL using the same cut-based technique. The direction of the electron is defined by the barycenter of the cells belonging to the cluster in the calorimeter. The energy of the electron is determined by the sum of the cluster cells.

The "IsEM" bit mask for forward electrons provides two levels of the ID for the forward electron: "forward loose" and "forward tight" and works in the same way as for central electrons, but the flags used are different.

- **ID "Forward loose"** is based on the cuts which are applied on the distance of each cell to the cluster center along the shower axis, on the radial distance of each cell to the shower axis and on the distance of the shower center from the front of the calorimeter along the shower axis.

- **ID "Forward tight"** in addition to the "forward loose" mask cuts uses cuts on the fraction of the cluster energy that is deposited in the most energetic cell of the cluster, on the lateral and longitudinal moments of the shower taking into account the two most energetic cells.

[1] The cluster moment of degree n for the variable x is defined as: $< x^n >= \frac{1}{E_{\text{norm}}} \times \sum_i E_i x_i^n$, where i is the cell index of the cluster, E_i is the energy in the cell i and $E_{\text{norm}} = \sum_i E_i$.

8.4 Electron isolation (Iso)

There are three types of electron candidates, which can be distinguished by the criteria of the Iso tool [74, 75]: isolated electrons, non-isolated electrons and fake electrons [2, 72]. Decays of the Z and W bosons are potential sources of high $E_{T,e}$ isolated electrons, whereas non-isolated electrons may, for example, originate from decays of B or D mesons. Also hadrons can be misidentified as electron candidates (this is the fake-electron case).

Calorimeter and track-based variables are used to separate isolated electrons from non-isolated electrons and fakes. While the calorimeter is sensitive to both neutral and charged particles, only charged particles contribute to the track-based discriminators. The advantage of the track-based variables lies in the possibility to distinguish between particles that originate from the primary vertex and those from secondary vertices, thus making it more robust against the impact of pileup.

There are two different ways to estimate Iso: using a cut-based discrimination (similar to the one used for electron ID) and using projective likelihood estimators. The projective likelihood estimator combines the separation power of a set of discriminating variables in one single variable r, defined as follows:

$$r = \ln \frac{p_S}{p_B} \sim \sum \frac{p_S^{var}(x_{var})}{p_B^{var}(x_{var})}\,, \tag{8.1}$$

where p_S and p_B are the signal and background probabilities and $p^{var}(x_{var})$ and $p^{var}(x_{var})$ denote the probabilities for the variable var to take a given value x_{var} in case of a signal and background electron, respectively.

The dedicated multivariate tools implementing Iso algorithm have two input parameters: type of Iso and tightness.

Possible types of Iso:

- **"IsoElectron_Jet"**: separation between isolated electrons and jets,
- **"IsoElectron_NonIsoElectron"**: separation between isolated electrons and non isolated electrons (from heavy quark decays),
- **"IsoPhoton_Jet"**: separation between isolated photons and jets.

Possible tightness:

- **"Iso99"**: cuts on calo and track Iso variables,
- **"CaloIso98"**: cuts on calo Iso variables,
- **"trackIso99"**: cuts on track Iso variables,
- **"likelihoodIso95"**: cuts on likelihood ratios.

where the numbers show the expected efficiency of the cut in %. The electron Iso "CaloIso98" was recommended by "e/gamma" group to use for analyses in the electron channel, since it provide sufficient background rejection.

CHAPTER 9

Event Selection

The event selection is performed in two steps: pre-selection and basic selection, which are described in the first two sections of this chapter. The pre-selection reduces total number of events in data sample and amount of information per each event in order to perform analysis faster. Basic event selection is used to select $Z \to e^+e^-$ signal and suppress background. The last section of this chapter describe the corrections applying to each event in data or MC samples.

9.1 Data pre-selection

The "e/gamma" stream of the 2010 ATLAS data sample contains about 2×10^8 events, which requires about 50 TB disc space (about 0.25 MB per event). Most of these events are not relevant for $Z \to e^+e^-$ analysis, and a pre-selection procedure is applied in order to reduce the data sample and to speed up the analysis.

The pre-selection is performed in two steps. The first step reduces the total number of events in the data sample. It is performed by the "DPD Maker" tool which is a part of Athena [76]. The algorithm applies several selection criteria to the data, where AOD files are used as an input. The output of the pre-selection have the same AOD format with exactly the same amount of information per event.

For the current $Z \to e^+e^-$ analysis the following list of cuts was applied in the pre-selection:

- GRL: WZjets_allchannels (see Sec. 5),
- The event must contain at least one reconstructed electron with $p_{T,e} > 15$ GeV which is identified as "Medium",
- The event must contain at least two EM clusters with $p_{T,e} > 15$ GeV.

The event rejection factor of this pre-selection is ∼100-150. The selected events are stored in D2PD files. The overall output has 1.3 M events (320 GB of disk space).

The second level of the pre-selection is performed using the analysis package ZeeD, described in Sec. 10.3. This pre-selection keeps all events, but stores only information relevant for $Z \to$

e^+e^- reconstruction using a dedicated TTree format. The final pre-selected 2010 data sample requires 1.3 GB (around 1 KB per event) of disc space and only 15 minutes to run on the NAF farm (German computer center [77]). These pre-selected data sample contains all necessary information to perform electron ID and Iso efficiency studies, the EM calibration and the cross-section calculation as presented in this thesis.

9.2 Basic event selection

The main purpose of the event selection is to suppress as much background as possible while keeping as much signal as possible. Since the ATLAS trigger system covers only the central part of the detector ($|\eta_e| < 2.5$), there are two different $Z \to e^+e^-$ analyses performed: a so-called Central-Central (CC) analysis, based on two electrons in central region, and a Central-Forward (CF) analysis, which requires one central electron and one forward electron ($2.5 < |\eta_e| < 4.9$).

The kinematic selection for both analyses is presented in Tab. 9.1 and defines the phase space in which the cross section is measured. The kinematic selection closely follows the fiducial volume defined in section 7.1. Compared to the definition of the fiducial volume, which is performed using generated event quantities, the kinematic selection is based on the reconstructed four-vectors. A threshold of 20 GeV for transverse energy of the electrons was chosen in order to get a trigger efficiency close to 100%. The central region is limited to $|\eta_e| < 2.47$ to stay well inside the central tracker acceptance. Di-electron mass window [66-116] GeV was chosen symmetrically with respect to the known mass of Z boson (~ 91 GeV).

CC $Z \to e^+e^-$	CF $Z \to e^+e^-$
both electrons	central electron: $\lvert\eta_e\rvert < 2.47$
$\lvert\eta_e\rvert < 2.47$	forward electron: $2.5 < \lvert\eta_e\rvert < 4.9$
the crack region $1.37 < \lvert\eta_e\rvert < 1.52$ is excluded for both electrons	
both electrons have $p_{T,e} > 20$ GeV	
$66 < M_{ee} < 116$ GeV	

Table 9.1: Kinematic selection for the CC and the CF analyses.

The full selection for the CC and CF analyses is listed below:
CC Z boson selection:

- CC kinematic selection (see Tab. 9.1),
- dead OTx region excluded for both electron candidates,
- the event has at least 1 primary vertex with at least 3 tracks,
- the event has exactly two electrons, which are identified as "medium" and satisfy the kinematic selection.

- each electron candidates is reconstructed by cluster-based algorithm (author=1),
- the event is triggered by L1_EM14 or EF_Medium_15,

CF Z boson selection:

- CF kinematic selection (see Tab. 9.1),
- dead OTx region excluded for both electron candidates,
- the event has at least 1 primary vertex which has at least 3 tracks,
- the event is triggered by L1_EM14 or EF_Medium_15,
- the event has exactly two electrons which satisfy kinematic selection: central is identified as "medium" while forward is identified as "forward loose",
- the central electron candidate must be reconstructed by the cluster-base algorithm (author=1), and the forward electron by the forward algorithm (author=8),
- the central electron candidate must pass Iso criteria "CaloIso98".

Both lists include the OTx cut (see Sec. 9.2.1) and the trigger L1_EM14 for periods B-E3 or EF_E15_medium for periods E4-I2. The author cut selects the proper reconstruction algorithm for the electrons. The electron quality cuts (ID and Iso) are used to reject fake electrons from jets and were chosen with respect to their efficiencies. The Iso cut "CaloIso98" was chosen for this analysis, since it is highly efficient for the signal while providing significant background suppression. In the following text it will be noted as "Iso cut". Various presented measurements such as the efficiency or the calibration require modifications of analysis selection, like relaxing of the invariant-mass cut. Explicit lists of cuts are provided for all presented studies.

9.2.1 Problematic regions of the EM calorimeter

During the data taking some cells of the EM calorimeter were not fully functional. This information is summarized in $\eta_e - \phi_e$ dependent Object Quality maps (OQ maps). Each cell can have one of the following types:

- type 1: The cell is functioning correctly,
- type 2: The cell has non-nominal high voltage,
- type 3: The cell has a major problem.

This map is different for different ranges of runs. In order to have the smallest possible systematic uncertainty due to the different quality of EM objects in data and MC, only the tightest map, which corresponds to the last run, is used in analysis. In this map maximum cells of the calorimeter are labeled by type 3 or 2. The quality of the electrons is not affected if it was reconstructed in cell has the type 2, since the appropriate correction factors are applied in the reconstruction. Therefore, the electrons which were reconstructed in cells with the type 1 or 2 are used in the analysis. The cut which rejects electron in cells with the type 3 is called OTx.

9.3 Calculation of the event corrections

As it was discussed in Sec. 6.3 and Sec. 6.4 the MC samples are always reweighted in $p_{T,Z}$ and $N_{\rm vtx}$ using the corresponding scale factors $SF_{p_{T,Z}}$ and $SF_{N_{\rm vtx}}$. Therefore the scale factor, which is applied for generated information (generated event weight $SF_{\rm gen}$) in each event in the MC samples, is calculated as:

$$SF_{\rm gen} = SF_{p_{T,Z}} \times SF_{N_{\rm vtx}} \times SF_{\rm initial}, \tag{9.1}$$

where $SF_{\rm initial}$ is an event weight read from the AOD file.

In order to extract cross sections with minimum systematic uncertainties, the simulated samples which are used in the calculation, have to describe detector effects. The selection criteria, which are applied for the electrons, could have different efficiencies (fraction of the $Z \to e^+e^-$ electrons passing criteria) in data and MC. In order to minimize these differences the electron reconstruction $\varepsilon_{\rm Reco}$, ID $\varepsilon_{\rm ID}$, Iso $\varepsilon_{\rm Iso}$ and trigger (TG) $\varepsilon_{\rm TG}$ efficiencies should be corrected in MC samples (see Sec. 13).

Each correction factor is applied as a scale factor (SF) in the event and is calculated as a ratio $\varepsilon^{\rm data}/\varepsilon^{\rm MC}$.

For the CC analysis, the electron reconstruction ($SF_{\rm Reco}$) and ID "medium" ($SF_{\rm ID\_medium}$) SFs are multiplied for both electrons. Since the trigger selects events using only one central electron, the trigger ($SF_{\rm TG}$) SF is applied as $1-(1-SF^{e1}_{\rm TG})(1-SF^{e2}_{\rm TG})$, where $SF^{e1}_{\rm TG}$ and $SF^{e2}_{\rm TG}$ are the SFs calculated for the first and second electron.

For the CF analysis, the trigger ($SF_{\rm TG}$) and electron reconstruction ($SF_{\rm Reco}$) SFs are multiplied for the central electron. The ID "tight" ($SF_{\rm ID\_tight}$) SF for the central electron and the ID "forward loose" ($SF_{\rm ID\_loose}$) SF for the forward electron are multiplied together with Iso ($SF_{\rm Iso}$) SF for the central electron.

The total efficiency correction for the CC ($SF_{\rm CC}$) and CF ($SF_{\rm CF}$) selections is calculated for each event as:

$$\begin{aligned} SF_{\rm CC} &= SF^{e1}_{\rm Reco} \times SF^{e2}_{\rm Reco} \times SF^{e1}_{\rm ID\_medium} \times SF^{e2}_{\rm ID\_medium} \times (1-(1-SF^{e1}_{\rm TG})(1-SF^{e2}_{\rm TG})) \times SF_{\rm gen}; \\ SF_{\rm CF} &= SF^{e_{\rm center}}_{\rm Reco} \times SF^{e_{\rm center}}_{\rm TG} \times SF^{e_{\rm center}}_{\rm Iso} \times SF^{e_{\rm center}}_{\rm ID\_tight} \times SF^{e_{\rm forward}}_{\rm ID\_loose} \times SF_{\rm gen}. \end{aligned} \tag{9.2}$$

The di-electron mass resolution in the MC samples should be in agreement with the data. The electron energy smearing is applied to the energy of each electron in the MC samples as $E' = E(1+Gaus(0,SmF))$, where the $Gaus(0,SmF)$ is a Gaussian random number with mean equal to 0 and standard deviation equal to SmF. The Smearing Factor (SmF) was calculated in order to minimize differences in the di-electron mass resolution in data and MC (see Sec. 12).

The electron energy calibration is applied to the energy of each electron in the data sample as a scale for electron energy: $E' = E/(1+\alpha)$, where α is an η_e-dependent scale factor.

The pileup effect (see Sec. 6.4) needs to be well described in MC as well. The uncertainties of these corrections are propagated to the cross-section uncertainty.

CHAPTER 10

Analysis tool (ZeeD)

The analysis presented here is performed using a tool called ZeeD ($Z \to e^+e^-$ DESY) [78]. Since ZeeD is an ATHENA-based tool, it is able to use all ATHENA services. The cross-section measurement, unfolding, efficiency calculation, background estimation and calibration can be done by ZeeD in parallel.

ZeeD can use several input formats: AOD (D2PD) samples, "ZeeD TTree" or "ZeeD Inline". ZeeD TTree is a ROOT TTree which is produced by the ZeeD pre-selection (see Sec. 10.3). This output format provides a factor of 10 CPU improvement and factor of 200 disc space reduction compared to AOD. "ZeeD Inline" is a fast inline event generator which can be used in cases where large statistic is needed and high precision is not required (see Sec. 10.2).

10.1 Analysis chain

Since ZeeD is an ATHENA algorithm, it has an "initialize", "execute" and "finalize" part. "Initialize" includes the initialization of all internal variables and ATHENA services. Also the loading of all necessary input information, like cut thresholds, tables and histograms with efficiencies and other corrections is performed at this step. The "execute" part performs the analysis event by event. At the "finalization" step all histograms and trees are written to the output file.

When running the main ZeeD algorithm on the NAF farm, all output files are summed by the "hadd"[1] ROOT script. In the last step of the analysis additional ZeeD algorithms or ROOT scripts perform final calculations (post-processing) and produce figures using the recommended ATLAS style.

10.1.1 Event reconstruction with the ZeeD algorithm

At the beginning of the analysis, ZeeD fills all necessary event information into internal variables: reconstructed tracks and clusters of electrons, primary vertex information and also generated information if running over MC-simulated samples. This filling can be done from several sources: AOD, TTree or Inline.

[1] "hadd" is a simple script which allows to merge a few ROOT files and requires $\sim$ one minute of CPU time.

Before calculating the electron four-vectors, the smearing and calibration corrections are applied. The next step is the calculation of electron four-vectors. Since the angular resolution of the tracker is higher than the one from the calorimeter, the electron four-vector is normally calculated using both tracker and cluster information. If the electron has both a cluster and a good[1] track, then the track angles θ^{tr} and ϕ^{tr} and cluster energy E^{cl} and momentum P^{cl} are used in the electron four-vector $FV_e(p_x, p_y, p_z, E)$, which is calculated as:

$$\begin{aligned} p_x &= P^{cl} \sin(\theta^{tr}) \cos(\phi^{tr}), \\ p_y &= P^{cl} \sin(\theta^{tr}) \sin(\phi^{tr}), \\ p_z &= P^{cl} \cos(\theta^{tr}), \\ E &= E^{cl}. \end{aligned} \tag{10.1}$$

If only cluster information are available then the cluster four-vector is used as an electron four-vector.

As a next step, a list of all possible ("loose") Z bosons is created. This list contains combinations of all possible electron pairs, and the four-vector (FV_Z) of the Z boson is calculated as:

$$FV_Z = FV_{e1} + FV_{e2}. \tag{10.2}$$

In order to speed-up the analysis and make the list of Z bosons shorter, a so-called loose invariant mass cut is applied. This invariant-mass cut has a threshold same or looser than the one that is used for the analysis.

Several different analyses (the CC and CF in this thesis) can be run simultaneously in ZeeD. All next steps are repeated for each analysis.

The first step, which depends on the analysis selection, is a selection of a "best" Z boson from the list of "loose" Z bosons. Each analysis has a list of the selection criteria which are applied for each "loose" Z bosons with a weight (see Tabs. 10.1 and 10.2). The "best" Z boson is a boson which passes more criteria than the others (taken into account weights). Each analysis has always only one "best" Z boson per event if the list of "loose" Z bosons is not empty. If a given event has two "best" Z bosons, only first of them is signed as the "best" (it is not essential for cross-section calculation, because de-facto both CC and CF selections reject events with more than one "best" Z boson). However, for some studies like the efficiency calculation or background studies it could be significant. For the presented analysis, in case of more than one "best" Z boson, the boson with highest sum of the transverse momentum of the electrons $p_{T,e1} + p_{T,e2}$ is finally signed as the "best".

After the "best" Z boson is selected a list of event criteria is calculated. ZeeD has a long list of criteria for Z bosons, its electrons and event parameters. Each criterion is implemented as a function which returns a boolean: true — event passed, false — event failed. Finally all boolean variables are filled in a cut bit mask.

[1] Electron tracks are called "good" if they have more than 3 SCT and pixel hits.

Cut	weight
$66 < M_{ee} < 116$ GeV	10
Both electrons $p_{T,e} > 20$ GeV	1
Both electrons $\|\eta_e\| < 2.47$	20
Crack $1.37 < \|\eta_e\| < 1.52$ excluded	1
Both electron ID "medium"	1
Electrons have opposite charge	1
OTx	1
Both electrons are Electron Author	1

Table 10.1: Selection criteria which are applied in order to select the "best" Z boson in a list of "loose" Z bosons for the CC analysis.

Cut	weight
$66 < M_{ee} < 116$ GeV	10
Both electrons $p_{T,e} > 20$ GeV	1
central electron $\|\eta_e\| < 2.47$, forward electron $2.5 < \|\eta_e\| < 4.9$	20
Crack $1.37 < \|\eta_e\| < 1.52$ excluded	1
central electron ID "tight"	1
forward electron ID "forward loose"	1
OTx	1
central electron is Electron Author forward is Electron Forward	1
central electron is Isolated with "CaloIso98"	1

Table 10.2: Selection criteria which are applied in order to select the "best" Z boson in a list of "loose" Z bosons for the CF analysis.

As the next step, the event weights are calculated (see Sec. 9.3).

In the final step the filling of histograms is performed. The lists of histograms, which are usually related to certain analysis (the cross-section calculation, acceptance measurement, efficiency measurement and so on) or to groups of variables (Z boson variables, electrons variables and so on) are stored in C++ classes, called ZeeD histogram managers. Each of this classes inherits from the cut histogram manager class, which has a list of cuts and the name of the histogram manager as parameters of the constructor. If all of these cuts are satisfied, the histograms of the corresponding histogram manager are filled.

This approach allows to perform several studies: i.e. calibration, efficiency measurement, bin-migration studies, and so on. The reconstructed and generated event quantities are filled in the histograms with reconstructed and generated event weight, respectively.

All systematic uncertainties for the given analysis can be estimated running the main anal-

ysis in ZeeD. For this reason raw event information is kept and this copy is used several times for each systematic. The calculation of systematic uncertainties introduce modification to variables such as energy of the electrons, efficiency corrections, pileup corrections and so on.

10.1.2 Cut flow performance

Apart from the histogram managers, additional histograms filled with the cut bit mask information are stored in ZeeD. One of them is used for cut rejection studies. An example of this histogram for the CC selection performed on MC samples is presented in Fig. 10.1 and shows the numbers of events which were rejected by individual cuts.

Another histogram stores the cut bit mask itself and can provide full cut flow information (i.e. the cut flow of any possible set and sequence of cuts). The ZeeD cut bit mask with N_{cuts} can have $2^{N_{\text{cuts}}}$ different values. The histogram, which stores all of these values, has $2^{N_{\text{cuts}}}$ bins and can therefore provide full cut flow information.

The cut flow for both CC and CF selection is presented in Tab. 10.3, for different sequence of cuts. It is apparent from the table that for both analyses the main background rejection occurs at Electron ID requirement. The trigger cut also rejects significant amount of background events if it is applied before the electron ID cut, however if it is applied after it there is very little loss from the trigger requirement.

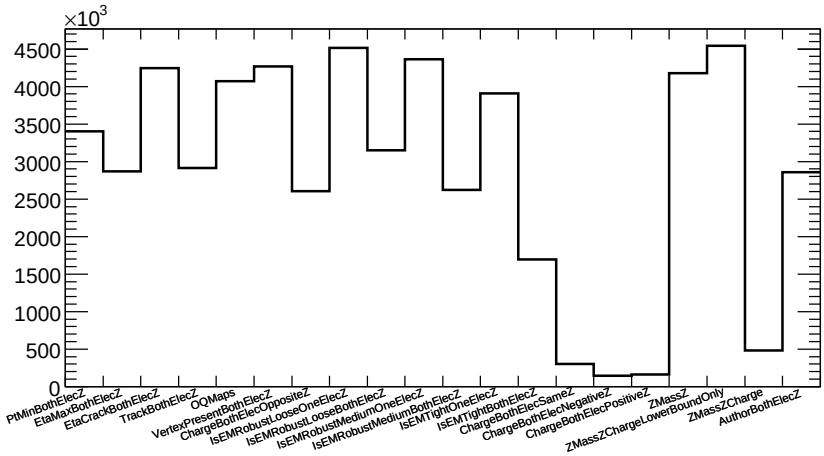

Figure 10.1: An example of the histogram for cut rejection studies, which shows the numbers of events rejected by individual cuts.

10.2 Inline generator

The ZeeD inline generator is a fast generator implemented in ZeeD as a C++ class. The input to the generator are histograms of $p_{T,Z}$ and y_Z distributions which were calculated using one of the recent proton PDFs. Generation starts from the randomly generated Z kinematic variables: flat ϕ_Z, $p_{T,Z}$ and y_Z generated using the shapes of the histograms as a probability function, M_Z generated using a Breit-Wigner function. These values allow to construct the Z four-vector,

Cut:	N_{evt} CC selection	N_{evt} CF selection
pre-selection	1.34M	1.34M
kinematic cuts	87.0K	56.1K
OTx	77.4K	53.3K
Author	74.0K	53.0K
Trigger	48.3K	34.7K
Electron ID	9998	3882
Vertex requirenment	9996	3881
Isolation	Not applied	3377
Opposite charge	9725	Not applied
pre-selection	1.34M	1.34M
kinematic cuts	87.0K	56.1K
Electron ID	11.1K	4225
Isolation	Not applied	3708
Opposite charge	10.6K	Not applied
OTx	9807	3418
Author	9731	3412
Trigger	9727	3378
Vertex requirenment	9725	3377

Table 10.3: Cut flow for the CC and CF analyses, with different sequence of the selection criteria. All cuts are described in Sec. 9.2.

$FV_Z(p_x, p_y, p_z, E)$, where:

$$\begin{aligned} p_x &= p_{T,Z}\cos(\phi_Z), \\ p_y &= p_{T,Z}\sin(\phi_Z), \\ p_z &= E\frac{e^{2y_Z}-1}{e^{2y_Z}+1}, \\ E &= \sqrt{\frac{M_Z^2 + p_{T,Z}^2}{\frac{4*e^{2y_Z}}{(e^{2y_Z}+1)^2}}}. \end{aligned} \tag{10.3}$$

Then two electrons with energy $E = M_Z/2$ and random momentum P ($P_{e1} = -P_{e2}$) are generated. Each of these electrons is boosted in order to match the generated Z boson. In addition, several smearing corrections can be applied.

Firstly, the PHOTOS (see Sec. 6.1) package is used to add QED radiation to the Z decay process. In addition a few % of energy smearing is applied in order to provide reasonable agreement with the full MC. Fig. 10.2 shows a comparison of the di-electron mass distribution for an MC sample and the ZeeD inline generator. Stages of smearing correction are shown in different colors.

For the simulation of detector effects an efficiency table, which contains the probabilities of the electron ID in bins of η_e and as calculated by full MC sample, is used.

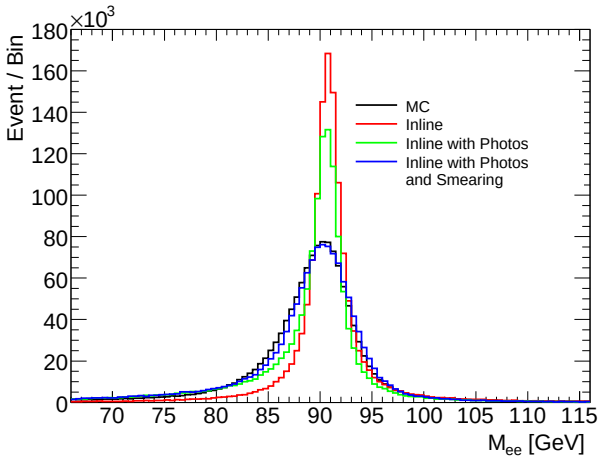

Figure 10.2: Comparison of the di-electron mass distribution between ZeeD inline generator and $Z \to e^+e^-$ MC@NLO generator. Red: pure inline generator, green: inline generator with photon radiation, blue: inline generator with photon radiation and smearing.

The inline generated Z boson and electrons before smearing corrections are used as a generated information for analysis. The electrons with QED radiation, smearing and simulation of the detector effects are used as reconstructed information.

10.3 Pre-selection

ZeeD pre-selection performs the second level of the pre-selection, which stores only the information relevant for the analyses and do not reduces a number of events. This pre-selection is implemented as a histogram manager, which stores internal ZeeD variables in a ROOT TTree. TTree input files are used by the same way as AOD files, but require less CPU time to access variables. These TTrees also can be browsed by standard ROOT tools.

10.4 Post-processing

In the post-processing step in ZeeD, the variables relevant for the analysis are calculated and studies such as calibration, background estimation and others are performed using ROOT scripts or additional ZeeD algorithms. This performance includes simple arithmetics with histograms their fitting as well. The tables and figures which are presented in this thesis are created at the ZeeD post-processing step.

CHAPTER 11

Background studies

Even after the full selection, the final event sample contains background contributions from non $Z \to e^+e^-$ events. The background is significantly higher for samples with relaxed ID selection criteria. This chapter present study of the background and discusses various methods of the background subtraction.

11.1 Methods of background estimation

All sources of background can be conventionally split in two: EW, including contributions from $t\bar{t}$ production and QCD. The sources of EW background are listed in Tab. 6.1. They have relatively small cross sections (comparable with the cross section for the $Z \to e^+e^-$ process) and therefore can be simulated by MC with sufficient statistics. The EW background contribution is generally small, and exact numbers are taken directly from MC for both the CC and the CF analysis.

Since QCD background, which comes from hadronic jets, has the cross section 6 orders of magnitude higher than the cross section of the EW processes and could not be simulated by MC with sufficient statistics, data-driven method are used to estimate its contribution as it is discussed below. The QCD background arises mostly from the misidentification of jets as isolated electrons. There is also a non-negligible contribution from non-isolated leptons, arising from the semileptonic decays of b or c hadrons or mesons, from $\pi^0 \to e^+e^-\gamma$ decays and from photon conversions and shower fluctuations.

The region under the di-electron mass peak has an enhanced signal contribution with respect to the side bands. Therefore the peak region is used to normalize the signal while the mass side bands are used to estimate the background contribution. Two fit methods, described below, are implemented to separate signal and background.

- **RooFit method.** The signal and background contributions are estimated by fitting the di-electron invariant mass shape using the RooFit framework [46]. The shape of the signal component is approximated by a convolution of a Crystal-Ball and a Breit-Wigner function. Several functions are used for the approximation of the background shape (see Sec. 11.3). The fit can be performed globally and in bins of $|y_Z|$. The fit mass

ranges are taken to be larger than the analysis mass range to increase the background contamination and therefore to increase the statistical precision of its determination. Different fit functions for the background description and different fit ranges are used for evaluation of systematic uncertainties.

- **Template fit method.** The similar fitting procedure is used for estimation of the signal and background contributions, however the shape of the signal and background, which are used for the fitting are different. The shape of the di-electron mass distribution for the signal component is taken from the signal MC after full analysis selection. The shape for background is taken from data, passing the same kinematic selection but inverting some of the ID and Iso criteria. The remaining signal component after this inverted selection is significantly suppressed and could be estimated by the signal MC with the same selection and then subtracted. In this method the signal is fitted under the di-electron mass peak (around [80-100] GeV region) while the background is fitted in the side bands (for example [60-80] GeV and [100-120] GeV). Various signal regions and various background templates are used for an evaluation of the systematic uncertainty.

In both approaches the EW background is estimated by MC and subtracted from the data before fitting. The RooFit method does not require any signal MC samples and is more robust for samples with large statistical uncertainties than the template method: If the template method is used in $|y_Z|$ bins adopted in the analysis, the statistical uncertainty for the background estimation reaches 50%.

To overcome the statistical limitations, the template method can be applied to the complete un-binned analysis sample to determine the background normalization. The background contribution in bins of $|y_Z|$ is then determined from the shape of the background template in $|y_Z|$. This approach has an additional systematic uncertainty for individual bins since the cut-inverted background sample may not follow the same $|y_Z|$ distribution compared to the nominal selection. In all methods, the total number of QCD events determined from the fit of the un-binned sample and the sum of background events determined in $|y_Z|$ bins are required to be the same for consistency.

11.2 EW background in $|y_Z|$ bins

Several component of the EW background are presented in Tabs. 11.1 and 11.2 for the CC and CF selections, respectively. The largest contributions for the CC selection come from the $t\bar{t}$, $W \to e\nu$ and $Z \to \tau\tau$ processes and smaller contribution from di-boson production. For the CF selection the dominant contribution comes from $W \to e\nu$ events, while the contribution from $t\bar{t}$, $Z \to \tau\tau$ and di-bosons is less significant.

The systematic uncertainty of the cross sections for these processes is about 10%. Therefore the total EW background uncertainty is quite small for the final result. Fig. 11.1 presents a comparison of the di-electron mass distribution between the data and MC, including all

background contributions. The signal and all background MC are normalized to the data luminosity. The shape of the QCD background are extracted from the data and normalized to number of the QCD background events (see next sections). The EW and QCD backgrounds are added to the signal MC histogram.

$\|y_Z\|$	$W \to e\nu$	$W \to \tau\nu$	$Z \to \tau\tau$	$t\bar{t}$	WW	WZ	ZZ	Sum
0.00–0.40	2.4	0.0	1.3	4.1	0.7	1.9	1.3	$11.7 \pm 0.3 \pm 0.7$
0.40–0.80	2.8	0.2	1.8	3.7	0.6	1.7	1.3	$12.1 \pm 0.3 \pm 0.7$
0.80–1.20	1.6	0.2	1.4	2.4	0.5	1.6	1.1	$8.8 \pm 0.2 \pm 0.5$
1.20–1.60	1.8	0.1	1.0	1.4	0.4	1.1	0.8	$6.6 \pm 0.1 \pm 0.4$
1.60–2.00	1.9	0.0	0.6	0.5	0.2	0.6	0.5	$4.3 \pm 0.1 \pm 0.3$
2.00–2.40	1.0	0.2	0.3	0.1	0.1	0.3	0.2	$2.2 \pm 0.0 \pm 0.1$
Total	11.5	0.7	6.4	12.2	2.5	7.2	5.2	$45.7 \pm 1.0 \pm 2.7$

Table 11.1: Number of the EW background events for the CC analysis with statistical and systematic uncertainties are given in bins of $|y_Z|$.

$\|y_Z\|$	$W \to e\nu$	$W \to \tau\nu$	$Z \to \tau\tau$	$t\bar{t}$	WW	WZ	ZZ	Sum
0.80 - 1.20	1.1	0.0	0.0	0.0	0.0	0.0	0.0	$1.1 \pm 0.0 \pm 0.1$
1.20 - 1.60	6.9	0.2	0.2	0.6	0.1	0.1	0.0	$8.1 \pm 0.3 \pm 0.4$
1.60 - 2.00	14.7	1.6	0.7	1.0	0.4	0.3	0.1	$18.8 \pm 0.7 \pm 1.0$
2.00 - 2.40	12.9	1.3	1.4	0.8	0.3	0.5	0.3	$17.5 \pm 0.6 \pm 0.9$
2.40 - 2.80	10.2	0.9	1.6	0.3	0.2	0.4	0.2	$13.8 \pm 0.5 \pm 0.7$
2.80 - 3.60	1.9	0.2	0.5	0.0	0.0	0.1	0.1	$2.8 \pm 0.1 \pm 0.1$
Total	47.7	4.2	4.4	2.7	1.0	1.4	0.7	$62.1 \pm 2.3 \pm 3.3$

Table 11.2: Number of the EW background events for the CF analysis with statistical and systematic uncertainties are given in bins of $|y_Z|$.

11.3 Study of the QCD background

The shape of the di-electron mass distribution for the QCD background events depends on the selection criteria and may vary for different analysis bins. Precise knowledge of the background shape is necessary to set starting values and limits of the parameters for background functions in the RooFit method and to find proper templates for the template method. If the selection of the background template is close to the analysis selection (almost all cuts the same), then its shape is also close to the background shape in the nominal selection, nevertheless it may have insufficient statistics and could have a large signal contamination. In addition, for all

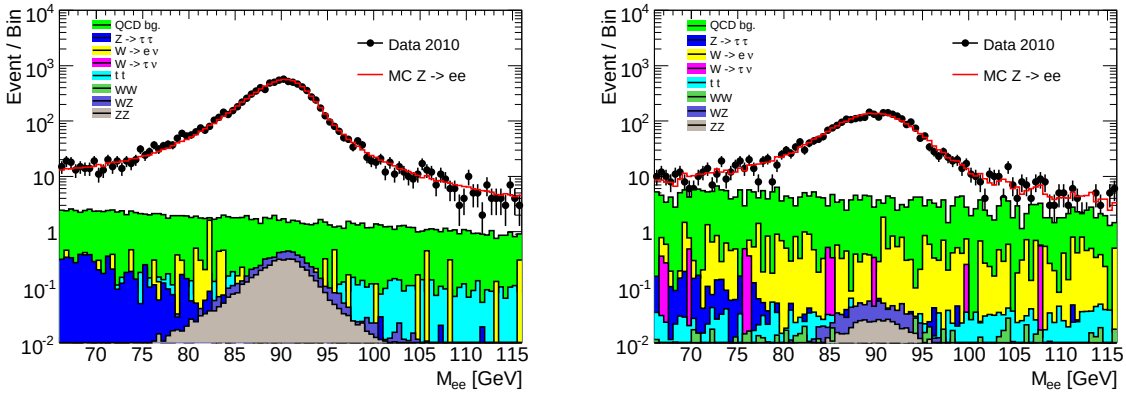

Figure 11.1: Comparison of the di-electron mass distribution for data and MC for the CC (left) and the CF (right) selections. The signal and all background MC are normalized to the data luminosity. All presented QCD and EW background events are added to the signal MC signal histogram.

background selections at least one electron must fulfill the ID "medium" cut, since it is required in the trigger.

Several background selections for the CC and CF analyses with different ID and Iso cuts are listed below:

Background selections for the CC analysis:

- **CCbg1**: one electron fails ID "medium", the other passes ID "medium", same-charge requirement,
- **CCbg2**: one electron fails ID "medium", the other passes ID "medium",
- **CCbg3**: one electron fails ID "medium", the other passes ID "medium" but fails "CaloIso98".

Background selections for the CF analysis:

- **CFbg1**: center electron passes ID "medium", forward fails ID "forward loose",
- **CFbg2**: center electron passes ID "medium" and "CaloIso98", forward fails ID "forward loose",
- **CFbg3**: center electron passes ID "medium" but fails "CaloIso98", forward fails ID "forward loose".

Fig. 11.2 shows a comparison of the di-electron invariant mass distribution for each background selection. A fraction of the remaining signal in each background selection was simulated by the signal MC with the same selection and subtracted. All presented shapes are quite similar, especially for the CC analysis.

The CC analysis selection requires electrons with opposite charges. This cut, if it is used for the background selection, potentially could change the background shape. However, the same-charge requirement for the background selections gives additional signal suppression, which allows to get more clear background sample.

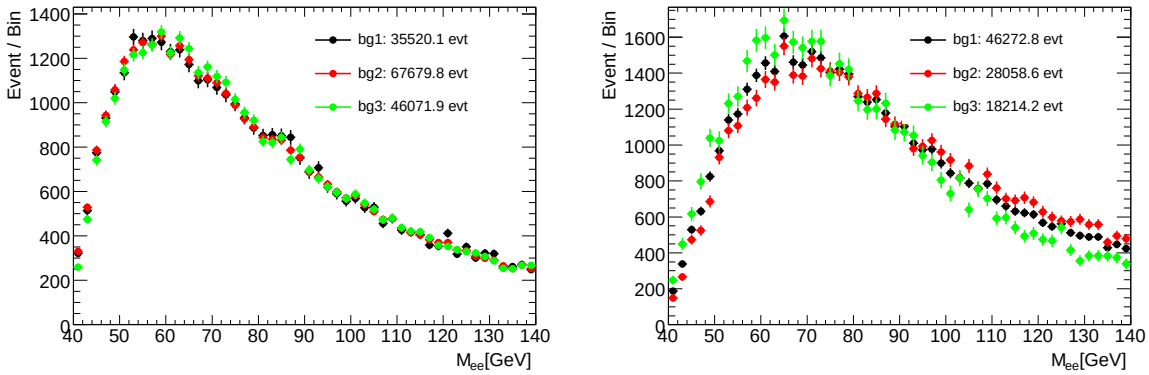

Figure 11.2: Comparison of the di-electron mass distributions for data with different background selections for the CC (left) and the CF (right) analyses. A fraction of the remaining signal in each background selection was simulated by the signal MC with the same selection and subtracted. All distributions are in reasonable agreement, especially for the CC analysis.

A comparison of the same-charge with opposite-charge backgrounds for the CC analysis is shown in Fig. 11.3. The left and right panels correspond to the CCbg2 and CCbg3 background selections, respectively. Fig. 11.3 shows similar shape for all selections, while the number of events is slightly (order of 7-9%) different. Since all of the presented histograms are similar, each of them could be used for background estimation. The background selection without charge requirement will be used for further studies, in order to have increased statistics.

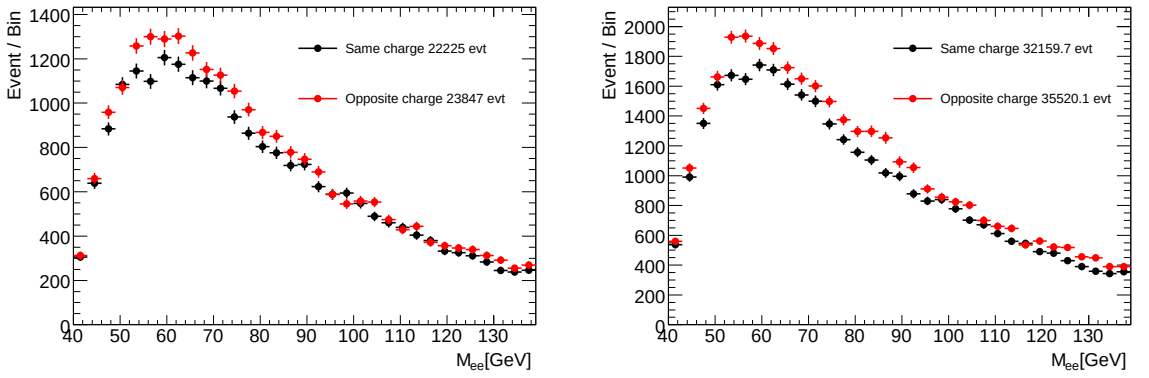

Figure 11.3: Comparison of the di-electron mass distributions between data with same-charge and data with opposite-charge background selections. A fraction of the remaining signal in each background selection was simulated by the signal MC with the same selection and subtracted. The left and right panels correspond to background selections CCbg2 and CCbg3 respectively.

To get additional background suppression, analyses are often performed with an increased $p_{T,e}$ threshold. Fig. 11.4 shows a comparison of the background distributions with different cuts on $p_{T,e}$. Left and right panels correspond to background selections CCbg3 and CFbg1 respectively. All histograms are normalized to have the same amount of events for $m_{ee} > 90$ GeV. The low-mass tails of these distributions are different with a significantly stronger suppression

for the sample with the higher $p_{T,e}$ threshold. This $p_{T,e}$ dependence of the background distributions needs to be taken into account during the fitting of the background shape using the RooFit method.

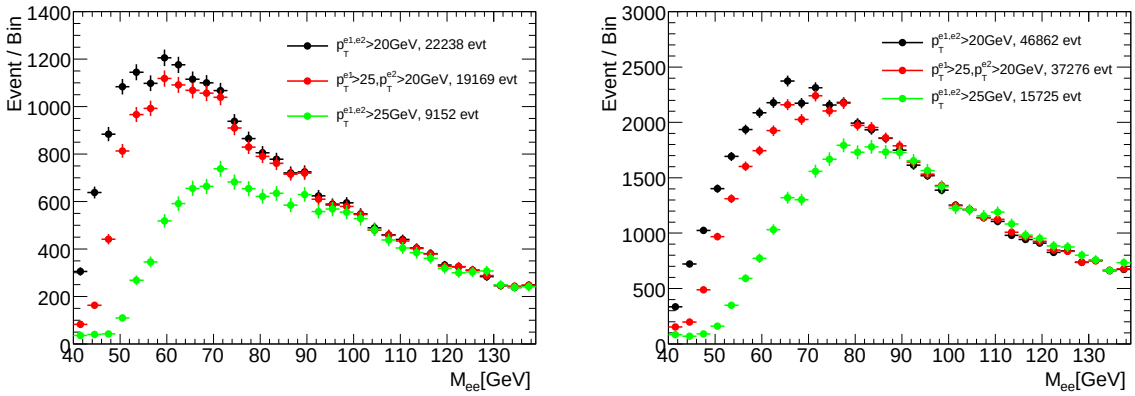

Figure 11.4: Comparison of the di-electron mass distributions for data with different electron $p_{T,e}$ cut for the CCbg3 (left) and CFbg2 (right) background selections. A fraction of the remaining signal in each background selection was simulated by the signal MC with the same selection and subtracted.

A comparison of the di-electron mass distribution in different di-electron rapidity bins is presented in Fig. 11.5. The peak positions of these distributions are different, which also must be taken into account by the RooFit method. Thus the fit parameters have to be selected separately for each bin and have to depend on the $p_{T,e}$ threshold.

Several fit functions were used for the RooFit method for background:

- Landau function: $f(x) = \int_{c-i\infty}^{c+i\infty} e^{s\log(s)+xs} ds$, where $s = \frac{x-x_0}{\sigma}$,
- Exponential function: $f(x) = e^{ax}$,
- Chebychev polynomials: $f(x) = 1 + \sum_{i=1}^{n} a_i T_i(x)$, n=3 ,
- RooDecay function: $f(x) = e^{-\frac{x}{t}} \otimes e^{-0.5(\frac{x-m}{s})^2}$, where $\otimes$ is the convolution.

Several examples of fits to background shapes for different $|y_Z|$ regions are shown in Fig. 11.6 for the CCbg2 background selection and Fig. 11.7 for the CFbg1 background selection. The Landau and RooDecay functions show good agreement with the histograms. The Exponential function can be used only in the plateau region, for di-electron masses larger than 60 GeV. The Chebyshev polynomials with n=3 fail to fit the background shape for most of the $|y_Z|$ bins.

11.4 QCD background in $|y_Z|$ bins

11.4.1 Background for CC $Z \to e^+e^-$ selection

Tab. 11.3 shows a comparison of the number of QCD background events estimated by different methods. As expected, the RooFit method shows smaller statistical uncertainty (estimated by

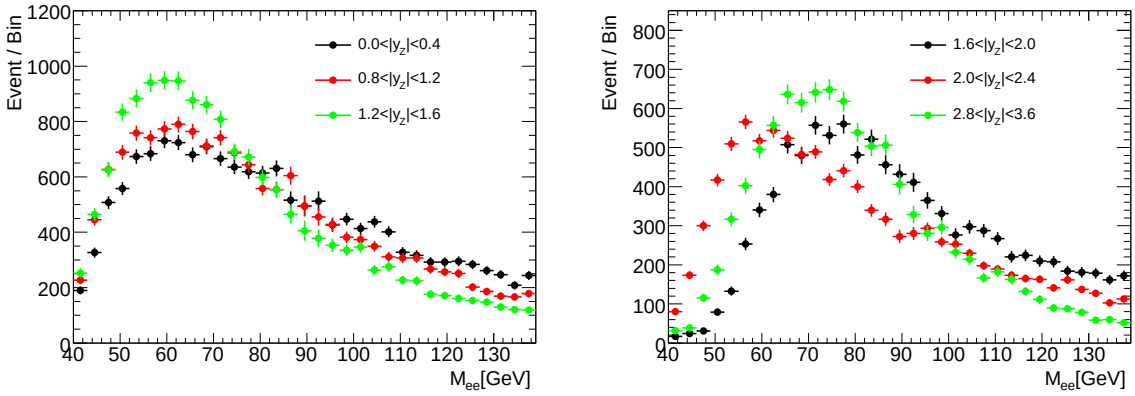

Figure 11.5: Comparison of the di-electron mass distributions for data in different $|y_Z|$ bins for the CCbg2 (left) and CFbg1 (right) background selections. A fraction of the remaining signal in each background selection was simulated by the signal MC with the same selection and subtracted.

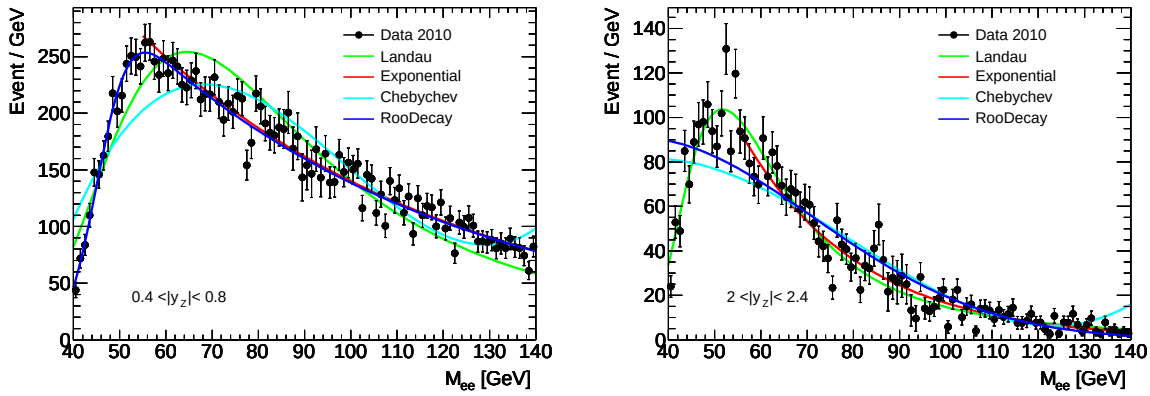

Figure 11.6: Comparison of different fits of the di-electron mass distributions for data in different $|y_Z|$ bins for the CCbg2 background selection. A fraction of the remaining signal in each background selection was simulated by the signal MC with the same selection and subtracted.

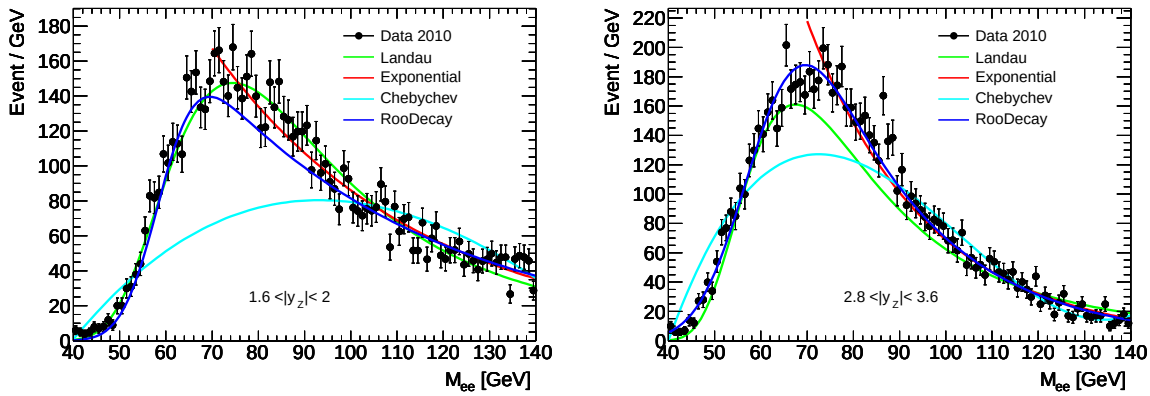

Figure 11.7: Comparison of different fits of the di-electron mass distributions for data in different $|y_Z|$ bins for the CFbg1 background selection. A fraction of the remaining signal in each background selection was simulated by the signal MC with the same selection and subtracted.

the fit uncertainty). The number of background events estimated from fitting of the un-binned sample is in agreement with the sum of background events determined in bins of $|y_Z|$.

The template method with two different templates T1=CCbg2 and T2=CCbg3 was applied as well. This method provides values with larger statistical uncertainty, since the fraction of the background is small. The total number of the QCD background events varies significantly from 100 to 200. Since the Landau function provides a better description of the background shape (see Fig. 11.6), the RooFit method with corresponding function is preferred.

Method	total $N_{\mathrm{QCD}} \pm$ stat
RooFit global, Fit range: 40-140, Bkg: Landau	**163 ± 16**
RooFit global, Fit range: 40-140, Bkg: Exponential	138 ± 13
RooFit global, Fit range: 40-140, Bkg: RooDecay	174 ± 14
RooFit summed, Fit range: 40-140, Bkg: Landau	186 ± 19
RooFit summed, Fit range: 40-140, Bkg: Exponential	122 ± 17
RooFit summed, Fit range: 40-140, Bkg: RooDecay	194 ± 19
Template T1 global, Fit range 60-120, Signal range: 75-100	181 ± 29
Template T1 summed, Fit range 60-120, Signal range: 75-100	179 ± 29
Template T2 global, Fit range 60-120, Signal range: 75-100	189 ± 21
Template T2 summed, Fit range 60-120, Signal range: 75-100	197 ± 27

Table 11.3: Estimated number of the QCD background events for the CC analysis obtained from different fits and different fit ranges. The presented numbers are calculated for the di-electron mass range [66-116] GeV. The number marked in bold is chosen as central value and a conservative systematic uncertainty of 40% is added to cover all measurements.

The final result is $163.0 \pm 16(\mathrm{stat}) \pm 65.2(\mathrm{syst})$ and has systematic uncertainty of 40%, which was chosen to cover all values in Tab. 11.3. The same RooFit method was used to get background in bins. Fig. 11.8 left shows the background in $|y_Z|$ bins obtained by several methods. All results are scaled by the selected value of 163.

$\lvert y_Z \rvert$	$N_{\mathrm{QCD}} \pm \mathrm{stat} \pm \mathrm{syst}$
0.00 - 0.40	$40.7 \pm 6.2 \pm 16.3$
0.40 - 0.80	$44.0 \pm 6.7 \pm 17.6$
0.80 - 1.20	$21.1 \pm 3.2 \pm 8.4$
1.20 - 1.60	$22.7 \pm 3.5 \pm 9.1$
1.60 - 2.00	$20.1 \pm 3.1 \pm 8.1$
2.00 - 2.40	$14.4 \pm 2.2 \pm 5.8$
Global	$163.0 \pm 16.0 \pm 65.2$

Table 11.4: Estimated number of the QCD background events in the di-electron mass window [66-116] GeV for the CC selection in $|y_Z|$ bins.

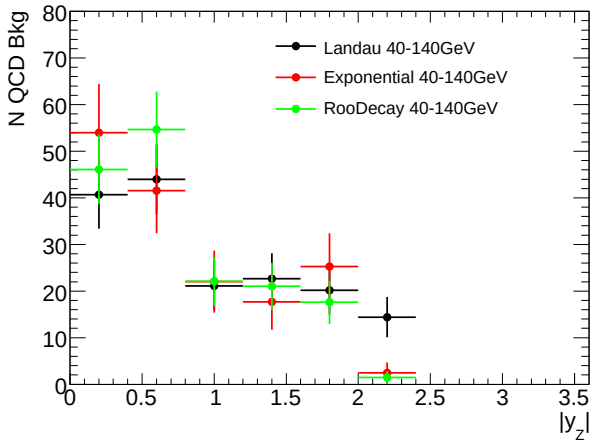

Figure 11.8: Estimated numbers of QCD background events in $|y_Z|$ bins obtained by different methods and scaled by total number of the QCD background events of 163 for the CC selection.

11.4.2 Background for CF $Z \to e^+e^-$ selection

Compared to the CC selection, the CF selection has a larger fraction of background which makes the background estimation more sensitive to the background shape. In this case the RooFit method becomes unstable. The template method with templates T1=CFbg1 and T2=CFbg3 shows more stable results since there is sufficient statistics for the background templates. Tab. 11.5 shows results obtained by several methods. The number of background events estimated from a fit of the un-binned sample is in agreement for the template method with a sum of background events determined in bins of $|y_Z|$, while the RooFit method shows a discrepancy. The T2 template with a narrow signal range was chosen as preferred because this template provides a better defined (signal significantly suppressed) background shape and the di-electron mass range [80-100] GeV contains a larger fraction of signal.

The determined number $334.0 \pm 27(\text{stat}) \pm 65.0(\text{syst})$ of QCD background events has a systematic uncertainty which covers all values presented in Tab. 11.5. Fig. 11.9 left shows the background in $|y_Z|$ bins obtained by different methods and scaled by the selected value of 334. The values obtained by the selected template fit are presented in Tab. 11.6.

11.5 Background in η_e bins

The efficiency calculations described in Sec. 13 are performed in bins of η_e. For these studies, a less strict selection is used for the $Z \to e^+e^-$ events and this leads to increased background.

Method	total $N_{\mathrm{QCD}} \pm$ stat
RooFit global, Fit range: 40-140, Bkg: Landau	282 ± 18
RooFit global, Fit range: 50-140, Bkg: Landau	327 ± 19
RooFit summed, Fit range: 50-140, Bkg: Landau	272 ± 29
Template T1 global, Fit range 60-120, Signal range: 75-100	348 ± 27
Template T1 global, Fit range 60-120, Signal range: 75-105	356 ± 29
Template T1 global, Fit range 60-120, Signal range: 80-100	367 ± 24
Template T1 summed, Fit range 60-120, Signal range: 75-100	399 ± 36
Template T1 summed, Fit range 60-120, Signal range: 75-105	400 ± 34
Template T1 summed, Fit range 60-120, Signal range: 80-100	370 ± 35
Template T2 global, Fit range 60-120, Signal range: 75-100	365 ± 22
Template T2 global, Fit range 60-120, Signal range: 75-105	365 ± 25
Template T2 global, Fit range 60-120, Signal range: 80-100	**334 ± 27**
Template T2 summed, Fit range 60-120, Signal range: 75-100	370 ± 34
Template T2 summed, Fit range 60-120, Signal range: 75-105	373 ± 35
Template T2 summed, Fit range 60-120, Signal range: 80-100	336 ± 32

Table 11.5: Estimated number of QCD background events for the CF analysis are obtained from different fits and different fit ranges. The presented numbers are calculates for the di-electron mass range [66-116] GeV. The number marked in bold is chosen as central value.

11.5.1 CC selection

The background in bins of η_{e2}[1] is calculated for different selections, which are presented in Tab. 11.7. Since for the CC analysis both electrons are equivalent and the selection is asymmetric (different selection criteria for the first and second electrons), each event is used twice. The background level is calculated using the RooFit method with the Landau function which fits the data better. Other functions are used to estimate systematic uncertainties. In order to get a smaller fraction of background, a signal mass window [80-100] GeV was considered, while the fit was calculated for the mass window [40-140] GeV.

The results are presented in Tabs. 11.8, 11.9 and 11.10 together with statistical and systematic uncertainties. The systematic uncertainties were estimated using different fit functions and different mass windows. Only results from good fits with $\chi^2/dof < 2$ were included for the determination of the systematic uncertainties. Fig. 11.10 shows an example of fits of the di-electron mass distributions with different fit functions for the background.

11.5.2 CF selection

In case of the CF, the selection background is calculated for the selections described in Tab. 11.11: The central value is calculated for a mass window [80-100] GeV, while the fit was calculated for

[1] Here $e2$ is an electrons which is labeled as second in the selection. It passes less strict selection conditions compare to the first electron.

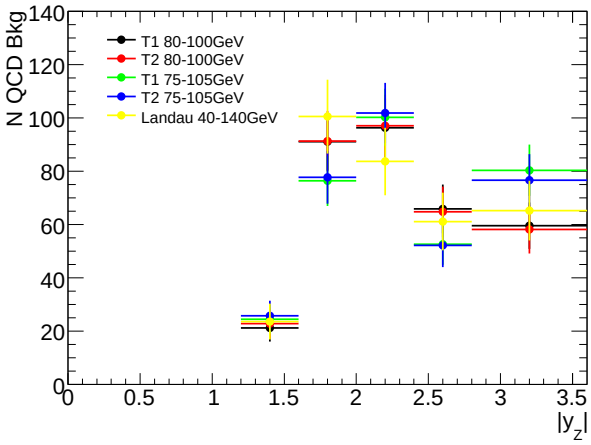

Figure 11.9: Estimated numbers of the QCD background events in $|y_Z|$ bins are obtained by different methods and scaled by total number of the QCD background events of 334 for the CF selection.

$\|y_Z\|$	$N_{\mathrm{QCD}} \pm \mathrm{stat} \pm \mathrm{syst}$
1.20 - 1.60	$22.8 \pm 1.8 \pm 4.4$
1.60 - 2.00	$91.3 \pm 7.4 \pm 17.5$
2.00 - 2.40	$97.0 \pm 7.8 \pm 18.6$
2.40 - 2.80	$64.7 \pm 5.2 \pm 12.4$
2.80 - 3.60	$58.2 \pm 4.7 \pm 11.1$
Total	$334.0 \pm 27.0 \pm 64.0$

Table 11.6: Estimated number of the QCD background events in the di-electron mass window [66-116] GeV for the CF selection in $|y_Z|$ bins.

the window [40-140] GeV using the RooFit method with the Landau background function. The results for both selections are presented in Tabs. 11.13 and 11.12. The systematic uncertainties were calculated using the RooFit method with different background functions and different fit ranges and using the template method as well. The RooFit method is not stable in case of the CF selection. Therefore only results from good fits with $\chi^2/dof < 2$ were included for the determination of the systematic uncertainties. Additionally, some criteria for an estimated background shape were used: the background in the side bands (mass range [60-80] GeV and [100-120] GeV) should be larger than the background in the central band (mass range [80-100] GeV), and the background in the right side band (mass range [100-120] GeV) should be 2 times smaller than sum of backgrounds in the left side band and the background in the central band (mass range [60-100] GeV). This selection is based on the background shape studies and provides an effective selection for rejecting bad fits.

Fig. 11.11 and 11.12 show several examples for the template and RooFit methods respectively. The RooFit is performed for several different background functions, the fit for each of

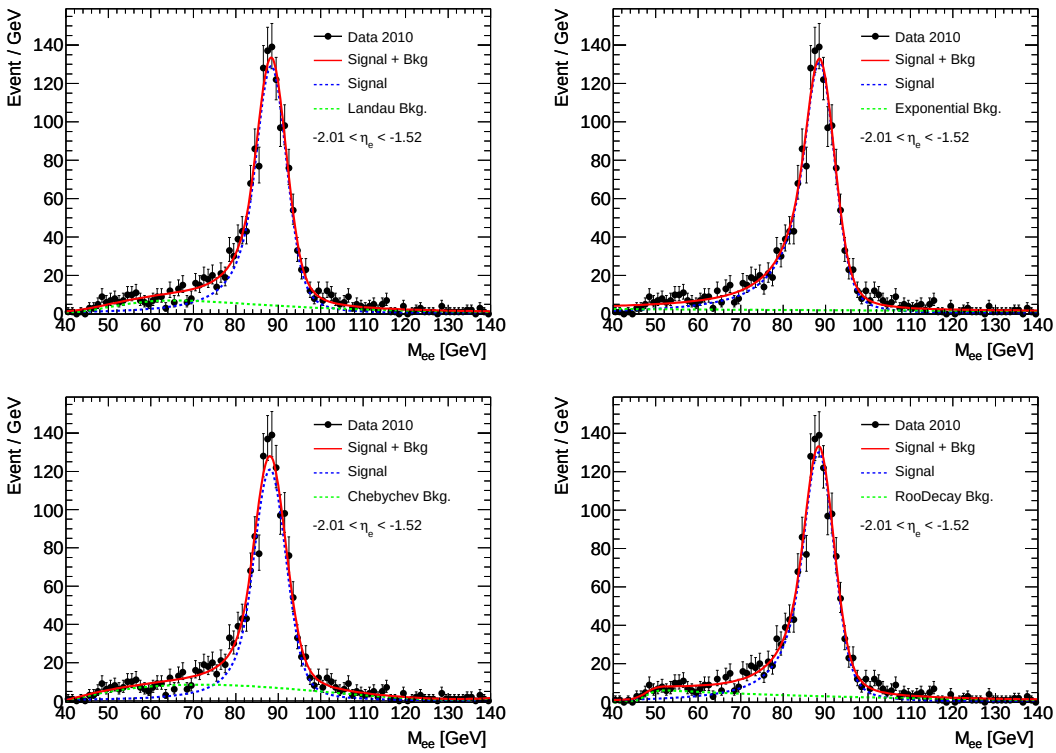

Figure 11.10: An example of the di-electron mass distributions with different background functions for fits for the CC_noID selection in $-2.01 < \eta_{e2} < -1.52$ bin.

name	e_1^{ID}	e_1^{Iso}	min. $p_{T,e1}$	e_2^{ID}
CC_noID	ID "tight"	"CaloIso98"	25	-
CC_medium	ID "tight"	"CaloIso98"	25	ID "medium"
CC_tight	ID "tight"	"CaloIso98"	25	ID "tight"

Table 11.7: Several selections for efficiency calculations, which are based on the CC selection.

η_e bins	$bg \pm \mathrm{stat} \pm \mathrm{syst}$	$bg \pm \mathrm{stat} \pm \mathrm{syst}$ in %
-2.47 - -2.01	$3.22 \pm 1.79 \pm 1.89$	$0.56 \pm 0.31 \pm 0.33$
-2.01 - -1.52	$3.12 \pm 1.77 \pm 1.97$	$0.36 \pm 0.21 \pm 0.23$
-1.37 - -0.80	$14.65 \pm 3.83 \pm 2.39$	$0.91 \pm 0.24 \pm 0.15$
-0.80 - 0.00	$2.31 \pm 1.52 \pm 2.23$	$0.09 \pm 0.06 \pm 0.08$
0.00 - 0.80	$16.66 \pm 4.08 \pm 10.35$	$0.57 \pm 0.14 \pm 0.35$
0.80 - 1.37	$11.47 \pm 3.39 \pm 1.16$	$0.64 \pm 0.19 \pm 0.06$
1.52 - 2.01	$4.77 \pm 2.18 \pm 3.39$	$0.53 \pm 0.24 \pm 0.38$
2.01 - 2.47	$0.27 \pm 0.52 \pm 0.19$	$0.05 \pm 0.09 \pm 0.04$

Table 11.8: Estimated numbers of the background events in the di-electron mass window [80-100] GeV for the CC_tight selection in η_{e2} bins. Statistical uncertainties are taken from the fit, while systematic uncertainties are estimated using fits with different background factions and with different fit mass ranges.

them is calculated for a mass range [40-140] GeV. The template method uses background selection CFbg3 for the background template. Signal is fitted under the peak region [75-100] GeV, while background is fitted in side bands [66-75] GeV and [100-116] GeV. The different panels in Fig. 11.12 correspond to the CF_noID (top panels) and CF_loose(bottom panels) background selections for the first (left panels) and second (right panels) bins.

11.6 Summary

The presented studies show that background is dominated by the QCD contribution ($\sim 75\%$ for the CC and $\sim 85\%$ for the CF analysis), however the EW background contributions also must be taken into account. The total background-to-signal ratio is 2.1% for the CC analysis and 12.5% for the CF analysis. Additional requirements, which could be introduced to decrease the CF background would significantly increase statistical uncertainties of the cross-section measurement, which are already large.

η_e bins	$bg \pm \text{stat} \pm \text{syst}$	$bg \pm \text{stat} \pm \text{syst}$ in %
-2.47 - -2.01	$0.38 \pm 0.61 \pm 2.08$	$0.05 \pm 0.08 \pm 0.36$
-2.01 - -1.52	$2.32 \pm 1.52 \pm 1.26$	$0.22 \pm 0.14 \pm 0.15$
-1.37 - -0.80	$17.67 \pm 4.20 \pm 1.66$	$0.94 \pm 0.22 \pm 0.10$
-0.80 - 0.00	$0.27 \pm 0.52 \pm 4.42$	$0.01 \pm 0.02 \pm 0.17$
0.00 - 0.80	$14.32 \pm 3.78 \pm 1.95$	$0.43 \pm 0.11 \pm 0.07$
0.80 - 1.37	$15.51 \pm 3.94 \pm 1.58$	$0.74 \pm 0.19 \pm 0.09$
1.52 - 2.01	$1.47 \pm 1.21 \pm 1.05$	$0.13 \pm 0.11 \pm 0.12$
2.01 - 2.47	$4.33 \pm 2.08 \pm 1.14$	$0.63 \pm 0.30 \pm 0.21$

Table 11.9: Estimated numbers of the background events in the di-electron mass window [80-100] GeV for the CC_medium selection in η_{e2} bins. Statistical uncertainties are taken from the fit, while systematic uncertainties are estimated using fits with different background factions and with different fit mass ranges.

η_e bins	$bg \pm \text{stat} \pm \text{syst}$	$bg \pm \text{stat} \pm \text{syst}$ in %
-2.47 - -2.01	$71.79 \pm 8.47 \pm 4.98$	$8.29 \pm 0.98 \pm 0.48$
-2.01 - -1.52	$108.71 \pm 10.43 \pm 34.21$	$8.81 \pm 0.84 \pm 2.31$
-1.37 - -0.80	$149.13 \pm 12.21 \pm 59.35$	$7.22 \pm 0.59 \pm 2.39$
-0.80 - 0.00	$229.35 \pm 15.14 \pm 9.81$	$7.02 \pm 0.46 \pm 0.25$
0.00 - 0.80	$242.62 \pm 15.58 \pm 74.82$	$6.69 \pm 0.43 \pm 1.72$
0.80 - 1.37	$159.44 \pm 12.63 \pm 44.31$	$7.05 \pm 0.56 \pm 1.63$
1.52 - 2.01	$77.20 \pm 8.79 \pm 20.07$	$6.35 \pm 0.72 \pm 1.38$
2.01 - 2.47	$70.83 \pm 8.42 \pm 26.05$	$9.18 \pm 1.09 \pm 2.81$

Table 11.10: Estimated numbers of the background events in the di-electron mass window [80-100] GeV for the CC_noID selection in η_{e2} bins. Statistical uncertainties are taken from the fit, while systematic uncertainties are estimated using fits with different background factions and with different fit mass range.

name	e^{ID}_{central}	$e^{\text{Iso}}_{\text{central}}$	min. $p_{T,e_{\text{central}}}$	e^{ID}_{forward}
CF_noID	ID "tight"	"CaloIso98"	25	-
CF_loose	ID "tight"	"CaloIso98"	25	ID "forward loose"

Table 11.11: Several selections for efficiency calculations, which are based on the CF selection.

$\|\eta_e\|$ bins	$bg \pm \text{stat} \pm \text{syst}$	$bg \pm \text{stat} \pm \text{syst}$ in %
2.50 - 3.20	$275.56 \pm 16.60 \pm 99.28$	$14.43 \pm 0.87 \pm 5.20$
3.20 - 4.90	$172.59 \pm 13.14 \pm 28.91$	$22.69 \pm 1.73 \pm 3.80$

Table 11.12: Estimated numbers of the background events in the di-electron mass window [80-100] GeV for the CC_noID selection in $\eta_{e_{\text{forward}}}$ bins. Statistical uncertainties are taken from the fit, while systematic uncertainties are estimated using fits with different background factions and with different fit mass range.

$\|\eta_e\|$ bins	$bg \pm \text{stat} \pm \text{syst}$	$bg \pm \text{stat} \pm \text{syst}$ in %
2.50 - 3.20	$65.10 \pm 8.07 \pm 40.94$	$4.13 \pm 0.26 \pm 2.60$
3.20 - 4.90	$21.70 \pm 4.66 \pm 11.89$	$3.47 \pm 0.37 \pm 1.90$

Table 11.13: Estimated numbers of the background events in the di-electron mass window [80-100] GeV for the CC_loose selection in $\eta_{e_{\text{forward}}}$ bins. Statistical uncertainties are taken from the fit, while systematic uncertainties are estimated using fits with different background factions and with different fit mass range.

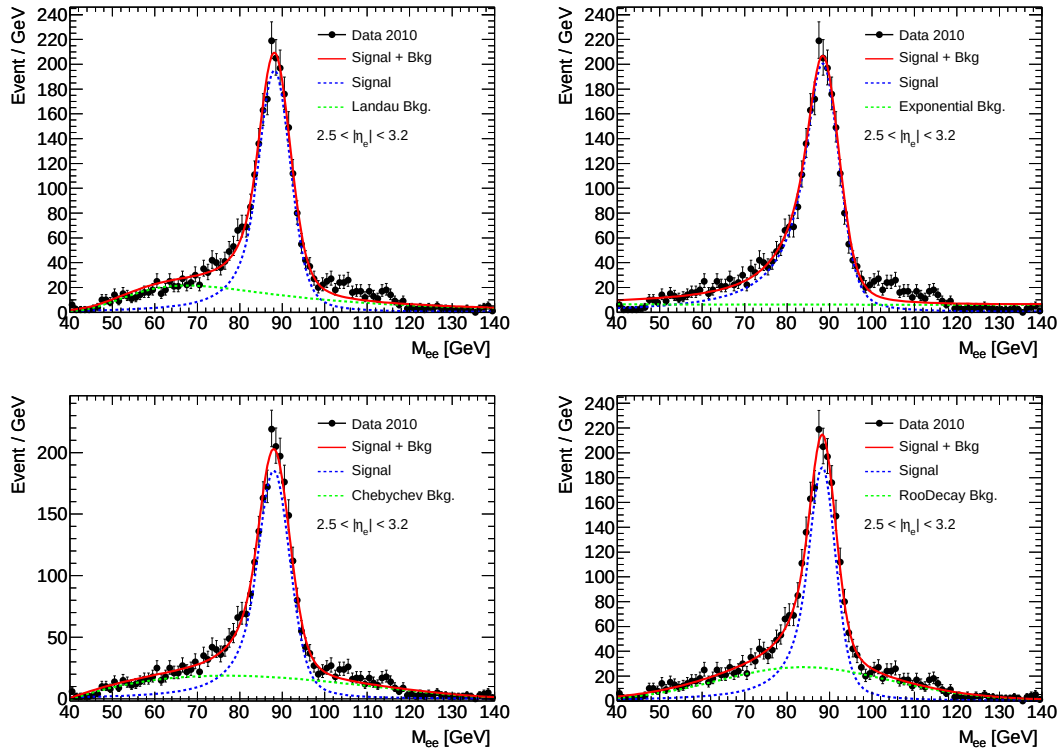

Figure 11.11: An example of the di-electron mass distributions with different fit options and different tightness of the central electron for the CF based selection (CF_loose) for $2.5 < |\eta_{e_{\text{forward}}}| < 3.2$ bin.

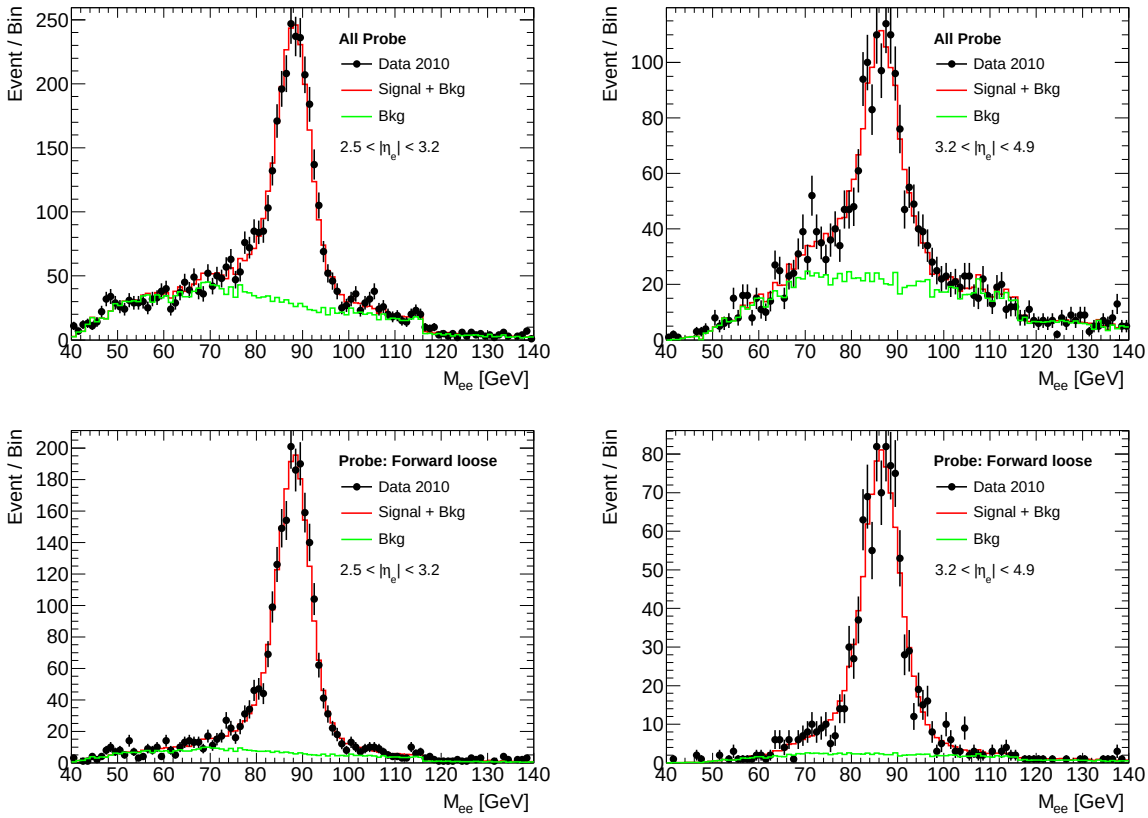

Figure 11.12: An example of the di-electron mass distributions with template fit for the CF based selection. Background shape is taken from data event with CFbg3 background selection. Background distributions are different for the EMEC-IW and FCAL. Signal shape is taken from signal MC. Signal is fitted under the mass peak [75-100] GeV, while background is fitted in the side bands [66-75] GeV and [100-116] GeV. Top panels correspond to the CC_noID selection while bottom to the CF_loose.

CHAPTER 12

Calibration of the EM calorimeter

The precise determination of the electron and photon energy scale and resolution is important for measurements in the electron channel. For example, the calibration is important for investigations of $Z \to e^+e^-$ events (especially the measurement of $Z\, p_{T,Z}$), and for searches for $Z' \to ee$ and $H \to \gamma\gamma$.

The EM calorimeter consists mostly of absorber material and therefore reconstructs only a small fraction of a particles energy. A calibration is necessary in order to precisely reconstruct the full energy. The calibration of the electron and photon energy measurements is performed in three steps [2]:

- The LAr calorimeter electronic calibration converts an electronic signal, which comes as a response from the detector cells, into a corresponding deposited energy.
- MC-based calibration applies corrections at the cluster level for energy losses due to the dead material and leakage.
- The in-situ calibration uses information from the physics events recorded by the ATLAS detector in order to determine the absolute energy scale and to cross-calibrate different regions of the EM calorimeter.

The calibration presented here is based on a comparison of the reconstructed di-electron mass with the well known mass of the Z boson, for data and MC. The calibration method is presented in Sec. 12.1. Different techniques were used to estimate systematic uncertainties of the calibration as described in Sec. 12.4. The effect of the resolution is also shown in this chapter.

12.1 Method description

Fully reconstructed $Z \to e^+e^-$ decays together with the well measured (at LEP) Z boson mass and width provide a natural reference for the electron energy calibration. The advantage of the method is that it is based on the signal events for the $Z \to e^+e^-$ analysis and the electron

kinematics are similar to those from the $W \to e\nu$ analysis, which provide smaller systematical uncertainties.

Neglecting the electron mass, the invariant mass of the di-electron can be written as:

$$M_{ee} = \sqrt{2E_1E_2(1-\cos(\theta_{12}))}, \tag{12.1}$$

where E_1, E_2 are the energies of the electrons, and θ_{12} is the opening angle between them. The calibration procedure consists in finding the calibration coefficients $\Delta_j = \Delta(p_{T,j}, \eta_j, \phi_j, ...) \equiv \Delta(j)$ (j is the bin number), which correct the electron energies and which are determined by equation: $E' = E(1+\Delta(j))$, where E' is the corrected energy. Assuming that these coefficients are small, the invariant mass for the calibrated electrons can be approximated as:

$$M'_{ee} = M_{ee}(1+0.5[\Delta_1+\Delta_2]), \tag{12.2}$$

where Δ_1 and Δ_2 are the calibration coefficients for the electrons [1]. This corrected di-electron mass is compared to a reference mass M_{ref} defined later. In general, the approximation requires 2–3 iterations for the determination of the calibration factors. The calibration factors for the iteration $n+1$ are calculated as

$$\alpha_j^{n+1} = \alpha_j^n - \frac{\Delta_j}{1+\Delta_j}. \tag{12.3}$$

The calibration correction factors for the first iteration are set to $\alpha_j^1 = 0$.

The calibration method is based on an iterative χ^2 minimization, in which the following linearized χ^2 is used:

$$\chi^2(\Delta_j) = \sum_{i=1}^{N_{\text{evt}}} \left(\frac{M_{ee}^i - M_{\text{ref}}(j_{e^1}^i, j_{e^2}^i)(1-0.5[\Delta_{j_{e^1}^i} + \Delta_{j_{e^2}^i}])}{\sigma_{M_{ee}}} \right)^2. \tag{12.4}$$

Here N_{evt} is total number of selected $Z \to e^+e^-$ events. For $Z \to e^+e^-$ event i, the bins $j_{e^1}^i$ and $j_{e^2}^i$ corresponding to the reconstructed electrons are determined (both electron and positron are equivalent for the calibration procedure). The invariant mass M_{ee} is reconstructed using the calibration factor from the previous iteration after correcting the four-momenta of the decay leptons. The reference mass M_{ref} depends on the PDG value[2] of the Z boson mass as well as on $j_{e^1}^i$ and $j_{e^2}^i$. $\sigma_{M_{ee}}$ is the di-electron mass resolution. It is taken as a constant factor for each iteration.

Minimization of Eq. 12.4 with respect to Δ_j leads to a system of linear equations from which the Δ_j are determined:

$$\Delta_j = M_{ij}^{-1} V_i, \tag{12.5}$$

[1] The calibration correction factors $\alpha_j \equiv \alpha(j)$ are defined as: $E'(1+\alpha(j)) = E$ in order to be consistent with the official ATLAS definition.

[2] The Particle Data Group (PDG) is an international collaboration of particle physicists that compiles and reanalyzes published results related to the properties of particles and fundamental interactions.

where M_{ij} is a covariance matrix and V_i is a vector of shifts. Both are calculated by the following equations:

$$M_{ij} = \frac{0.5\,(n_{ij} + n_{ji} + n_{ii} + n_{jj})}{\sigma^2}$$
$$V_j = \frac{1}{\sigma^2} \sum_{i=1}^{N_{\text{evt}}} \left(\sum_{j^i_{e^1}} \left[\frac{M_{\text{ref}}(j^i_{e^1}, j^i_{e^2}) - M^i_{ee}}{M_{\text{ref}}(j^i_{e^1}, j^i_{e^2})} \right] + \sum_{j^i_{e^2}} \left[\frac{M_{\text{ref}}(j^i_{e^1}, j^i_{e^2}) - M^i_{ee}}{M_{\text{ref}}(j^i_{e^1}, j^i_{e^2})} \right] \right) \tag{12.6}$$

where n_{ij} is the number of events where the first electron falls in bin i and the second electron falls in bin j.

The vector of shifts contains the sum of shifts between reference mass and measured invariant mass of the di-electron, normalized by the reference mass. The energies of the electrons are already corrected by the calibration factors, calculated at the previous iteration.

Since there are two separate Z boson analyses (CC and CF, see Sec. 9.2), the calibration procedure can be done separately for the central region or combined for the central and forward. For the simultaneous calibration in the central and forward regions, events are selected by separate analysis chains, but the resulting covariance matrices are added together before inversion and determination of the calibration coefficients. The summation of the covariance matrices for the combined CC and CF calibration is performed for each iteration. An example of covariance matrices for the CC and CF selections is presented in Fig. 12.1 together with the vectors of shifts. The calibration here is performed in 12 $|\eta_e|$ bins and uses 34.5 k and 7.9 k di-electrons for the CC and CF analyses, respectively.

The covariance matrix and vector of shifts for the CC selection are filled only for $|\eta_e| < 2.5$, while in case of the CF selection they are filled for the full η_e range. Therefore the calibration based on the CF events calibrates both the central and the forward region. The di-electron mass resolution $\sigma_{M_{ee}}$ is not included into Eq. 12.5 and Eq. 12.6 because it is taken as a constant factor. However the resolutions for the CC and CF analyses are different, that needs to be take into account for the summation of the covariant matrices. The resolution for the CF analysis is worse and therefore the covariance matrix for the CF analysis should have smaller significance for the combined calibration.

The reference mass $M_{\text{ref}}(j_1, j_2)$ is determined from the MC simulation as the average reconstructed di-electron mass M_{ee} for events in which the first electron falls in bin j_1 and the second electron falls in bin j_2. The mass is lower for events in which both lepton are reconstructed at low $p_{T,e}$. This is illustrated in Fig. 12.3, which shows M_{ee} distribution for all events and events in which both leptons falls in low(high) $p_{T,e}$ bin.

Fig. 12.2 shows (as an example) $M_{\text{ref}}(j_1, j_2)$ for binning in η_e (left) and $p_{T,e}$ (right) for the combined CC and CF calibration. The distribution of M_{ref} is symmetric in j_1 and j_2. The reference mass shows stronger variation for $p_{T,e}$ compared to η_e binning.

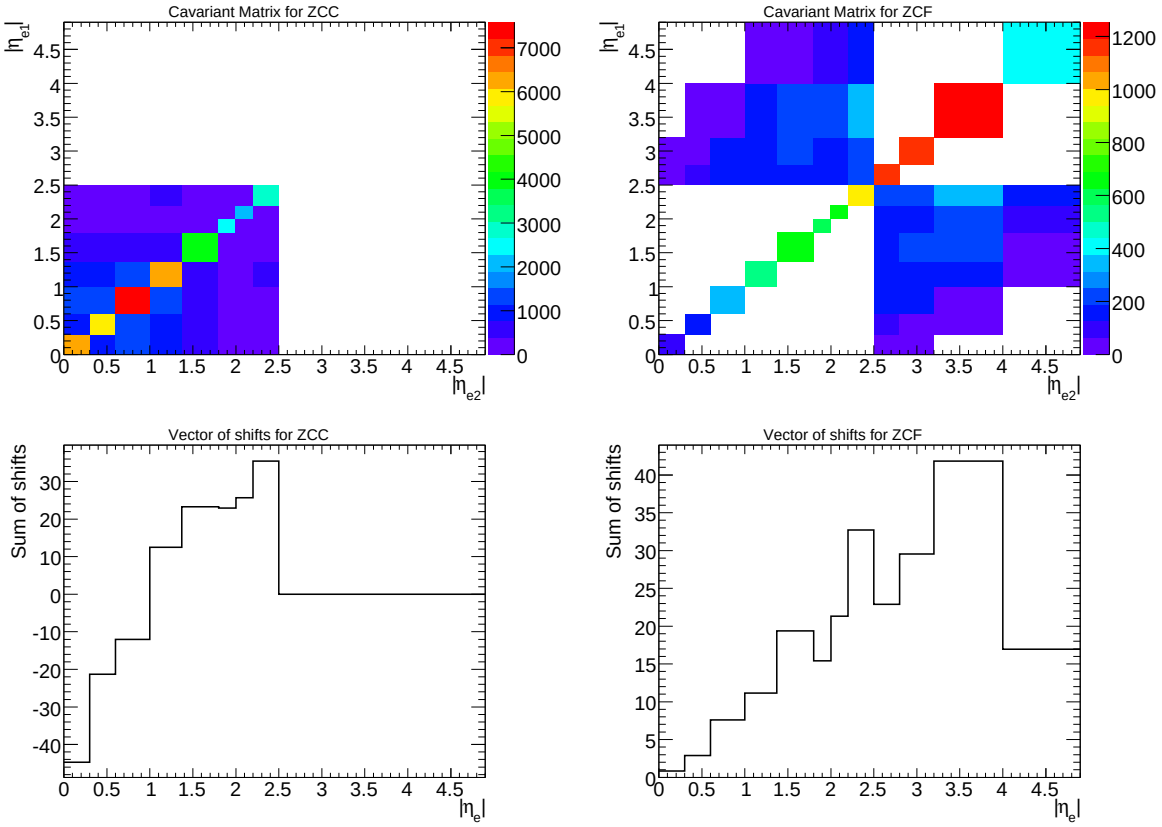

Figure 12.1: The covariant matrices (top) and vector of shifts (bottom) for the CC (left) and CF (right) selections.

12.1.1 Test of the calibration method

Before performing the data calibration, the calibration method must be validated. The validation is based on a so-called closure test. An MC sample is used as a reference for the calibration and as a sample which needs to be calibrated, referred in the later text as "pseudo-data". The calibration method starts from a random correction with $\alpha_i \neq 0$. Several iterations lead to a correction factor $\alpha_i \sim 0$ (see Fig. 12.4) within statistical uncertainties. This test shows that at least 2–3 iterations are needed to converge.

The next test of the calibration consists of using the same sample for the reference, but modified "pseudo-data". The energy of the electrons in this sample is shifted to

$$E' = E(1 + \gamma_\eta \eta_e), \tag{12.7}$$

where $\gamma_\eta = 0.01$ and E is the initial electron energy. This energy shift leads to a shift of the invariant mass (see Fig. 12.5 left) of about 1%.

In this test, the calorimeter mis-calibration depends on η_e, therefore η_e bins are more natural bins to use for the calibration. 12 η_e bins were chosen in order to calibrate the sample with shifted energy. Several iterations of the calibration move the mass peak back (see Fig. 12.5 right). The correction factors for this test are shown in Fig. 12.6. Generally they reproduce the

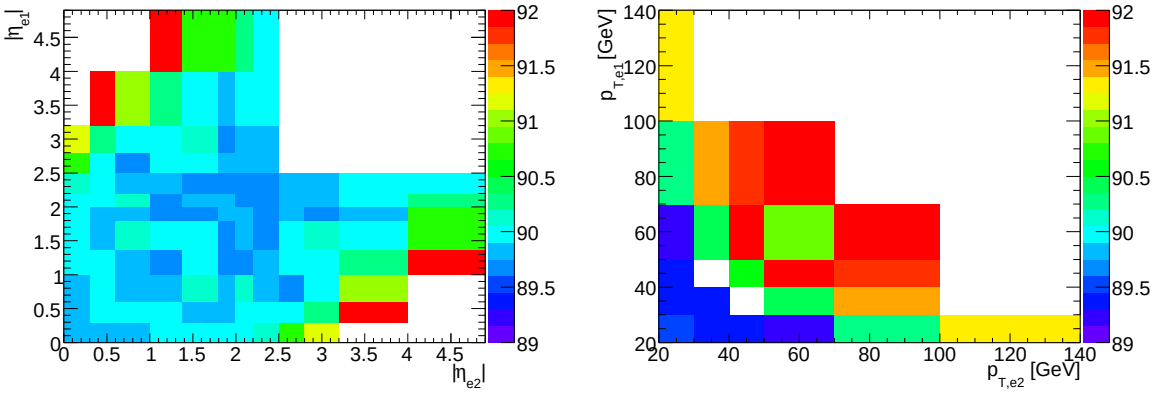

Figure 12.2: Tables of reference masses for 12 $|\eta_e|$ bins (left) and 7 $p_{T,e}$ bins (right). Vertical and horizontal axes correspond to electron one and electron two respectively. Since both electrons are equivalent for the calibration, the tables are always symmetric. These tables illustrate the di-electron mass dependence on the electrons kinematics.

test bias from Eq. 12.7. Some small deviations appear in the crack region $1.37 < |\eta_e| < 1.52$.

12.1.2 Studies of statistical uncertainties

The statistical uncertainties of the calibration factors are calculated from the covariance matrix obtained during the calibration. The other way to calculate statistical uncertainties is by using the toy MC method. For this method, the calibration is performed N times (e.g. $N = 120$) using every time the same reference sample but statistically different "pseudo-data" samples. Finally, the uncertainty can be estimated as an standard deviation of the correction factors. Fast inline generator (see Sec 10.2) with 100 K event statistics was used to create each of the 120 "pseudo-data" sample.

Correction factors for these N samples and average calibration factors with uncertainties are shown in Fig. 12.7 left. Fig. 12.7 right shows a comparison of the statistical uncertainty estimated by the covariant matrix, and calculated by the MC method. Good agreement between the two histograms validates the estimation of the uncertainties.

12.2 Resolution dependencies

The width and mean of the observed di-electron mass distribution depend on the mass resolution. A study of this effect can be made by a smearing of the electron energy. For simplicity, a Gaussian smearing with the standard deviation σ_E is considered here. Since the resolution depends on η_e, the smearing parameter is chosen as $\sigma_E = \gamma_\eta \eta_e$, where $\gamma_\eta = 0.03$.

The effect of the energy smearing is clearly visible in Fig. 12.8, where the invariant mass distributions before and after smearing of the electron energy are shown. The resulting effect on the calibration can be estimated by comparing M_{ref} determined for the nominal and smeared MC sample. This comparison is shown in Fig. 12.9 in η_e and $p_{T,e}$ binnings. From this figure

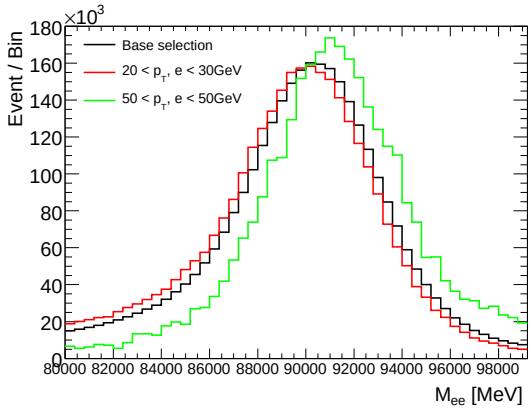

Figure 12.3: Comparison of the di-electron mass distributions for the combined CC and CF selection for the MC sample. Black histogram shows all selected events, red histogram corresponds to events with both electrons in $20 < p_{T,e} < 30$ GeV bin, green histogram shows events with both electrons in $50 < p_{T,e} < 70$ GeV bin. All histograms are normalized to the number of events in the CC and CF selections together.

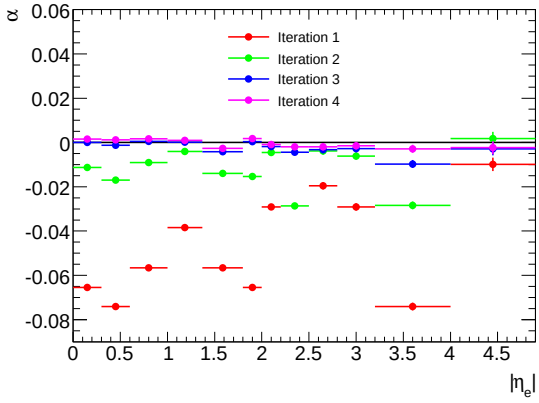

Figure 12.4: Closure test of the calibration. 3 iterations are needed in order to get correction factors α close to 0 within statistical uncertainties.

it becomes clear that energy smearing effects more stronger impacts of a calibration binned in $p_{T,e}$. Therefore the resolution of a MC sample needs to be corrected to data resolution before performing the calibration.

12.2.1 MC resolution correction

The standard deviations of the di-electron mass distributions for the data and signal MC are different due to the different electron energy resolution of the data and MC and due to background in the data sample. In order to separate the resolution effect from the effect of the background the fitting procedure described in Sec. 11 was performed. The mass resolution is estimated as a sigma of the Crystal-Ball function (see Tab. 12.1 and Fig. 12.10). The smearing factors, which are applied to energy of the electron in MC, are used to minimize the differences

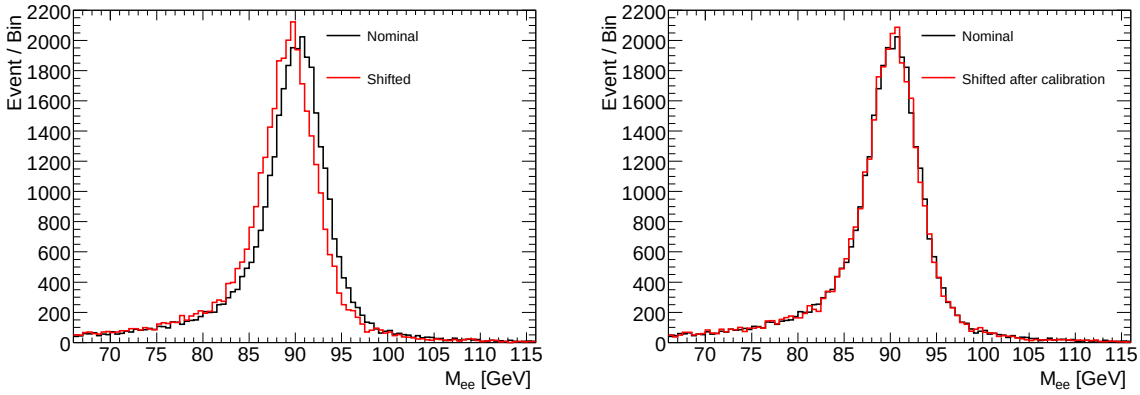

Figure 12.5: Comparison of di-electron mass distribution between nominal sample and sample with electron energy shift: $E' = E(1 + \gamma_\eta \eta_e)$, where $\gamma_\eta = 0.01$ before (left) and after (right) the calibration.

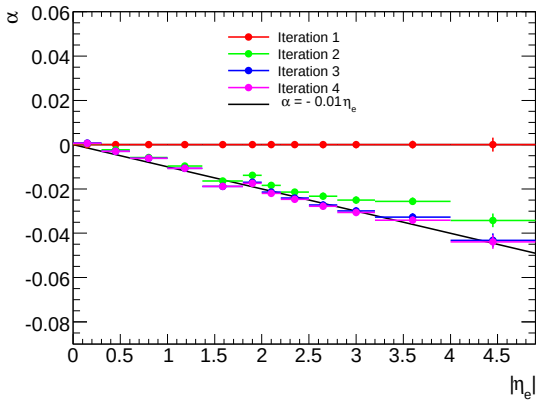

Figure 12.6: Correction factors for the calibration test. Energy of the electrons in "pseudo-data" was shifted as $E' = E(1+\gamma_\eta \eta_e)$, where $\gamma_\eta = 0.01$ compare to reference sample. Presented correction factors α eliminate energy shift. Black line shows the truth calibration $\alpha = -0.01\eta_e$.

in the invariant mass resolution between the data and MC. They were determined in 4 η_e bins (two in the central and two in the forward) with respect of the detector geometry and given in Tab. 12.2.

	EMB-EMB	EMEC-OW - EMEC-OW	Center - EMEC-IW	Center-FCAL
Data	1.65 ± 0.1	2.09 ± 0.3	2.98 ± 0.2	3.67 ± 0.35
MC before smearing	1.5 ± 0.01	1.76 ± 0.03	2.12 ± 0.02	3.5 ± 0.03
MC after smearing	1.59 ± 0.01	2.12 ± 0.03	2.95 ± 0.02	3.69 ± 0.03

Table 12.1: Invariant mass resolution for different regions of the calorimeter for data and MC (before and after smearing). The resolution is obtained from Crystal Ball sigma parameter.

Comparisons of the di-electron mass distribution between the data and MC before and after smearing are shown in Fig. 12.11. In order to better illustrate differences, the plots are made

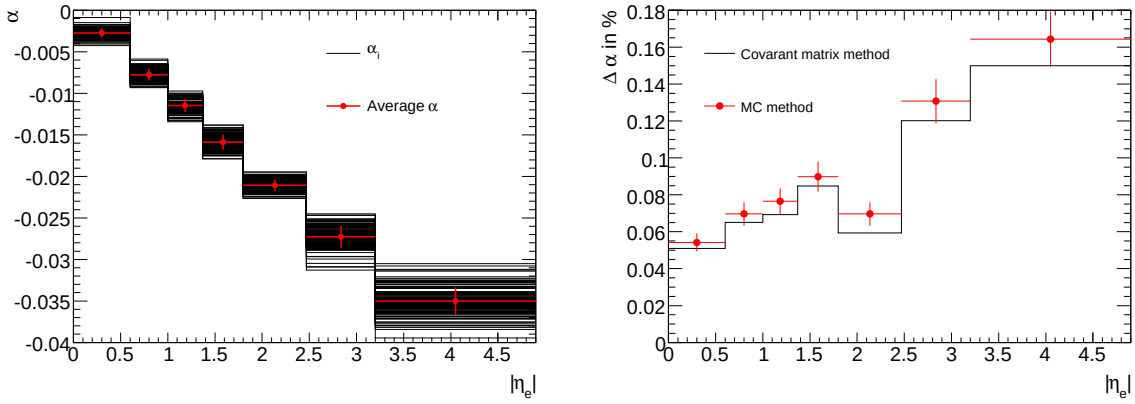

Figure 12.7: Left: Correction factors α_i for $N = 120$ "pseudo-data" (black) and average correction factors with uncertainty equal standard deviation (red). Right: Calibration uncertainty was calculated by MC method (red) and estimated by covariant matrix (black). Both methods for estimation of statistical uncertainties are in a good agreement.

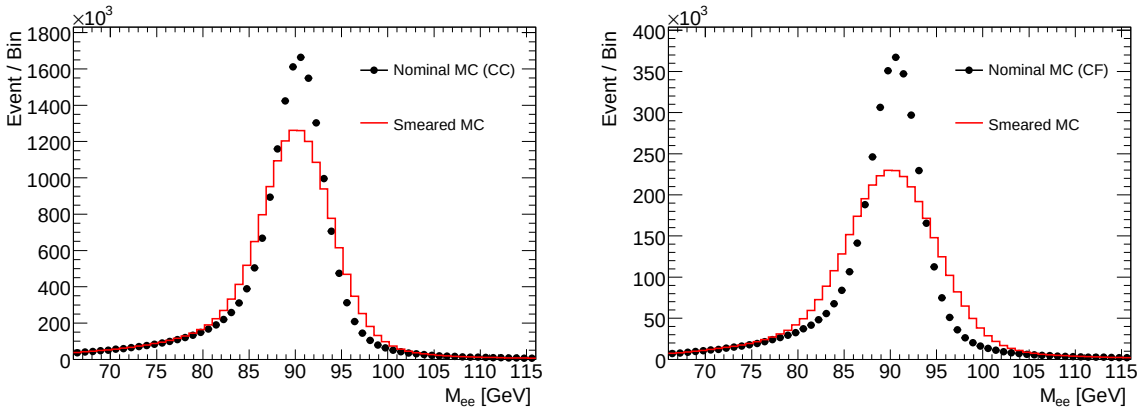

Figure 12.8: Effect of the electron energy smearing ($\sigma_E = \gamma_\eta \eta_e$, where $\gamma_\eta = 0.03$) for the di-electron mass distribution of the MC for the CC (left) and CF (right) selections. Large searing factor was chosen in order to clearly illustrate calibration smearing dependence.

$\|\eta_e\|$ bin	0.0-1.37	1.52-2.5	2.5-3.2	3.2-4.9
Smearing factor	0.0085	0.0016	0.04	0.0185

Table 12.2: Smearing factors which need to be applied for MC on order to get the same resolution with data.

using the data after the calibration.

12.3 Results of calibration using $Z \to e^+e^-$ events

The calibration is based on 2010 data (36.2 pb^{-1}) with 8699 events for the CC selection and 2807 events for the CF selection. A narrow mass window [80-100] GeV, compared to the

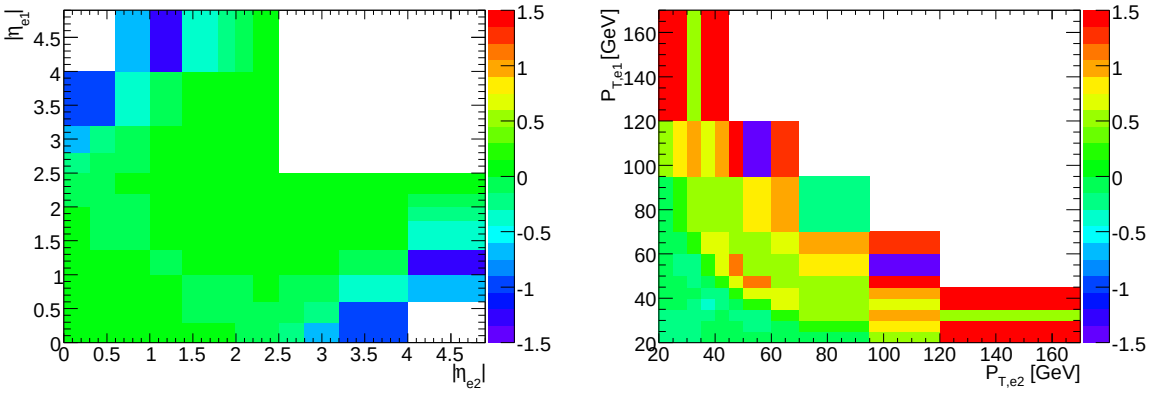

Figure 12.9: Differences in invariant masses of di-electrons between smeared and unsmeared samples are presented in η_e (left) and $p_{T,e}$ (right) bins. The differences in $p_{T,e}$ bins are much larger and therefore measurements in $p_{T,e}$ bins more sensitive to the resolution than in η bins.

baseline selection [66-116] GeV (see Sec. 9.2) is used in order to get a smaller background fraction. The calibration is performed in 56 η_e (4 in the forward and 52 in the central region) bins and covers $|\eta_e| < 4.9$. The size of these bins was chosen as a compromise between statistics and number of bins.

The improvement in the shape of the di-electron mass distribution is shown in Fig. 12.12 where a comparison of data and MC before (left) and after (right) the calibration is shown. Remaining fraction of background was not taken into account for the calibration procedure but systematic uncertainties due to this background was estimated and discussed in following section.

As a result of the calibration the mean of the di-electron mass distribution was significantly shifted: for the CC selection from 88.63 GeV to 89.04 GeV (89.17 GeV for MC), while the resolution remained mostly the same. The mean of the data distribution remains lower compared to MC due to the background.

Several iterations were done in order to get stable correction factors. The difference in correction factors between the first and second iteration depends on the value of the correction factor and could be larger than the statistical uncertainty. Fig. 12.13 shows the correction factors for all iterations and compares them with the official ATLAS correction factors, which were used for 2010 data. The differences are within the statistical uncertainty. Both calibrations are based on the same data samples however the calibration methods are different [2].

12.4 Systematic uncertainties of calibration

Since the calibration procedure depends on both data and MC samples, there are many sources of systematic uncertainties. They are presented below.

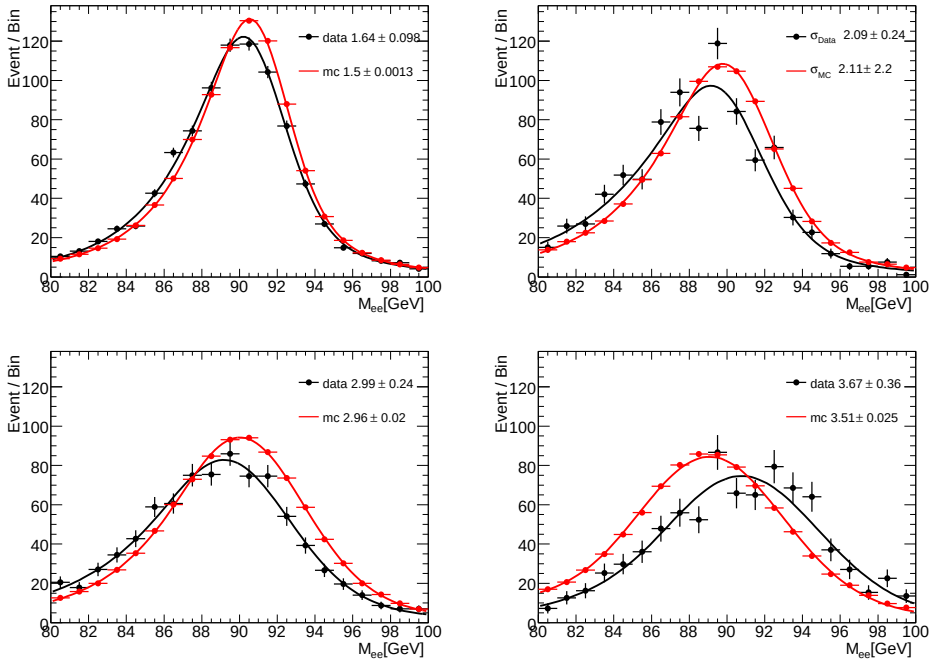

Figure 12.10: Comparison of the di-electron mass distribution between data and MC, fitted by the convolution Crystal-Ball and Breit-Wigner functions. Sigma of the Cristal-Ball function corresponds to the mass resolution (shown on the plot). Calculations were performed in EMB–EMB (left-Top), EMEC-OW–EMEC-OW (right top), Central–EMEC-IW (left-Bottom) and Central–FCAL (right-bottom) bins of the Z boson electrons.

12.4.1 MC statistical uncertainty

The MC sample provides a reference di-electron masses with limited statistics. The effect of the statistics as well as binning effects can be estimated by the following test. The MC sample was split in two. The first sample was used for a reference, the second as a "pseudo-data". Non-zero calibration factors determined in this procedure measure the statistical uncertainty for the reference sample. They are found to be below 0.1%.

12.4.2 Theoretical inputs

Main parameters of the di-electron mass shape are modified by the final state radiation and proton structure functions. The uncertainties related to this effect can be calculated using different MC samples. Since for the central value of the calibration MC@NLO was used, Pythia MC, which used different PDFs and a different algorithm for radiation can be used for this test. It has been shown that the uncertainty is less than 0.1%.

12.4.3 Background

The background under the mass peak is significantly suppressed by ID and Iso cuts. The fraction of the remaining background is about 1% and 5% for the CC and CF selections,

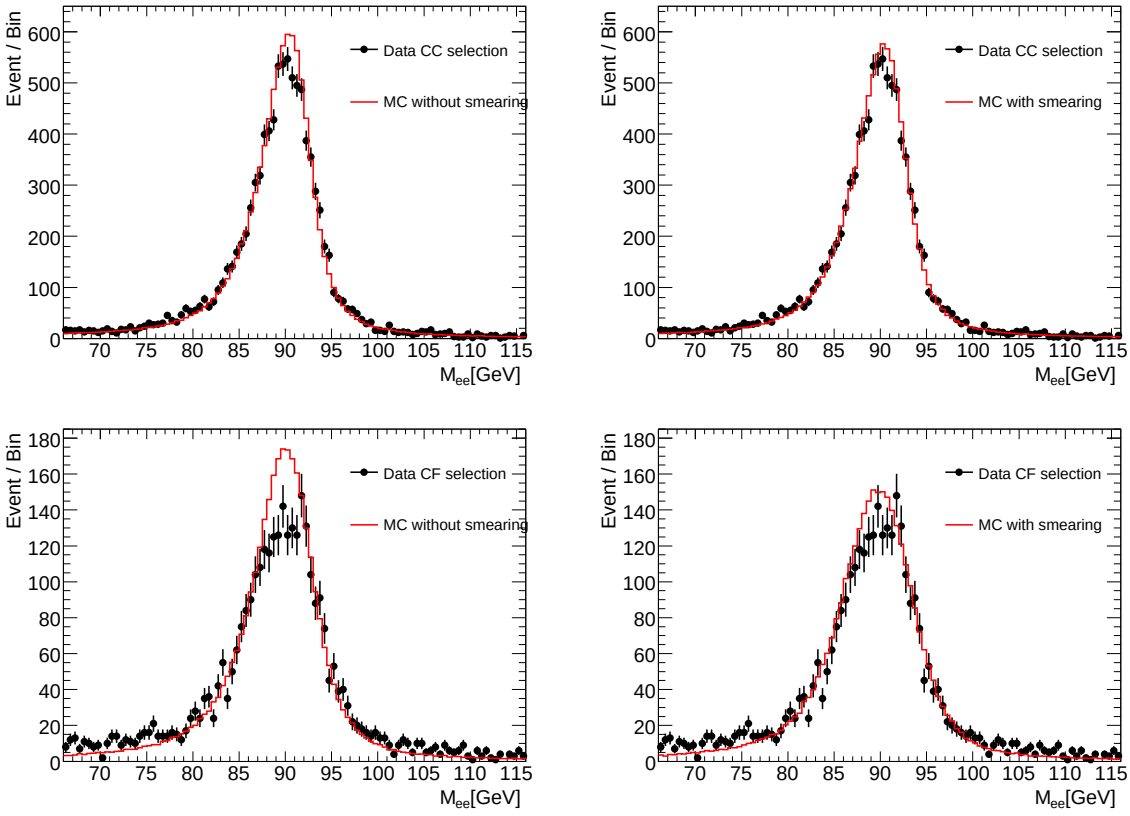

Figure 12.11: Comparisons of the di-electron mass distribution between calibrated data and MC before smearing (left) after smearing (right) for the CC (top) and CF (bottom) selections.

respectively (see Sec. 11).

For studies of the remaining background effect, calibration was performed for different mass ranges: [80-100] GeV, [75-105] GeV and [85-95] GeV. This test gives about 0.2% uncertainty for the EMB, 0.6% for the EMEC-OW, 0.8% for the EMEC-IW and up to 1.2% for the FCAL.

Another approach to estimate the background effects is using different selections. For example, tightening the ID cut from ID "medium" to ID "tight" for the electrons in the CC selection reduces background significantly. Relaxing Iso cut for the CF selection increases background. Calibration factors determined for these modified ID cuts are within 0.2% for the EMB and with 0.3% and 1.1% for the EMEC and the FCAL respectively, which is covered by the background systematic uncertainties.

12.4.4 Additional material

MC simulation requires a detailed information about the detector structure. Imperfect knowledge of the detector geometry leads to a bias in the MC based correction for the energy loss in dead material in a front of the EM calorimeter.

A comparison of the di-electron mass distributions for the nominal MC sample and a MC sample with additional material can be found in Fig. 12.14. The mass peak for MC with

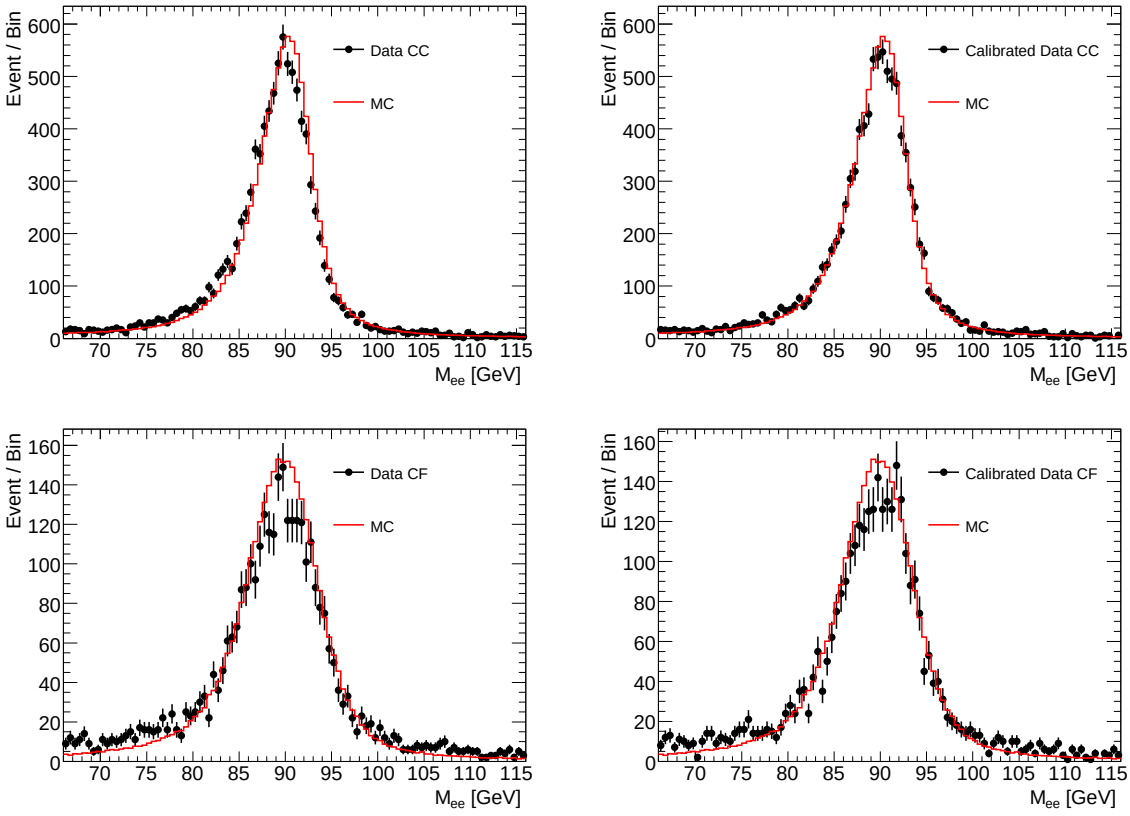

Figure 12.12: Comparison of the di-electron mass distribution between data and MC before (left) and after (right) calibration for the CC (top) and the CF (bottom) selections. These plots are normalized by the number of events.

additional material is shifted to a lower value. The impact of additional material on the electron energy scale can be found in Fig. 12.15. It is obtained by calibration of MC with additional material using nominal MC as a reference. As expected, the correction factors have negative values.

If additional material was present in data, the calibration correction factors extracted from $Z \to e^+e^-$ events would restore the electron energy scale on average. $p_{T,Z}$ spectrum of Z boson decay has a most probable value around 45 GeV and a mean value around 40 GeV. The calibration and systematic uncertainties obtained from $Z \to e^+e^-$ decays have to be extrapolated to electron energy regions not well populated by these events.

The systematic uncertainties due to the additional material can be estimated by the following procedure. At the first step, MC with additional material needs to be calibrated by the nominal MC. Then the non-linearity is measured using MC truth information by comparison of the most probable value of the $E_{\mathrm{rec}}/E_{\mathrm{gen}}$ distribution between the nominal MC sample and the sample with additional material.

The $p_{T,e}$-dependent systematic uncertainties are shown in Fig. 12.16. For this estimation, an additional $10 < p_{T,e} < 20$ GeV bin is used. Uncertainties in η_e and $p_{T,e}$ vary from -1.5% to

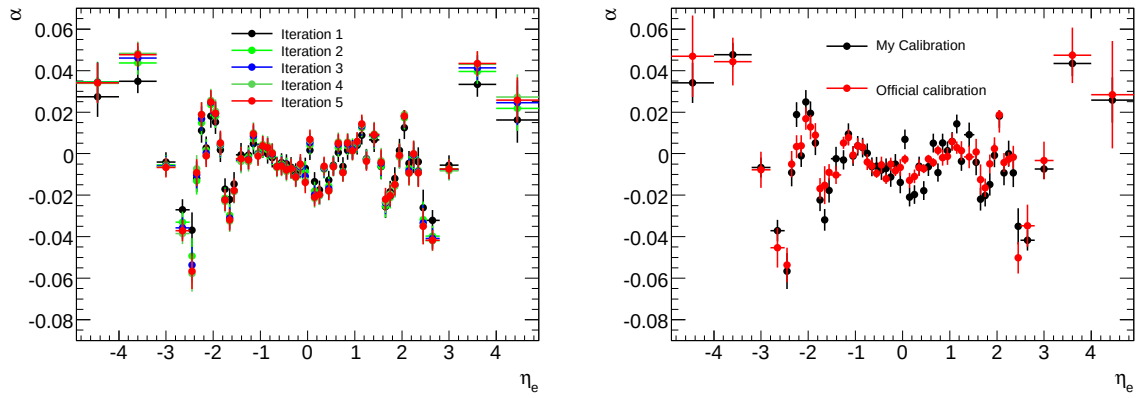

Figure 12.13: Left: calibration correction factors for 5 iterations of the 2010 data calibration. Right: comparison of the presented calibration correction factors and the official ATLAS result.

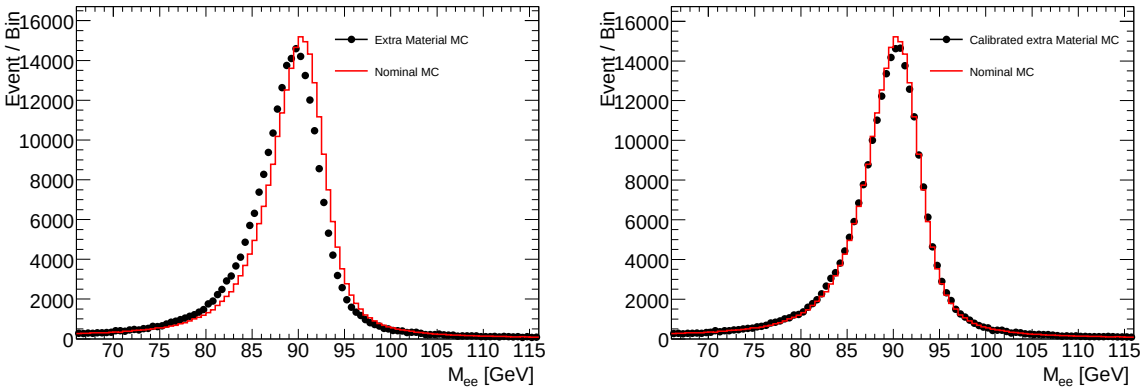

Figure 12.14: Comparison of the di-electron mass distribution for nominal MC and MC with additional material before calibration (left) and after calibration (right).

2%. As expected, the uncertainties are very small for $p_{T,e} = 40$ GeV.

12.4.5 Pre-sampler energy scale

A detailed study of the pre-sampler energy scale was performed by "e/gamma" group and presented in [2]. The uncertainty of the energy scale of the EM calorimeter can be different from the pre-sampler energy scale since it is a different detector. The upper limit to the detector energy-scale uncertainty was estimated by comparison of the energy deposited in the pre-sampler between data and MC simulation by electrons from $W \to e\nu$ events. The values is about $\pm 5\%$ in the EMB and $\pm 10\%$ in the EMEC ($|\eta_e| < 1.8$).

Since calibration only fixes one overall scale and therefore can not correct for the differences between the pre-sampler and EM calorimeter energy scale, these differences are propagated to the calibration uncertainties. The bias on the electron energy scale due to a shift of the pre-sampler energy scale was calculated in $|\eta_e|$ and $p_{T,e}$ bins. The dependencies in $|\eta_e|$ bins are explained by the differences in the material distribution in a from of calorimeter, while

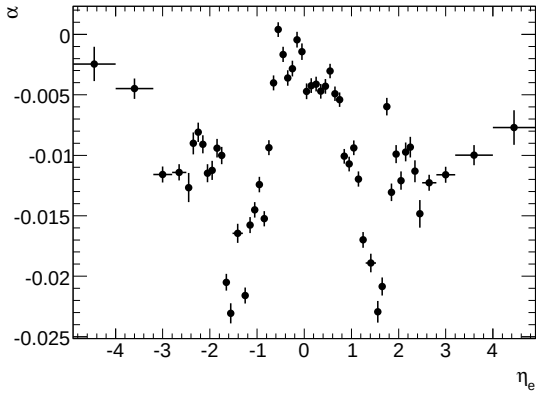

Figure 12.15: The correction factors (after 3 iterations) for calibration of the MC with additional material, using nominal MC as reference.

dependencies in $p_{T,e}$ bins by the dependencies in a fraction of energy deposited in the pre-sampler (the fraction of energy deposited in the pre-sampler is larger for lower $p_{T,e}$).

The presented correction factors, which are extracted from $Z \to e^+e^-$ events, would correct the electron energy scale on average for any bias on the pre-sampler energy scale. Therefore the non-linearity should be 0 for the average $p_{T,e} \sim 40$ GeV. The uncertainties due to the pre-sampler energy scale are $p_{T,e}$-dependent and vary from -1% to 1% for $|\eta_e| < 1.8$.

12.4.6 Non-ideal detector conditions

During the 2010 data taking, about 2% of the readout channels of the EM calorimeter were disabled. 6% of the readout channels were also not at the nominal high-voltage. Electrons falling in the regions corresponding to disabled readout channels were removed from the analysis. For electrons in the region corresponding to non-nominal high-voltage a correction was applied to compensate signal losses.

Possible calibration bias can be estimated by applying the tighter selection for low quality electrons, e.g. to exclude regions with non nominal high voltage. The effect is small and mostly appears in the forward region.

12.4.7 Energy non-linearity

Studies of a non-linearity of the EM calorimeter response would provide a cross check of the systematic uncertainties calculated before. The non-linearity is studied after applying the nominal $|\eta_e|$-dependent calibration. The uncertainty due to the energy non-linearity can be estimated by the calibration of the data in $|\eta_e|$ and $p_{T,e}$ bins. Fig. 12.17 shows the result of this estimation. The total uncertainty bands which are assigned for the energy scale systematic uncertainties is also shown. For all regions, the data is found to be within the uncertainty bands. The non-linearity effect in the high $p_{T,e}$ region is poorly estimated due to the low statistics, especially in the forward region.

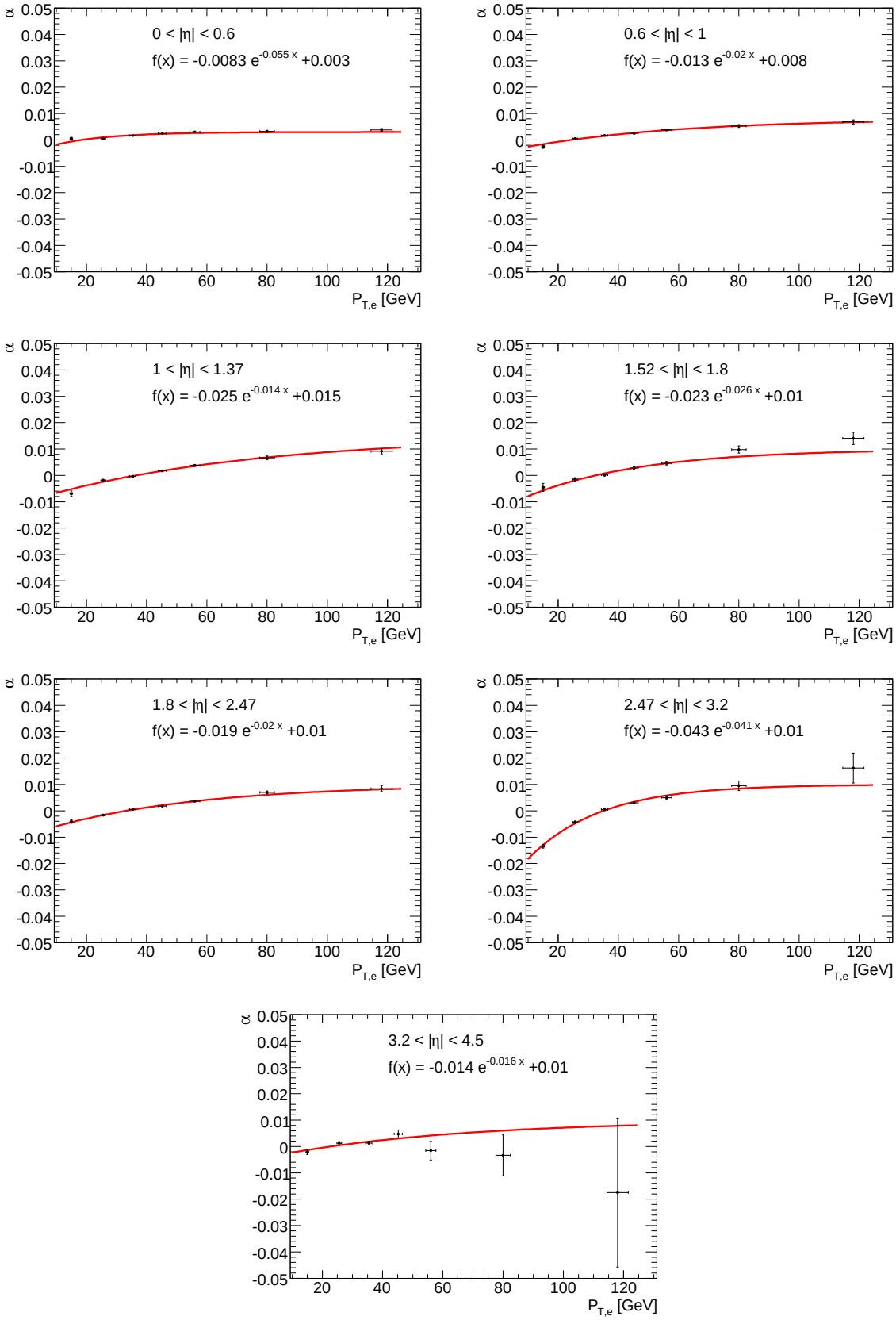

Figure 12.16: Differences of the maximum probable value of the $E_{\mathrm{rec}}/E_{\mathrm{gen}}$ distributions between the nominal MC and the MC with additional material. In the latter case, η_e-dependent energy scale correction measured in the same sample are applied. Parameterization: $f(x) = ae^{bx} + c$ is presented.

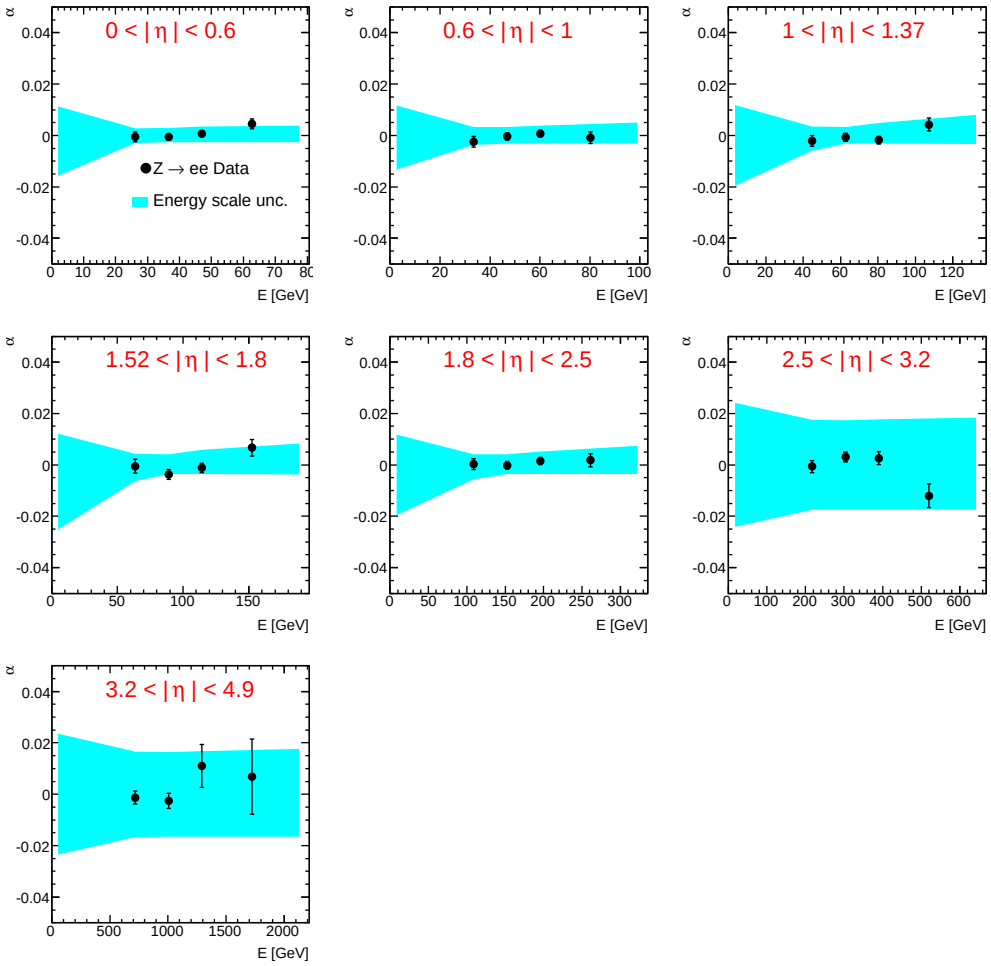

Figure 12.17: The correction factors α are determined in $|\eta_e|$ and $p_{T,e}$ bins using $Z \to e^+e^-$ events, which were preliminary corrected by the central calibration in η_e bins. The (blue) bands represent the sum of statistical and systematic uncertainties on the energy scale.

12.4.8 Summary

A summary of all systematic uncertainties can be found in Tab. 12.3. The uncertainties for $10 < p_{T,e} < 20$ GeV are based on the MC with extra material studies (see Fig. 12.16). Fig. 12.18 shows the overall uncertainly of the electron energy calibration. For the forward region, uncertainties are 2-3 times larger compared to the central region. Uncertainties for $p_{T,e} = 40$ GeV (around the peak) are smaller. There were no studies performed for the uncertainties in the crack region $1.37 < |\eta_e| < 1.52$ and a conservative 5% uncertainty on the electron energy scale is assumed here.

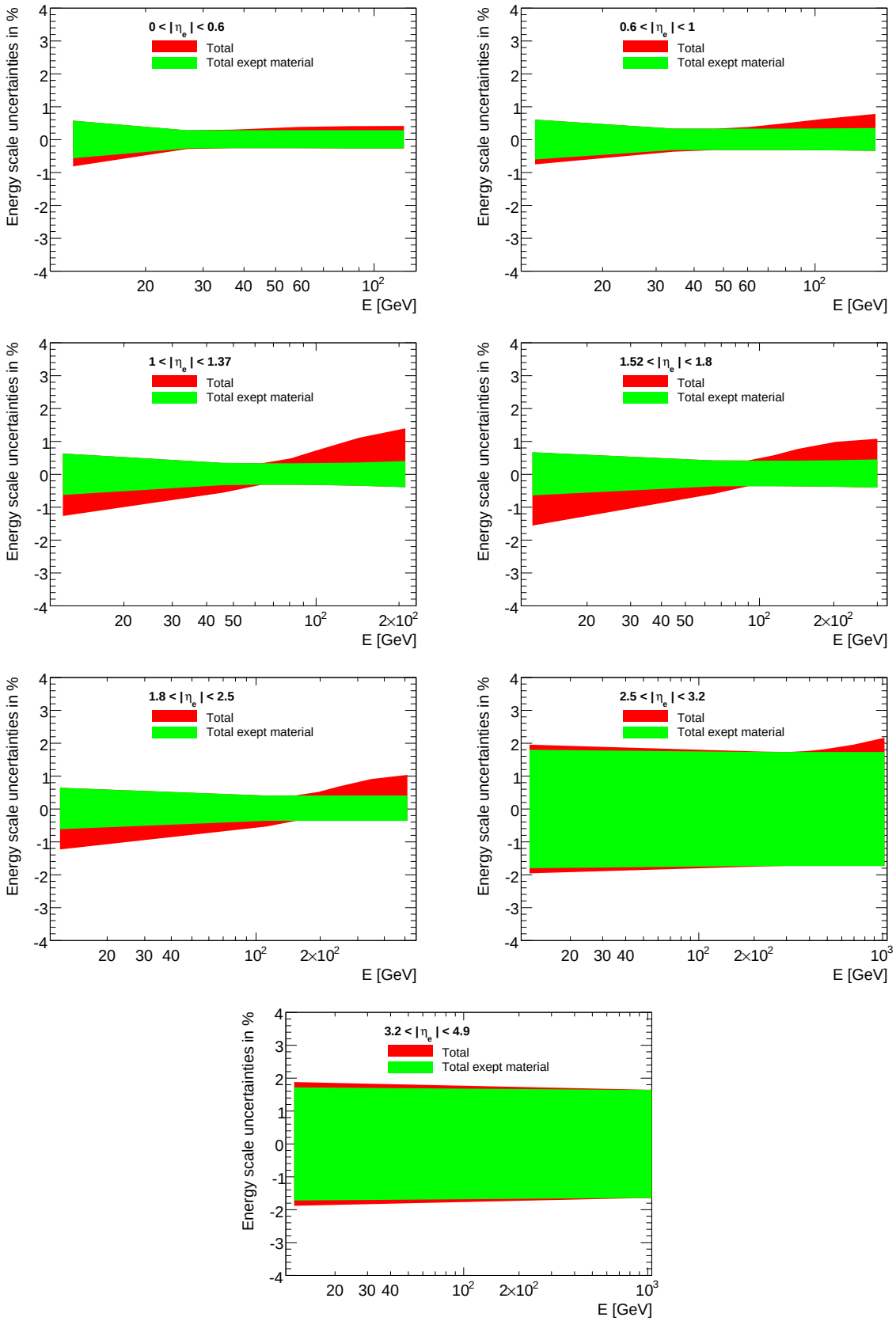

Figure 12.18: Total uncertainty of the electron energy scale with (red) and without (green) the uncertainty due to additional material.

	0.0-0.6	0.6-1.0	1.0 - 1.37	1.52-1.8	1.8 - 2.5	2.5 - 3.2	3.2 - 4.9
Statistical	± 0.1	± 0.2	± 0.2	± 0.2	± 0.2	± 0.5	± 1
Background	± 0.2	± 0.2	± 0.2	± 0.3	± 0.3	$+0.8/-0.3$	$+1.1/-0.8$
MC Closure	± 0.1	± 0.1	± 0.1	± 0.1	± 0.1	± 0.2	± 0.2
Theoretical	± 0.1	± 0.1	± 0.1	± 0.1	± 0.1	± 0.1	± 0.1
Extra-Material	$p_{T,e}$ dependent from -1.5% to 2%						
Detector Condition	$< \pm 0.1$	$< \pm 0.1$	$< \pm 0.1$	$< \pm 0.1$	$< \pm 0.1$	± 0.2	± 0.3
Pre-samples energy scale	$p_{T,e}$ dependent from -1% to 1% for $\lvert\eta_e\rvert < 1.8$						

Table 12.3: Summary of systematic uncertainties of the electron energy calibration.

CHAPTER 13

Efficiency studies

A precise measurement of the various components of the electron reconstruction efficiency for data and MC and their ratio is essential for the analysis. This chapter describes electron reconstruction $\varepsilon_{\text{Reco}}$, ID ε_{ID}, Iso ε_{Iso} and trigger (TG) ε_{TG} efficiencies and the corresponding scale factors (SFs) which are defined as a ratio $\varepsilon^{\text{data}}/\varepsilon^{\text{MC}}$.

The efficiencies need to be measured in several steps. Each efficiency and the corresponding SF are determined with respect to a previous step. The reconstruction starts at the cluster level and measures the efficiency to reconstruct an electron. The ID efficiency measurement uses the reconstructed electrons and measures the efficiency of the ID "medium", ID "tight" or ID "forward loose". The Iso efficiency "CaloIso98" is measured with respect to the ID "tight", since it is used for the CF selection, where the central electron is required to be identified as "tight". The TG efficiency measurement is finally evaluated with respect to a sample with all off-line analysis cuts applied.

Values of the efficiencies are provided by "e/gamma" group: [2, 79]. The following sections present a calculation of the ID and Iso efficiencies and show comparisons with the official ATLAS results. TG and reconstruction efficiencies are taken from the official "e/gamma" recommendation.

13.1 Electron reconstruction efficiency for the central electron

The reconstruction efficiency is defined as the probability to reconstruct a central electron ($|\eta_e| < 2.47$), which has deposited its energy in a calorimeter cluster, as electron candidate by the "e/gamma" algorithm (see Sec. 8). The efficiency of the track quality (TQ) requirement (at least one pixel hit and seven silicon hits) is included to the reconstruction efficiency. $Z \to e^+e^-$ based tag-and-probe method was used to perform calculations. The ratio of data to MC efficiencies, which can be used as a SF for simulated events is [2] :

$$SF_{\text{Reco + TQ}} = 1.0126 \pm 0.0019(\text{stat}) \pm 0.0079(\text{syst}) = 1.0126 \pm 0.0082 \tag{13.1}$$

13.2 ID efficiency

To determine the electron ID efficiency, the tag-and-probe method based on $Z \to e^+e^-$ events is used. The method consists of tagging a strongly selected electron and probing the second electron (electron with relaxed ID cuts). The measurement is based on the CC selection in the central region and the CF selection in the forward region (both CC and CF selections are described in Sec. 9.2). Since for the CC selection both electrons are equivalent, each event is used twice: the first, the first electron is considered as a tag and second as a probe and the second the second electron is considered as a tag. For the CF selection the tag electron is always central. With respect to these selections the ID cuts are relaxed for the probe electron. For the tag electron, the additional central ID "tight", "CaloIso98" and TG match are applied. A higher electron $p_{T,e}$ threshold can be used for the tag electrons for additional background rejection.

The efficiency is calculated as the ratio of the number of the probe electrons passing ID selection to the number of all probe electrons:

$$\varepsilon_{ID} = \frac{N^{\text{probe with ID}}}{N^{\text{all probe}}}. \tag{13.2}$$

Since the nominator and denominator in Eq. 13.2 are correlated, the statistical uncertainty for the efficiency can be calculated as:

$$\delta\varepsilon_{ID} = \frac{\sqrt{(1-2\varepsilon)A^2 + \varepsilon^2 B^2}}{N^{\text{all probe}}}, \tag{13.3}$$

where A(B) is the statistical uncertainty of $N^{\text{probe with ID}}(N^{\text{all probe}})$. The background was estimated and subtracted using the methods described in Sec. 11.1. Since the selection with all probe electrons has a large fraction of background (10-25%), the value $N^{\text{all probe}}$ is more sensitive to the background determination procedure than $N^{\text{probe with ID}}$.

The result of the efficiency calculation is presented in 8 η_e bins for the central region and in 2 $|\eta_e|$ in the forward region. The bin definition is presented in Tab. 13.1. The binning was chosen with respect to the detector structure and available statistics. SFs are calculated for the ID "medium" and ID "tight" in the central region and for ID "forward loose" in the forward region (see definition of the ID levels in Sec. 8.3).

13.2.1 The results for the central electron efficiency

The systematic uncertainties of the SFs mostly arise from the background subtraction. Therefore different signal mass ranges ([66-116] GeV, [75-105] GeV, [80-100] GeV), different fit functions for the background (RooDecay, Landau, Exponential, Chebyshev) and different selections for the tag electron (ID "tight", ID "tight"+$p_{T,e} > 25$ GeV) were used for estimation of systematic uncertainties. Only results from "good" fits (see Sec. 11.5) were included for the determination of the systematic uncertainties.

The SFs are presented in Tabs. 13.2 and 13.3 for the ID "tight" and ID "medium" efficiency SFs, respectively.

Bin	η_e
1	-2.47 - -2.01
2	-2.01 - -1.52
3	-1.37 - -0.80
4	-0.80 - 0.00
5	0.00 - 0.80
6	0.80 - 1.37
7	1.52 - 2.01
8	2.01 - 2.47
Bin	$\|\eta_e\|$
EMEC_IW	2.5 - 3.2
FCAL	3.2 - 4.9

Table 13.1: The binning definition for the ID efficiency calculations in the central and forward regions.

η_e bins	1	2	3	4	5	6	7	8
Standard deviation:	0.007	0.028	0.029	0.005	0.021	0.020	0.017	0.034
RooFit $p_{T,e} > 20$ GeV sig: [66-116], Landau	0.967	0.984	1.044	0.973	0.976	1.045	1.043	1.031
RooFit $p_{T,e} > 20$ GeV sig: [75-105], Landau	0.962	1.000	1.048	0.977	0.983	1.055	1.059	1.030
RooFit $p_{T,e} > 20$ GeV sig: [80-100], Landau	0.958	1.011	1.052	0.982	0.991	1.063	1.088	1.029
RooFit $p_{T,e} > 20$ GeV sig: [75-105], RooDecay	0.961	C	1.024	0.972	1.023	1.035	R	R
RooFit $p_{T,e} > 20$ GeV sig: [80-100], RooDecay	R	C	C	0.984	1.033	C	R	R
RooFit $p_{T,e} > 25$ GeV sig: [66-116], Landau	0.978	0.995	1.027	0.977	0.977	1.055	1.050	1.014
RooFit $p_{T,e} > 25$ GeV sig: [75-105], Landau	0.976	1.010	1.035	0.981	X	1.062	1.079	1.017
RooFit $p_{T,e} > 25$ GeV sig: [80-100], Landau	**0.966**	**1.017**	**1.046**	**0.987**	**0.990**	**1.069**	**1.084**	**1.033**
RooFit $p_{T,e} > 25$ GeV sig: [66-116], Exp.	X	0.925	0.960	X	X	X	X	0.931
RooFit $p_{T,e} > 25$ GeV sig: [75-105], Exp.	X	X	0.984	X	X	1.003	X	X
RooFit $p_{T,e} > 25$ GeV sig: [80-100], Exp.	X	0.977	1.011	X	X	X	X	0.976

Table 13.2: The ID "tight" SFs estimated in η_e bins for central electrons using fits with different background functions and different mass ranges. Systematic uncertainties are calculated as standard deviation of these numbers. X - fit has $\chi^2/dof > 2$, C - background in the central band is larger than background in the side bands, R - background in the left side band is smaller than sum of background in the left side band and central band.

The values, which were obtained from the RooFit method with Landau background function, are accepted as a central values. In order to get smaller fraction of background, the signal window [80-100] and additional $p_{T,e} > 25$ GeV cut for the tag electron were used.

Another source of systematic uncertainties arises from the MC efficiency measurement. For the calculation of the central value of SFs, Eq. 13.2 is used for both data and MC, without any background subtraction for the MC calculation. However the MC sample potentially also can have a background, when the fake electrons are used for the Z boson construction. The systematic uncertainties due to this effect could be estimated as differences between MC efficiencies, calculated with and without truth match (which is described in Sec. 7.1.2). The truth matching requires $\Delta R < 0.2$ between reconstructed and generated electrons. The final

η_e bins	1	2	3	4	5	6	7	8
Standard deviation:	0.013	0.020	0.015	0.019	0.006	0.040	0.023	0.023
RooFit $p_{T,e} > 20$ GeV sig: [66-116], Landau	0.955	0.937	0.969	0.961	0.963	0.962	0.982	0.993
RooFit $p_{T,e} > 20$ GeV sig: [75-105], Landau	0.952	0.941	0.971	0.964	0.969	0.969	1.001	0.980
RooFit $p_{T,e} > 20$ GeV sig: [80-100], Landau	0.949	0.949	0.974	0.967	X	0.977	1.009	0.978
RooFit $p_{T,e} > 20$ GeV sig: [66-116], Chebuchev	0.950	0.981	X	X	X	1.035	1.037	1.035
RooFit $p_{T,e} > 20$ GeV sig: [75-105], Chebuchev	0.985	X	X	X	X	1.076	1.046	1.033
RooFit $p_{T,e} > 20$ GeV sig: [80-100], Chebuchev	0.979	R	X	1.003	X	1.049	1.048	1.025
RooFit $p_{T,e} > 25$ GeV sig: [66-116], Landau	0.973	0.944	0.960	0.968	0.961	0.970	0.990	0.992
RooFit $p_{T,e} > 25$ GeV sig: [75-105], Landau	X	0.927	0.965	0.971	X	0.976	1.004	0.993
RooFit $p_{T,e} > 25$ GeV sig: [80-100], Landau	**0.971**	**0.962**	**0.972**	**0.975**	**0.976**	**0.982**	**1.004**	**1.013**
RooFit $p_{T,e} > 25$ GeV sig: [66-116], RooDecay	R	C	0.982	X	C	C	C	C
RooFit $p_{T,e} > 25$ GeV sig: [75-105], RooDecay	0.961	0.985	0.984	1.016	R	C	C	C
RooFit $p_{T,e} > 25$ GeV sig: [80-100], RooDecay	R	C	1.015	C	R	R	C	C

Table 13.3: The ID "medium" SFs estimated in η_e bins for central electrons using fits with different background functions and different mass ranges. Systematic uncertainties are calculated as standard deviation of these numbers. X — fit has $\chi^2/dof > 2$, C — background in the central band is larger than background in the side bands, R — background in the left side band is smaller than sum of background in the left side band and central band.

result for ID efficiencies and SFs calculations is shown in Tabs. 13.4 and 13.5 for the ID "tight" and ID "medium" efficiency SFs, respectively. The systematic uncertainties for data efficiencies were calculated using different fits, while the systematic uncertainties for the SFs include both MC and data efficiency systematic uncertainties.

η_e	$\varepsilon^{\mathrm{MC}} \pm$ stat.$\pm$ syst	$\varepsilon^{\mathrm{data}} \pm$ stat $\pm$ syst	SF $\pm$ stat $\pm$ syst
-2.50 – -2.01	$0.693 \pm 0.001 \pm 0.004$	$0.669 \pm 0.016 \pm 0.007$	$0.966 \pm 0.016 \pm 0.008$
-2.01 – -1.37	$0.686 \pm 0.001 \pm 0.003$	$0.698 \pm 0.013 \pm 0.028$	$1.017 \pm 0.013 \pm 0.028$
-1.37 – -0.80	$0.742 \pm 0.001 \pm 0.003$	$0.776 \pm 0.009 \pm 0.029$	$1.046 \pm 0.009 \pm 0.029$
-0.80 – 0.00	$0.816 \pm 0.001 \pm 0.001$	$0.805 \pm 0.007 \pm 0.005$	$0.987 \pm 0.007 \pm 0.005$
0.00 – 0.80	$0.821 \pm 0.001 \pm 0.001$	$0.813 \pm 0.006 \pm 0.021$	$0.990 \pm 0.006 \pm 0.021$
0.80 – 1.52	$0.743 \pm 0.001 \pm 0.003$	$0.794 \pm 0.008 \pm 0.020$	$1.069 \pm 0.008 \pm 0.020$
1.52 – 2.01	$0.686 \pm 0.001 \pm 0.003$	$0.744 \pm 0.013 \pm 0.017$	$1.084 \pm 0.013 \pm 0.017$
2.01 – 2.50	$0.687 \pm 0.002 \pm 0.004$	$0.710 \pm 0.016 \pm 0.034$	$1.033 \pm 0.016 \pm 0.034$

Table 13.4: The electron ID "tight" efficiencies and SFs (data/MC efficiency) with statical and systematic uncertainties.

13.2.2 The results for the forward electron efficiency

The fraction of background for the CF analysis is much larger compared to the CC analysis, which leads to a large systematic uncertainties of the ID efficiency measurement. The systematic uncertainties are estimated using the same variations for the tag electron as for the CC selection. Additionally the template method was used for the estimation of the systematic uncertainty.

η_e	$\varepsilon^{\mathrm{MC}} \pm$ stat.$\pm$ syst	$\varepsilon^{\mathrm{data}} \pm$ stat $\pm$ syst	SF $\pm$ stat $\pm$ syst
-2.50 – -2.01	$0.901 \pm 0.001 \pm 0.005$	$0.875 \pm 0.011 \pm 0.013$	$0.971 \pm 0.011 \pm 0.014$
-2.01 – -1.37	$0.902 \pm 0.001 \pm 0.004$	$0.868 \pm 0.010 \pm 0.020$	$0.962 \pm 0.010 \pm 0.020$
-1.37 – -0.80	$0.939 \pm 0.001 \pm 0.004$	$0.913 \pm 0.006 \pm 0.015$	$0.972 \pm 0.006 \pm 0.016$
-0.80 – 0.00	$0.934 \pm 0.000 \pm 0.001$	$0.911 \pm 0.005 \pm 0.019$	$0.975 \pm 0.005 \pm 0.019$
0.00 – 0.80	$0.936 \pm 0.000 \pm 0.001$	$0.914 \pm 0.005 \pm 0.006$	$0.976 \pm 0.005 \pm 0.006$
0.80 – 1.52	$0.939 \pm 0.001 \pm 0.003$	$0.922 \pm 0.006 \pm 0.040$	$0.982 \pm 0.006 \pm 0.040$
1.52 – 2.01	$0.900 \pm 0.001 \pm 0.004$	$0.904 \pm 0.008 \pm 0.023$	$1.004 \pm 0.008 \pm 0.023$
2.01 – 2.50	$0.900 \pm 0.001 \pm 0.005$	$0.912 \pm 0.011 \pm 0.021$	$1.013 \pm 0.011 \pm 0.022$

Table 13.5: The electron ID "medium" efficiencies and SFs (data/MC efficiency) with statical and systematic uncertainties.

The result for different variations is shown in Tabs. 13.6 and 13.7 for the EMEC-IW and FCAL, respectively. The systematic uncertainties for data efficiency were estimated as standard deviation of the presented values.

The systematic uncertainties of the MC efficiencies is estimated using the same truth matching as it was described for the central electron. The values for both bins are about 0.7%. The final results for the ID "forward loose" efficiencies and SFs are shown in Tab. 13.8. The systematic uncertainties for SFs are calculated as quadratic sum of the MC and data efficiency systematic uncertainties.

13.2.3 Comparison with the "e/gamma" results

The ID efficiency SFs, provided by the "e/gamma" group, were calculated using tag-and-probe method for $Z \to e^+e^-$, $W \to e\nu$ and J/ψ events [2, 79]. A combined result of these channels improves accuracy and was accepted as the ATLAS official.

SFs for the forward region were calculated using $Z \to e^+e^-$ events only. Fig. 13.1 shows a comparison between the results of this analysis and the official ATLAS results. The values are found to be in a good agreement.

13.3 Iso efficiency

The Iso efficiencies for the "CaloIso98" were estimated using $Z \to e^+e^-$ events by the tag-and-probe method (similar to the ID efficiency estimation). The presented efficiencies were calculated with respect to the electron ID "tight".

The baseline CC selection with an additional ID "tight" cut for both electrons was used for this measurement. The efficiency is calculated as the ratio of the number of probe electrons passing "CaloIso98" to the number of all probe electrons: Eq. 13.2. Statistical uncertainties can be calculated by Eq. 13.3. Efficiencies and SFs are measured in the same η_e bins as presented in Tab. 13.1.

The remaining fraction of the background (less than 1%) was estimated by a fit (see

Standard deviation:	0.037
Template fit sig: [75-105], fit: [66-116]	0.977
Template fit sig: [75-105], fit: [66-130]	0.990
Template fit sig: [80-100], fit: [66-116]	0.937
Template fit sig: [80-100], fit: [66-130]	0.951
RooFit $p_{T,e} > 20$ GeV sig: [66-116], fit: [40-140], Landau Bkg	0.924
RooFit $p_{T,e} > 20$ GeV sig: [66-116], fit: [60-120], Landau Bkg	1.009
RooFit $p_{T,e} > 20$ GeV sig: [66-116], fit: [60-120], Exponential Bkg	0.945
RooFit $p_{T,e} > 20$ GeV sig: [75-105], fit: [40-140], Landau Bkg	0.927
RooFit $p_{T,e} > 20$ GeV sig: [75-105], fit: [50-140], Landau Bkg	0.879
RooFit $p_{T,e} > 20$ GeV sig: [75-105], fit: [60-120], Landau Bkg	0.996
RooFit $p_{T,e} > 20$ GeV sig: [75-105], fit: [60-120], Exponential Bkg	0.949
RooFit $p_{T,e} > 20$ GeV sig: [80-100], fit: [40-140], Landau Bkg	0.945
RooFit $p_{T,e} > 20$ GeV sig: [80-100], fit: [50-140], Landau Bkg	0.920
RooFit $p_{T,e} > 20$ GeV sig: [80-100], fit: [60-120], Landau Bkg	1.018
RooFit $p_{T,e} > 20$ GeV sig: [80-100], fit: [60-120], Exponential Bkg	0.971
RooFit $p_{T,e} > 25$ GeV sig: [66-116], fit: [40-140], Landau Bkg	0.972
RooFit $p_{T,e} > 25$ GeV sig: [66-116], fit: [50-140], Exponential Bkg	0.914
RooFit $p_{T,e} > 25$ GeV sig: [66-116], fit: [60-120], Exponential Bkg	1.014
RooFit $p_{T,e} > 25$ GeV sig: [66-116], fit: [60-120], Exponential Bkg	0.980
RooFit $p_{T,e} > 25$ GeV sig: [75-105], fit: [40-140], Landau Bkg	0.974
RooFit $p_{T,e} > 25$ GeV sig: [75-105], fit: [50-140], Exponential Bkg	0.975
RooFit $p_{T,e} > 25$ GeV sig: [75-105], fit: [60-120], Exponential Bkg	1.028
RooFit $p_{T,e} > 25$ GeV sig: [75-105], fit: [60-120], Exponential Bkg	0.984
RooFit $p_{T,e} > 25$ GeV sig: [80-100], fit: [40-140], Landau Bkg	**0.987**
RooFit $p_{T,e} > 25$ GeV sig: [80-100], fit: [50-140], Exponential Bkg	0.990
RooFit $p_{T,e} > 25$ GeV sig: [80-100], fit: [60-120], Exponential Bkg	1.025
RooFit $p_{T,e} > 25$ GeV sig: [80-100], fit: [60-120], Exponential Bkg	1.003

Table 13.6: SFs (data/MC efficiency) for the ID "forward loose" efficiency in the FCAL. Values are calculated using different fits.

Standard deviation:	0.051
Template fit sig: [75-105], fit: [66-116]	0.914
Template fit sig: [75-105], fit: [66-130]	0.916
Template fit sig: [80-100], fit: [66-116]	0.929
Template fit sig: [80-100], fit: [66-130]	0.930
RooFit $p_{T,e} > 20$ GeV sig: [66-116], fit: [40-140], Landau Bkg	0.862
RooFit $p_{T,e} > 20$ GeV sig: [66-116], fit: [40-140], Chebuchev Bkg	0.934
RooFit $p_{T,e} > 20$ GeV sig: [66-116], fit: [50-140], Landau Bkg	0.918
RooFit $p_{T,e} > 20$ GeV sig: [66-116], fit: [60-120], Landau Bkg	0.948
RooFit $p_{T,e} > 20$ GeV sig: [75-105], fit: [40-140], Landau Bkg	0.877
RooFit $p_{T,e} > 20$ GeV sig: [75-105], fit: [40-140], Chebuchev Bkg	0.933
RooFit $p_{T,e} > 20$ GeV sig: [75-105], fit: [40-140], RooDecay Bkg	0.990
RooFit $p_{T,e} > 20$ GeV sig: [75-105], fit: [50-140], Landau Bkg	0.918
RooFit $p_{T,e} > 20$ GeV sig: [75-105], fit: [50-140], RooDecay Bkg	1.085
RooFit $p_{T,e} > 20$ GeV sig: [75-105], fit: [60-120], RooDecay Bkg	1.032
RooFit $p_{T,e} > 20$ GeV sig: [80-100], fit: [40-140], Landau Bkg	0.893
RooFit $p_{T,e} > 20$ GeV sig: [80-100], fit: [40-140], RooDecay Bkg	0.995
RooFit $p_{T,e} > 20$ GeV sig: [80-100], fit: [50-140], Landau Bkg	0.919
RooFit $p_{T,e} > 20$ GeV sig: [80-100], fit: [50-140], RooDecay Bkg	0.994
RooFit $p_{T,e} > 20$ GeV sig: [80-100], fit: [60-120], Landau Bkg	0.949
RooFit $p_{T,e} > 20$ GeV sig: [80-100], fit: [60-120], RooDecay Bkg	1.030
RooFit $p_{T,e} > 25$ GeV sig: [66-116], fit: [40-140], Landau Bkg	0.893
RooFit $p_{T,e} > 25$ GeV sig: [66-116], fit: [50-140], Landau Bkg	0.927
RooFit $p_{T,e} > 25$ GeV sig: [66-116], fit: [50-140], Exponential Bkg	0.856
RooFit $p_{T,e} > 25$ GeV sig: [66-116], fit: [50-140], Chebuchev Bkg	0.993
RooFit $p_{T,e} > 25$ GeV sig: [66-116], fit: [60-120], Landau Bkg	0.973
RooFit $p_{T,e} > 25$ GeV sig: [66-116], fit: [60-120], Exponential Bkg	0.945
RooFit $p_{T,e} > 25$ GeV sig: [75-105], fit: [40-140], Landau Bkg	0.903
RooFit $p_{T,e} > 25$ GeV sig: [75-105], fit: [50-140], Landau Bkg	0.925
RooFit $p_{T,e} > 25$ GeV sig: [75-105], fit: [50-140], Exponential Bkg	0.869
RooFit $p_{T,e} > 25$ GeV sig: [75-105], fit: [50-140], Chebuchev Bkg	0.992
RooFit $p_{T,e} > 25$ GeV sig: [75-105], fit: [50-140], RooDecay Bkg	1.032
RooFit $p_{T,e} > 25$ GeV sig: [75-105], fit: [60-120], Landau Bkg	0.955
RooFit $p_{T,e} > 25$ GeV sig: [75-105], fit: [60-120], Exponential Bkg	0.940
RooFit $p_{T,e} > 25$ GeV sig: [75-105], fit: [60-120], RooDecay Bkg	1.009
RooFit $p_{T,e} > 25$ GeV sig: [80-100], fit: [40-140], Landau Bkg	**0.915**
RooFit $p_{T,e} > 25$ GeV sig: [80-100], fit: [40-140], RooDecay Bkg	1.003
RooFit $p_{T,e} > 25$ GeV sig: [80-100], fit: [50-140], Landau Bkg	0.926
RooFit $p_{T,e} > 25$ GeV sig: [80-100], fit: [50-140], Exponential Bkg	0.885
RooFit $p_{T,e} > 25$ GeV sig: [80-100], fit: [60-120], Landau Bkg	0.955
RooFit $p_{T,e} > 25$ GeV sig: [80-100], fit: [60-120], Exponential Bkg	0.941
RooFit $p_{T,e} > 25$ GeV sig: [80-100], fit: [60-120], RooDecay Bkg	1.009

Table 13.7: SFs (data/MC efficiency) for the ID "forward loose" efficiency in the EMEC-IW. The values are calculated using different fits.

$\|\eta_e\|$	Fwd.Loose SF $\pm$ stat $\pm$ syst
2.5 - 3.2	$0.915 \pm 0.015 \pm 0.052$
3.2 - 4.9	$0.987 \pm 0.031 \pm 0.038$

Table 13.8: The electron ID "forward loose" efficiencies and SFs (data/MC efficiency) with statistical and systematic uncertainties for the forward region.

Sec. 11.5) and provides a small systematic uncertainties for the efficiency measurement. Tab. 13.9 shows various SFs obtained from different fits, and selections with different threshold of the electron $p_{T,e}$. The systematic uncertainties are estimated as standard deviation of the different SFs.

Standard deviation:	0.004	0.003	0.005	0.006	0.005	0.005	0.010	0.004
RooFit $p_{T,e} > 20$ GeV sige: [66-116], Landau	0.983	1.000	0.989	0.996	0.987	0.996	0.998	0.971
RooFit $p_{T,e} > 20$ GeV sige: [66-116], Exp.	0.978	0.999	0.990	0.994	0.990	0.986	X	0.971
RooFit $p_{T,e} > 20$ GeV sige: [66-116], RooDecay	0.973	1.004	0.987	0.994	0.984	0.988	R	0.970
RooFit $p_{T,e} > 20$ GeV sige: [75-105], Landau	0.984	0.999	0.991	0.998	0.989	0.995	1.001	0.974
RooFit $p_{T,e} > 20$ GeV sige: [75-105], Exp.	0.980	1.002	0.992	0.996	0.992	0.988	X	0.974
RooFit $p_{T,e} > 20$ GeV sige: [75-105], RooDecay	0.970	C	1.008	1.007	0.993	0.998	R	0.975
RooFit $p_{T,e} > 20$ GeV sige: [80-100], Landau	0.984	1.005	0.994	1.000	0.994	0.995	1.004	0.978
RooFit $p_{T,e} > 20$ GeV sige: [80-100], Exp.	0.982	1.006	0.994	0.998	0.994	0.990	X	0.977
RooFit $p_{T,e} > 20$ GeV sige: [80-100], RooDecay	R	1.009	C	1.013	C	C	0.971	R
RooFit $p_{T,e} > 25$ GeV sige: [66-116], Landau	0.972	1.006	0.988	0.996	0.987	0.997	0.997	0.974
RooFit $p_{T,e} > 25$ GeV sige: [66-116], Exp.	0.978	X	0.990	0.994	0.990	0.987	X	0.974
RooFit $p_{T,e} > 25$ GeV sige: [66-116], RooDecay	X	1.004	0.987	0.995	1.007	0.990	R	0.971
RooFit $p_{T,e} > 25$ GeV sige: [75-105], Landau	0.975	1.004	0.990	0.997	0.990	0.997	0.999	0.969
RooFit $p_{T,e} > 25$ GeV sige: [75-105], Exp.	0.980	X	0.992	0.996	0.992	0.989	X	0.976
RooFit $p_{T,e} > 25$ GeV sige: [75-105], RooDecay	0.980	C	R	0.983	0.994	1.004	R	0.981
RooFit $p_{T,e} > 25$ GeV sige: [80-100], Landau	**0.978**	**1.004**	**0.993**	**0.999**	**0.995**	**0.996**	**1.001**	**0.971**
RooFit $p_{T,e} > 25$ GeV sige: [80-100], Exp.	0.982	X	0.994	0.998	0.994	0.991	X	0.978

Table 13.9: SFs (data/MC efficiency) for the Iso efficiency in η_e bins. The values are calculated using different fits. X — fit has $\chi^2/dof > 2$, C — background in the central band is larger than background in the side bands, R — background in the left side band is smaller than sum of background in the left side band and central band.

Tab. 13.10 presents the final results with statistical and systematic uncertainties. The systematic uncertainties of the MC efficiencies are estimated using the same truth matching as it was described for the ID efficiency calculation.

The Iso SFs, which were accepted as officially recommended for analysis in ATLAS were calculated in a finer binning, and therefore have a larger statistical uncertainly. The comparison between presented SFs and the official recommendation shown in Fig. 13.2. All numbers are in agreement.

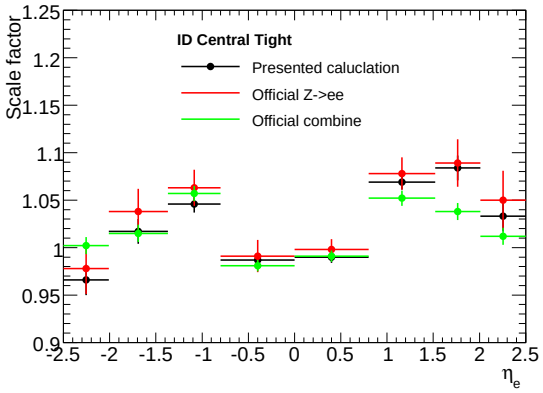

(a) SFs ID "tight"

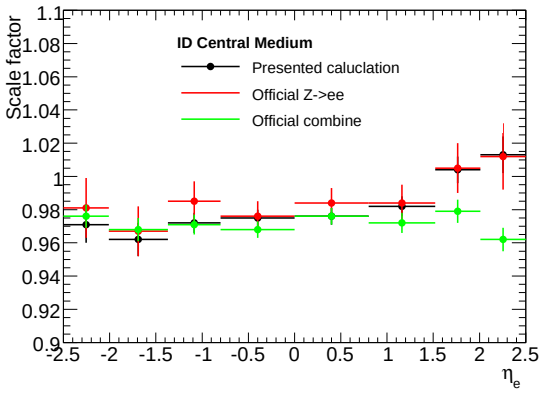

(b) SFs ID "medium"

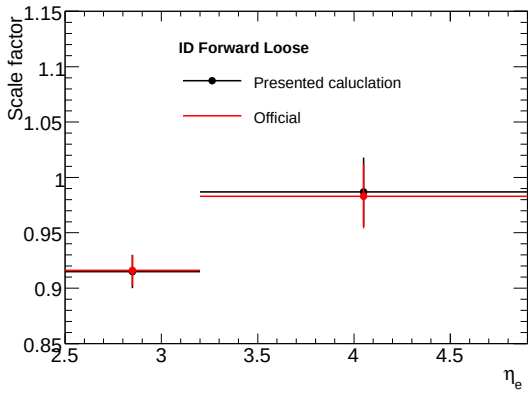

(c) SFs ID "forward loose"

Figure 13.1: Comparison of the ID SFs for the central ID "tight" (a), ID "medium" (b) and ID "forward loose" (c) efficiency between presented and the official ATLAS results. Only statistical uncertainties are shown.

η_e	$\varepsilon^{\mathrm{MC}} \pm$ stat.$\pm$ syst	$\varepsilon^{\mathrm{data}} \pm$ stat $\pm$ syst	SF $\pm$ stat $\pm$ syst
-2.50 - -2.01	$0.974 \pm 0.0003 \pm 0.0006$	$0.953 \pm 0.007 \pm 0.007$	$0.978 \pm 0.007 \pm 0.007$
-2.01 - -1.37	$0.974 \pm 0.0002 \pm 0.0001$	$0.978 \pm 0.004 \pm 0.003$	$1.004 \pm 0.004 \pm 0.003$
-1.37 - -0.80	$0.975 \pm 0.0002 \pm 0.0002$	$0.968 \pm 0.004 \pm 0.005$	$0.993 \pm 0.004 \pm 0.005$
-0.80 - 0.00	$0.975 \pm 0.0001 \pm 0.0003$	$0.974 \pm 0.003 \pm 0.005$	$0.999 \pm 0.003 \pm 0.005$
0.00 - 0.80	$0.975 \pm 0.0001 \pm 0.0003$	$0.970 \pm 0.003 \pm 0.005$	$0.995 \pm 0.003 \pm 0.005$
0.80 - 1.52	$0.974 \pm 0.0002 \pm 0.0002$	$0.970 \pm 0.004 \pm 0.005$	$0.996 \pm 0.004 \pm 0.005$
1.52 - 2.01	$0.975 \pm 0.0002 \pm 0.0003$	$0.976 \pm 0.004 \pm 0.007$	$1.001 \pm 0.004 \pm 0.007$
2.01 - 2.50	$0.973 \pm 0.0004 \pm 0.0003$	$0.945 \pm 0.007 \pm 0.004$	$0.976 \pm 0.007 \pm 0.004$

Table 13.10: The electron Iso efficiencies and SFs (data/MC efficiency) with statical and systematic uncertainties for the central region.

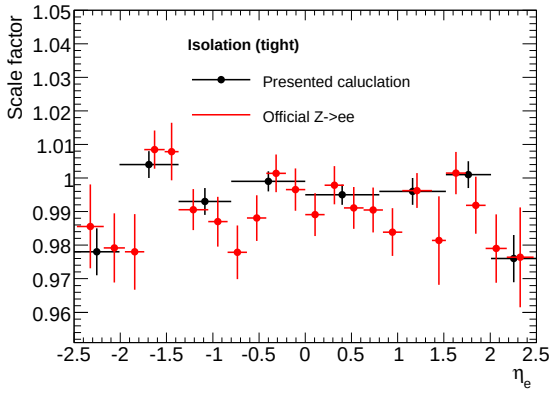

Figure 13.2: Comparison of the Iso SFs with respect of the ID "tight" for presented calculation and the official ATLAS recommendation.

13.4 TG efficiency

Since for 2010 data analysis two TGs (L1_EM14 and EF_e15_medium) were used, the final TG efficiency must be calculated using combination of the individual TG efficiencies.

The efficiency is calculated with respect to the off-line electron ID "medium" and ID "tight" using the tag-and-probe method applied to $Z \to e^+e^-$ and $W \to e\nu$ events. The efficiencies are almost flat in η_e and $p_{T,e}$ bins and higher than 98% for EF_e15_medium and 99% for L1_EM14.

Since most of the data were collected with the EF_e15_medium TG, the corresponding SF has larger significance. Both SFs are very close to each other and to 1 (see Tab. 13.11).

off-line Selection	$\varepsilon^{\text{data}}$	ε^{MC}	SF for $Z \to e^+e^-$	SF combined
ID "medium"	98.7 ± 0.1	99.235 ± 0.006	0.9943 ± 0.0013	0.995 ± 0.004
ID "tight"	99.02 ± 0.09	99.540 ± 0.005	0.9948 ± 0.0013	

Table 13.11: TG efficiencies and SFs (data/MC efficiency) for EF_e15_medium TG. The SFs are presented with both statistical and systematic uncertainties, while uncertainties for efficiencies is only statistical. Combined value summarize results, which was obtained in $Z \to e^+e^-$ and $W \to e\nu$ channels.

CHAPTER 14

Cross-section $\sigma(Z \to e^+e^-)$ results

The first section of this chapter summarizes studies of the integrated and differential acceptance (defined in Sec. 7). Control plots for both the CC and CF analyses are also shown in this section. The systematic uncertainties for cross section are shown in the next section. The cross-section results for both the CC and CF analyses and their combination are presented in third and fourth sections, respectively. The last section of the chapter describes a comparison of the data with theoretical calculations.

14.1 $Z \to e^+e^-$ acceptance

14.1.1 The CC selection

The integrated values of A_Z and C_Z (defined in Sec. 7), and the differential C_Z and $C_{\text{comb}} = C_Z/E$ (where E is the extrapolation factor) are calculated using MC@NLO $Z \to e^+e^-$ MC sample. Tab. 14.1 presents A_Z and C_Z factors for the integrated cross-section measurement. Tab. 14.2 shows C_Z and C_{comb} together with the event yield for the differential measurement. For the CC selection, a total of the 9725 Z boson candidates passed all selection criteria.

A_Z	$0.445 \pm 0.01\% \pm 2.0\%$
C_Z	$0.617 \pm 0.02\% \pm 2.6\%$

Table 14.1: The integrated values of A_Z and C_Z factors for the CC analysis, which are used in the cross-section calculation, with absolute statistical and systematic uncertainties.

14.1.2 The CF selection

For the CF selection a total of 3377 $Z \to e^+e^-$ candidates passed all selection criteria. The integrated values of A_Z and C_Z as well as the differential C_Z and $C_{\text{comb}} = C_Z/E$ (where E is the extrapolation factor) are calculated using MC@NLO $Z \to e^+e^-$ MC sample. Tab. 14.3 shows C_Z and C_{comb} together with the event yield for the differential measurement. Tab. 14.4 presents A_Z and C_Z factors for the integrated cross-section measurement.

$\|y_Z\|$	N_{data}	$C_{\text{comb}} \pm \text{stat}(\%) \pm \text{syst}(\%)$	$C_Z \pm \text{stat}(\%) \pm \text{syst}(\%)$
0.00 - 0.40	2447	$0.619 \pm 0.1 \pm 2.5$	$0.650 \pm 0.1 \pm 2.5$
0.40 - 0.80	2214	$0.585 \pm 0.1 \pm 2.6$	$0.649 \pm 0.1 \pm 2.5$
0.80 - 1.20	2050	$0.539 \pm 0.1 \pm 2.8$	$0.631 \pm 0.1 \pm 2.8$
1.20 - 1.60	1641	$0.449 \pm 0.1 \pm 3.0$	$0.602 \pm 0.1 \pm 3.0$
1.60 - 2.00	960	$0.284 \pm 0.1 \pm 3.2$	$0.555 \pm 0.1 \pm 3.1$
2.00 - 2.40	405	$0.131 \pm 0.1 \pm 4.1$	$0.482 \pm 0.2 \pm 3.7$

Table 14.2: Event yields, C_{comb} and C_Z factors for the CC analysis.

$\|y_Z\|$	N_{data}	$C_{\text{comb}} \pm \text{stat}(\%) \pm \text{syst}(\%)$	$C_Z \pm \text{stat}(\%) \pm \text{syst}(\%)$
1.20 - 1.60	187	$0.050 \pm 0.0 \pm 6.5$	$0.481 \pm 0.2 \pm 6.4$
1.60 - 2.00	716	$0.169 \pm 0.1 \pm 6.3$	$0.517 \pm 0.1 \pm 6.3$
2.00 - 2.40	930	$0.266 \pm 0.1 \pm 5.9$	$0.451 \pm 0.1 \pm 5.8$
2.40 - 2.80	969	$0.327 \pm 0.1 \pm 5.6$	$0.409 \pm 0.1 \pm 5.6$
2.80 - 3.60	567	$0.164 \pm 0.1 \pm 8.9$	$0.408 \pm 0.1 \pm 8.9$

Table 14.3: Event yields, C_{comb} and C_Z factors for the CF analysis.

14.1.3 Control Plots

Comparisons of data and MC including all corrections are presented in Figs. 14.1 and 14.2 for the CC and CF selections, respectively. The QCD background shape (as described in Sec. 11.1) is taken from a selection with inverted ID cuts and normalized by the total number of the background events. The presented background includes EW components. All figures show a reasonable agreement between data and MC. The peak of the electron $p_{T,e}$ distribution is shifted to the low p_T region for the CF analysis. The background is large for low electron $p_{T,e}$. The electron η_e distribution shows the structure of the calorimeter with the crack region between the EMB and EMEC (around $|\eta_e| = 1.5$) and between the EMEC and FCAL (around $|\eta_e| = 3.2$).

14.2 Systematic uncertainties of the cross-section calculation

The cross-section measurement relies on various corrections applied to the data and MC. Each correction has statistical and systematic uncertainties, which need to be properly propagated

A_Z	$0.198 \pm 0.00\% \pm 2.0\%$
C_Z	$0.441 \pm 0.01\% \pm 5.5\%$

Table 14.4: The integrated values of A_Z and C_Z factors for the CF analysis, which are used in the cross-section calculation with absolute statistical and systematic uncertainties.

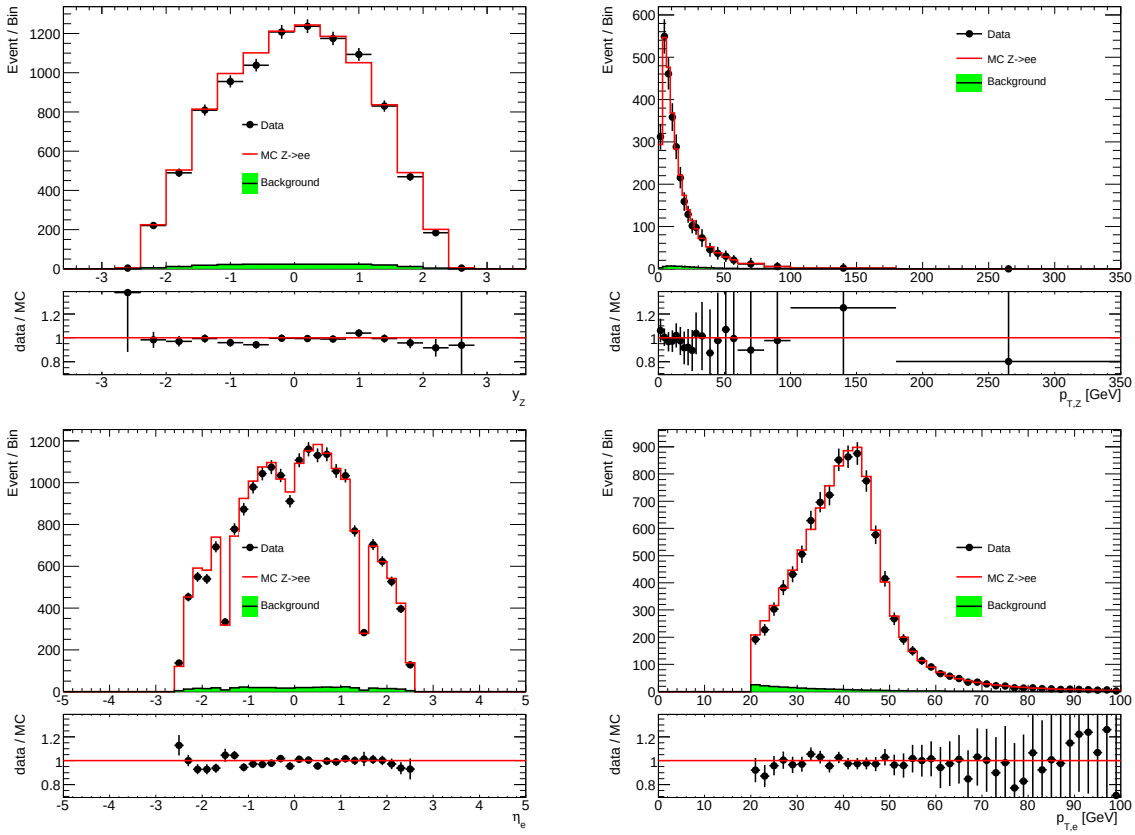

Figure 14.1: Control plots for the CC selection for $p_{T,Z}$, y_Z, $p_{T,e}$ and η_e distributions. Symbols with error bars represent data with statistical uncertainties. Lines show predictions of MC@NLO simulation. Background contribution is added to the MC prediction.

to the systematic uncertainties of the cross section. Two methods were used in order to propagate these uncertainties. The first of them is the bootstrap method [80], which is used for propagation of a bin-to-bin correlated uncertainty. The second method is used for propagation of uncorrelated uncertainty and is called toy MC.

14.2.1 Bootstrap method

MC samples used for the estimation of systematic uncertainties have limited statistics leading to statistical uncertainty for the estimated values of the systematic uncertainties. The bootstrap method allows this statistical component of the uncertainty to be estimated.

For each event, a vector with $N = 100$ Poisson-distributed random numbers with a mean $\mu = 1$ is prepared. These numbers are used as additional event weights, they have positive integer values, starting from 0. Weight 0 means that the event is rejected from the sample, weight $K \geq 1$ means that the event is used K-times. This way the original event sample is re-sampled ("bootstrapped") into N alternative samples using sampling with replacement method.

The SFs are then varied up and down in each event by their systematic uncertainties. The

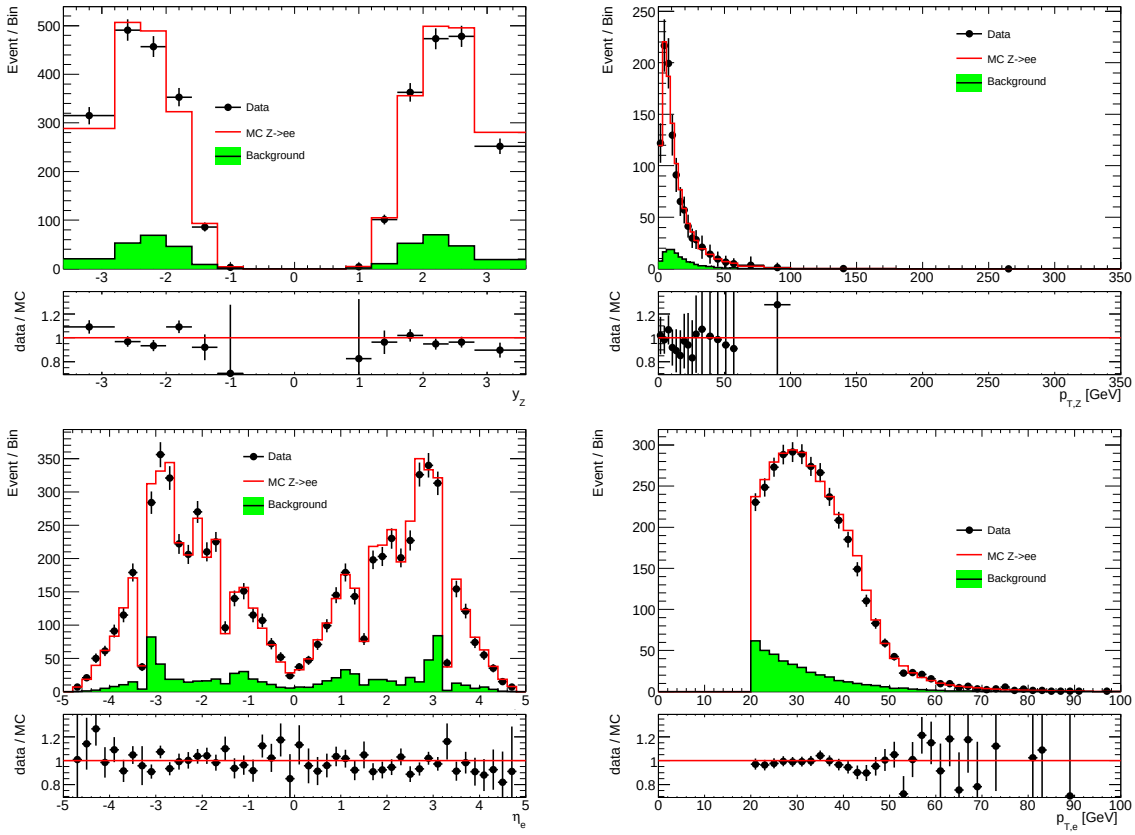

Figure 14.2: Control plots for the CF selection for $p_{T,Z}$, y_Z, $p_{T,e}$ and η_e distributions. Symbols with error bars represent data with statistical uncertainties. Lines show predictions of MC@NLO simulation. Background contribution is added to the MC prediction.

sum of weights over the reconstructed events is measured for each of the bootstrapped samples and C_Z^{up} and C_Z^{down} factors are calculated for corresponding SF variations. The correlated systematic uncertainty on C_Z is determined as an average over the bootstrapped samples of $s = (C_Z^{up} - C_Z^{down})/2$. The standard deviation of s over the bootstrapped samples is used to estimate the statistical component of this correlated uncertainty.

Fig. 14.3 shows an example of the bootstrap method for propagation of the electron energy calibration uncertainty. The left panel shows the $|y_Z|$ distribution for different bootstrap numbers Bs_i. In the right panel, which shows propagation of the resulting uncertainty, the shift is the estimated systematic bias and the spread is the statistical uncertainty. Since the statistical uncertainty is comparable or even smaller than the systematic, it can be concluded that the bias is estimated correctly and that the sample has enough statistics.

14.2.2 The toy MC method

The toy MC method, which is used for propagation of uncorrelated systematic uncertainties, starts with preparing N (e.g. N=100) tables of biases B_i, where i runs over tables. Each bias is taken as a Gaussian random number with mean 0 and standard deviation equal to

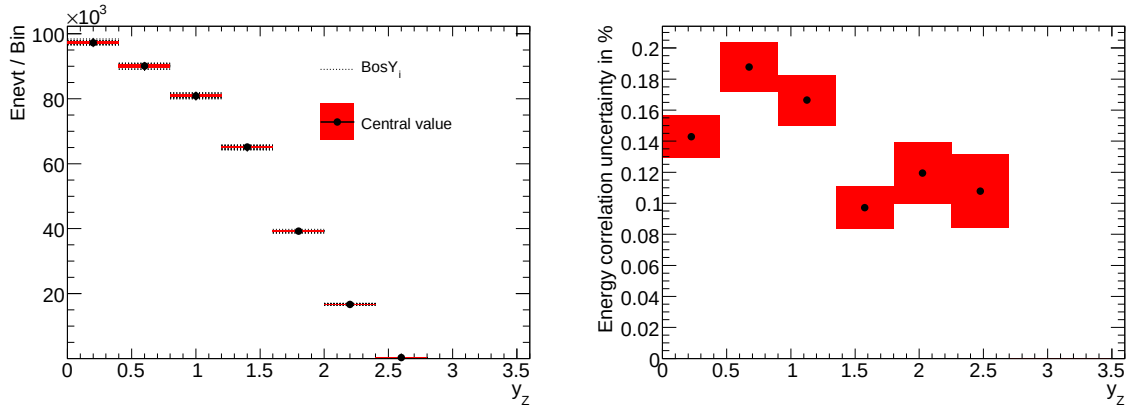

Figure 14.3: Several y_Z distribution for different bootstrap numbers (left). Resulting uncertainty propagation, the shift is the estimated systematic bias and the spread is MC uncertainty (right).

the uncorrelated uncertainty, which needs to be propagated. In the following we will discuss uncorrelated uncertainty of a scale factor as an example.

The tables of biases are used to prepare N samples of the scale factors C_Z. Then the C_Z factor is calculated N times. For each event, correction biases are used instead of SF:

$$SF_1 \times SF_2 \Longrightarrow (SF_1 + B_{i,1}) \times (SF_2 + B_{i,2}), \tag{14.1}$$

where $B_{i,1}$ and $B_{i,2}$ correspond to the first and second electrons respectively. Final C_Z systematic uncertainty is calculated as the standard deviation of these N samples.

Fig. 14.4 shows the deviation of the 100 C_Z values in percentage in a given bin as an example of the toy MC method for propagation of the uncorrelated ID efficiency for the CC analysis.

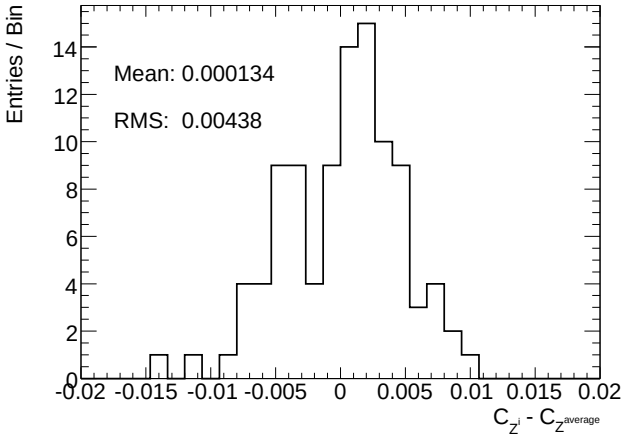

Figure 14.4: Deviation of 100 C_Z values.

14.2.3 $Z \to e^+e^-$ systematic uncertainties for the CC selection

A summary of the systematic uncertainties for the CC analysis is presented differentially in Tabs. 14.5 (correlated uncertainties) and 14.6 (uncorrelated uncertainties) and integrated in Tab. 14.7. Dominant uncertainties come from electron reconstruction and ID efficiency corrections. All values are discussed below.

Since the TG efficiency is about 99.5% (see Sec. 13.4) for single electron above 20 GeV, the probability that two electrons can fail the TG is less than 0.1%, that leads to an efficiency of effectively 100% with negligible systematic uncertainty.

The SF for reconstruction efficiency correction (see Sec. 13.1) has 0.82% uncertainty. This gives 1.63% uncertainty for two electrons.

The η_e dependent SFs for ID efficiency correction (see Sec. 13.2) with their statistical and systematic uncertainties were propagated by the methods described before. The uncorrelated part of the uncertainty gives 0.44% systematic uncertainties (for the integrated value). The correlated part of uncertainty leads to 1.7% uncertainty for the cross section.

The electron energy calibration described in Sec. 12.3 was applied for data. However systematic uncertainties due to the uncertainties of the calibration correction factors were studied on MC, because MC has larger statistics. The result is +0.24% and -0.13% for the up and down uncertainty of the calibration respectively, which gives an symmetrised result of 0.18%. Finally, only the symmetrised result is used.

Electron energy smearing (see Sec. 12.2) could also be a source of systematic uncertainty. The differences in C_Z due to applying smearing are about 0.1%. Therefore the systematic uncertainty due to energy resolution is below 0.1% and negligible.

The MC sample was reweighted in the number of vertices to data (see Sec. 6.4). The systematic uncertainty, which comes from this procedure is about 0.3% and does not depend much on y_Z. This 0.3% is taken as a systematic uncertainty due to the pileup reweighting for all bins.

The efficiency of reconstructing electrons in a problematic region of the EM calorimeter could be very low. Most of these problematic regions are due to the broken OTX modules, which were excluded from the analysis using the OTX cut. The corresponding uncertainty is estimated as 0.4% per electron, which leads to estimation of 0.8% uncertainty for two electrons.

The Z coordinate of the primary vertex has small differences in the distribution between data and MC (see Fig. 14.5). These differences can be eliminated by the reweighting procedure. Since reweighting factors are quite small and have relatively large uncertainty due to imperfection in the description of the Z_{vtx}, differences in C_Z factors between the nominal and reweighted MC are taken as a systematic uncertainties.

The $p_{T,Z}$ distribution of MC@NLO was reweighted (see Sec. 6.5) to PYTHIA, which helped to better describe data. The resulting uncertainty due to this reweighting is about 0.1%.

The opposite charge cut, which was used in the CC analysis is sensitive to the correct modeling of charge misidentification. The charge misidentification can be measured for $Z \to e^+e^-$ events using the tag-and-probe method. The calculation were performed in [2]. The

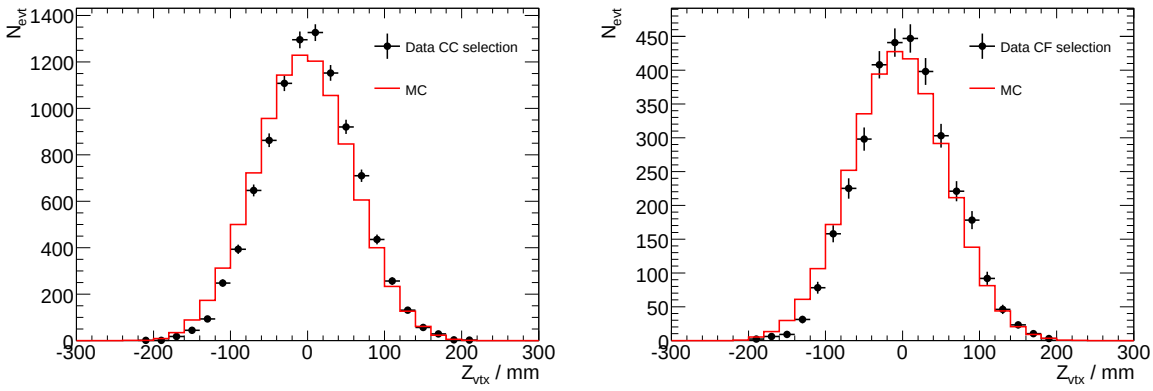

Figure 14.5: The Z coordinate of the primary vertex for the CC (left) and CF (right) selections.

$\|y_Z\|$ bin	E-scale	E-res	$\varepsilon^{\text{Reco}}$	ε^{ID}	$p_{T,Z}$	Trig.	OTX	Z_{vtx}	pileup	MC1	MC2	PDFs	ChMID
0.00 - 0.40	0.1	0.0	1.6	1.4	0.0	0.0	0.8	0.0	0.3	0.1	-0.0	0.2	-0.2
0.40 - 0.80	0.2	0.0	1.6	1.5	0.0	0.0	0.8	-0.0	0.3	0.4	-0.2	0.2	-0.3
0.80 - 1.20	0.2	-0.0	1.6	1.6	0.1	0.0	0.8	0.0	0.3	0.5	-0.8	0.2	-0.5
1.20 - 1.60	0.1	-0.0	1.6	1.9	0.1	0.0	0.8	0.2	0.3	0.4	-0.2	0.2	-0.9
1.60 - 2.00	0.1	-0.0	1.6	2.2	0.0	0.0	0.8	0.3	0.3	0.1	0.6	0.2	-1.2
2.00 - 2.40	0.1	-0.0	1.6	2.9	0.1	0.0	0.8	0.2	0.3	0.6	0.5	0.2	-1.9

Table 14.5: Correlated systematic uncertainties (in %) for the differential $|y_Z|$ measurement for the CC analysis. The sources of the systematic uncertainties are TG efficiency, electron reconstruction efficiency, ID efficiency (statistical and systematic components), energy scale, energy resolution, pileup, OTX, description of the Z vertex shape, description of Z transverse momentum distribution ($p_{T,Z}$), comparison of MC@NLO+Herwig with PowHeg+Herwig (MC1), comparison of PowHeg+Herwig with PowHeg+Pythia (MC2), input PDFs variation by reweighting, charge misidentification (ChMID).

values increased from 0.5% for the central η_e up to 7% for $\eta_e = 2.5$. This effect leads to an uncertainty of about 0.6% for integrated cross section and from 0.2% to 1.9% for the differential cross section.

In order to estimate the uncertainty for modeling NLO effects an MC@NLO sample with Herwig parton showers has been compared to PowHeg simulation interfaced with Herwig showers. This uncertainty is up to 1.4% for higher $|y_Z|$ and about 0.42% for the total cross section. The simulation results of PowHeg interfaced to Herwig and Pythia generators were compared for estimation of uncertainty due to parton showering. This variation gives 0.26% uncertainty.

14.2.4 $Z \to e^+e^-$ systematic uncertainties for the CF selection

A summary of the systematic uncertainties for the CF analysis is presented differentially in Tabs. 14.8 (correlated uncertainties) and 14.9 (uncorrelated uncertainties) and integrated in Tab. 14.10.

$\|y_Z\|$ bin	$\varepsilon_{\mathrm{ID}}$
0.00 - 0.40	0.7
0.40 - 0.80	0.8
0.80 - 1.20	0.8
1.20 - 1.60	0.8
1.60 - 2.00	0.8
2.00 - 2.40	1.0

Table 14.6: Uncorrelated systematic uncertainties (in %) for the differential $|y_Z|$ measurement for the CC analysis.

Systematic name	$\Delta C_Z/C_Z$ [%]
TG efficiency	< 0.1
reconstruction efficiency	1.63
ID efficiency correlated	1.7
ID efficiency uncorrelated	0.44
Energy scale	0.18
Smearing	< 0.1
Pileup	0.3
OTX	0.8
Z vertex shape	0.08
Boson $p_{T,Z}$	< 0.01
Charge MisID	0.6
MC@NLO vs POWHEG	0.29
POWHEG-HERWIG vs PYTHIA	0.04
Total Syst	2.58

Table 14.7: Summary of uncertainties (in %) on C_Z for the CC analysis.

$\|y_Z\|$ bin	E_{scale}	E_{res}	Rec.	$\varepsilon^{\text{ID}}_{\text{Center}}$	$p_{T,Z}$	Trig.	OTX	Z_{vtx}	pileup	MC1	MC2	PDFs	ε^{Iso}	$\varepsilon^{\text{ID}}_{\text{EMEC}}$	$\varepsilon^{\text{ID}}_{\text{FCAL}}$
1.20 - 1.60	1.6	-0.4	0.8	0.7	0.4	0.4	0.8	0.2	0.6	0.5	-0.2	0.2	0.2	5.3	0.0
1.60 - 2.00	0.6	-0.1	0.8	0.8	0.5	0.4	0.8	0.2	0.6	-0.1	1.3	0.2	0.2	5.3	0.0
2.00 - 2.40	1.1	-0.1	0.8	1.3	0.3	0.4	0.8	0.3	0.6	0.3	-0.2	0.2	0.2	4.7	1.0
2.40 - 2.80	1.1	-0.0	0.8	1.2	0.3	0.4	0.8	0.3	0.6	-0.4	-0.2	0.2	0.3	3.2	3.0
2.80 - 3.60	2.5	-0.1	0.8	1.2	0.6	0.4	0.8	0.3	0.6	-1.2	0.3	0.2	0.4	0.1	7.5

Table 14.8: Correlated systematic uncertainties (in %) for the differential $|y_Z|$ measurement for the CF analysis. The sources of the systematic uncertainties are TG efficiency, electron reconstruction efficiency, ID efficiency (statistical and systematic components, for central electrons, EMEC and FCAL separately), energy scale, energy resolution, pileup, OTX, Iso efficiency (statistical and systematic components), description of the Z vertex shape, description of Z transverse momentum distribution ($p_{T,Z}$), comparison of MC@NLO+Herwig with PowHeg+Herwig (MC1), comparison of PowHeg+Herwig with PowHeg+Pythia (MC2) and variation of input PDFs.

Mostly, the sources of systematic uncertainties for the CF analysis are similar to these in the CC analysis. Namely, similar uncertainties are provided by the electron energy smearing, OTX, Z position of primary vertex distribution, MC generators and PDFs. Larger effect (compared to the CC case) comes from reweighting the $p_{T,Z}$ distribution and pileup reweighting. Electron energy calibration also gives a larger effect, since the uncertainties of the calibration correction factors for the forward electron are larger.

Since the TG covers only the central part of the detector, only one of two electrons could be triggered for the CF analysis. Therefore uncertainty due to the TG efficiency correction starts to play a role. An uncertainty of 0.4% is added to the list of systematic uncertainties.

The uncertainty of the electron reconstruction efficiency SF comes from the track-cluster matching in the central part of the calorimeter. Since there is no tracking for the forward part of the calorimeter, no correction is applied. Therefore the total uncertainty due to the electron reconstruction efficiency correction is assumed to be equal to the uncertainty for the central electrons.

Systematic uncertainties of the electron ID efficiency SFs for the central detector, EMEC-IW and FCAL are all propagated separately. These uncertainties in total provide dominant contribution for C_Z systematic uncertainties due to the large background contamination in the forward region.

The systematic uncertainties due to Iso efficiency corrections for the central electron are propagated in the same way as the ID efficiency corrections.

14.2.5 Systematic uncertainties of A_Z and extrapolation factors

The systematic uncertainties of A_Z and the extrapolation factor E are purely theoretical (they depend only on generated information). Several sources of uncertainties are described in the following items:

- The uncertainty within the PDFs set.
- Differences between different PDFs sets. Both A_Z and E were calculated using MC@NLO

$\|y_Z\|$ bin	$\varepsilon^{\mathrm{ID}}$	$\varepsilon^{\mathrm{Iso}}$
1.20 - 1.60	2.6	0.328
1.60 - 2.00	2.5	0.246
2.00 - 2.40	2.4	0.307
2.40 - 2.80	2.5	0.605
2.80 - 3.60	3.1	0.788

Table 14.9: Uncorrelated systematic uncertainties (in %) for the differential $|y_Z|$ measurement for the CF analysis.

Systematic name	$\Delta C_Z/C_Z$ [%]
TG efficiency	0.40
Boson Pt Reweighting	0.41
vertex Z position reweighting	0.27
reconstruction efficiency	0.82
ID efficiency Uncorr	2.27
ID efficiency Central	1.14
ID efficiency EMEC-IW	3.60
ID efficiency FCAL	2.48
Iso efficiency	0.30
Iso efficiency UnCorr	0.26
Energy scale	1.30
Smearing	0.09
Pileup	0.60
PDFs	0.20
OTx	0.80
MC@NLO vs POWHEG-HERWIG	0.36
POWHEG-HERWIG vs POWHEG-PYTHIA	0.28
Total Syst	5.45

Table 14.10: Summary of the uncertainties (in %) on C_Z for the CF analysis.

	PDF unc.	PDF diff.	MC@NLO vs POWHEG	POWHEG JIMMY vs POWHEG PYTHIA
CC selection	1.4	0.6	0.2	0.7
CF selection	1.4	0.7	0.4	0.8

Table 14.11: Systematic uncertainties (in %) for integrated A_Z for the CC and CF selections.

$\|y_Z\|$ bin	PDF unc.	PDF diff.	MC@NLO vs POWHEG	POWHEG JIMMY vs POWHEG PYTHIA
0.00 - 0.40	0.01	0.02	0.01	-0.02
0.40 - 0.80	0.01	0.03	0.07	-0.11
0.80 - 1.20	0.01	0.03	-0.17	0.10
1.20 - 1.60	0.03	0.01	0.43	-0.11
1.60 - 2.00	0.05	0.04	0.67	0.39
2.00 - 2.40	0.13	0.12	1.96	-0.10

Table 14.12: Systematic uncertainties (in %) for differential E for the CC selection.

sample with CTEQ6.6NLO PDFs. PDFs reweighting was used to obtain the other PDFs, such as: ABKM095fl, HERA-PDF10, MSTW2008, CT10, CT10W and NNPDF2.1.

- Differences between generators, which were calculated using MC@NLO and POWHEG.
- Differences in parton shower modeling, which were estimated as differences in results obtained by POWHEG interfaced to PYTHIA and POWHEG interfaced to HERWIG/JIMMY.

The results for the integrated calculation of A_Z are presented in Tab. 14.11 and for the differential calculation of E in Tabs. 14.12 and 14.13 for the CC and CF selections respectively.

$\|y_Z\|$ bin	PDF unc.	PDF diff.	MC@NLO vs POWHEG	POWHEG JIMMY vs POWHEG PYTHIA
1.20 - 1.60	0.19	0.18	-1.33	-0.42
1.60 - 2.00	0.09	0.07	-0.70	-0.40
2.00 - 2.40	0.06	0.05	-1.11	-0.06
2.40 - 2.80	0.03	0.06	-0.01	0.01
2.80 - 3.60	0.43	0.59	0.69	0.08

Table 14.13: Systematic uncertainties (in %) for differential E for the CF selection.

data	9725.0 ± 98.6
QCD bkg.	$163.0 \pm 12.8 \pm 65.2$
EW bkg.	$45.7 \pm 1.0 \pm 2.7$
A_Z	$0.445 \pm 0.0001 \pm 0.009$
C_Z	$0.617 \pm 0.0002 \pm 0.017$

Table 14.14: Number of Z boson candidates, QCD and EW background, A_Z and C_Z for the cross-sections calculation in the $Z \to e^+e^-$ CC channel. The first uncertainty is statistical, while the second is systematic.

	central value [pb] $\pm$ stat $\pm$ syst $\pm$ lumi
σ_{total}	$955.8 \pm 9.7 \pm 33.0 \pm 32.5$
σ_{fidu}	$425.6 \pm 4.3 \pm 12.0 \pm 14.5$

Table 14.15: The integrated total and fiducial cross sections with statistical, systematic and luminosity uncertainties for the CC analysis.

14.3 Cross-section results

14.3.1 $Z \to e^+e^-$ CC Measurement

Fig. 14.6 shows good agreement between the data and MC for the fiducial and combination (defined in Sec. 7.1) cross sections in y_Z bins.

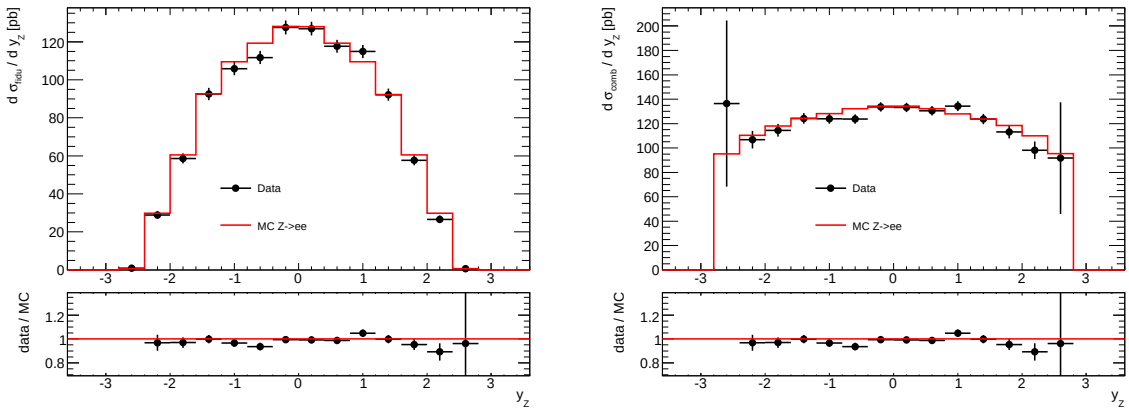

Figure 14.6: Fiducial and combination cross sections for the CC analysis. Symbols with error bars represent background subtracted data with statistical uncertainties. Lines show predictions of MC@NLO simulation.

The main results for the integrated total and fiducial cross-section measurements (see Eq.7.1) are presented in Tab. 14.14. The values for these cross sections are presented in Tab. 14.15.

The fiducial and combination cross sections as a function of $|y_Z|$ are shown in Fig. 14.7. The values are presented in Tab. 14.16.

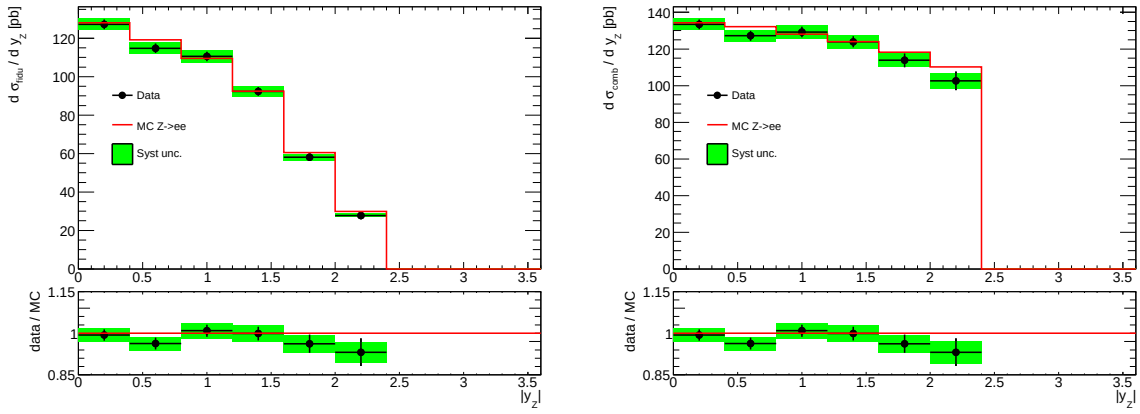

Figure 14.7: Fiducial (left) and combination (right) cross sections as a function of absolute di-electron rapidity $|y_Z|$ for the CC analysis. Symbols with error bars represent background subtracted data with statistical uncertainties. Lines show predictions of MC@NLO simulation.

$\|y_Z\|$	σ_{fidu} [pb]	σ_{comb} [pb]
0.00 - 0.40	$127.2 \pm 2.6 \pm 3.3$	$133.5 \pm 2.7 \pm 3.4$
0.40 - 0.80	$114.8 \pm 2.4 \pm 3.1$	$127.2 \pm 2.7 \pm 3.4$
0.80 - 1.20	$110.5 \pm 2.4 \pm 3.1$	$129.3 \pm 2.9 \pm 3.7$
1.20 - 1.60	$92.4 \pm 2.3 \pm 2.8$	$123.9 \pm 3.1 \pm 3.7$
1.60 - 2.00	$58.2 \pm 1.9 \pm 1.9$	$113.8 \pm 3.7 \pm 3.7$
2.00 - 2.40	$27.8 \pm 1.4 \pm 1.1$	$102.6 \pm 5.1 \pm 4.1$

Table 14.16: Fiducial and combination cross sections in the $Z \to e^+e^-$ CC channel. The first uncertainty is uncorrelated between $|y_Z|$ bins while the second one is correlated.

14.3.2 $Z \to e^+e^-$ CF Measurement

Fig. 14.8 shows a consistent agreement within the statistical uncertainties between data and MC for the fiducial and combination cross sections in full y_Z bins.

Tab. 14.17 presents the main results for the integrated total and fiducial cross-section measurements. The values for these cross sections are presented in Tab. 14.18.

The fiducial cross section and extrapolated combination cross section as a function of $|y_Z|$ are shown in Fig. 14.9. The values for the cross sections are presented in Tab. 14.19. The result shows some discrepancy between data and MC for the bin $1.2 < |y_Z| < 1.6$ which could be due to large systematic uncertainties.

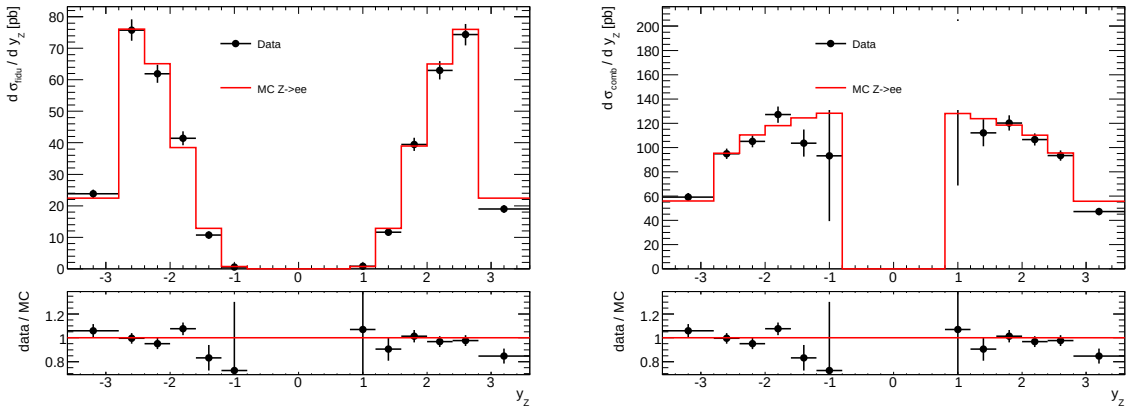

Figure 14.8: Fiducial and combination cross sections in the CF analysis. Symbols with error bars represent background subtracted data with statistical uncertainties. Lines show predictions of MC@NLO simulation.

data	3377.0 ± 58.1
QCD bkg.	$335.0 \pm 27.5 \pm 65.0$
EW bkg.	$63.1 \pm 2.3 \pm 3.4$
A_Z	$0.198 \pm 0.0003 \pm 0.004$
C_Z	$0.441 \pm 0.0002 \pm 0.024$

Table 14.17: Number of Z boson candidates, QCD and EW background, A_Z and C_Z for the cross-sections calculation in the $Z \to e^+e^-$ CF channel. First uncertainty is statistical, while the second is systematic.

14.4 Cross-section combination

The combination of the $Z \to e^+e^-$ CC and CF analyses is presented here, as well as their combination with the $Z \to \mu\mu$ analysis, providing average numbers with smaller systematic uncertainty. The combination performs a test of compatibility. To make a combination of these measurement with a minimum theoretical uncertainty all analyses were performed in the same $|y_Z|$ bins. The common combination phase space:

- $E_{T,l} > 20$ GeV for both leptons

	central value [pb] $\pm$ stat $\pm$ syst $\pm$ lumi
σ_{total}	$939.4 \pm 16.2 \pm 57.7 \pm 31.9$
σ_{fidu}	$186.5 \pm 3.2 \pm 10.8 \pm 6.3$

Table 14.18: The integrated fiducial and total cross sections with statistical, systematic and luminosity uncertainties are calculated for the CF analysis.

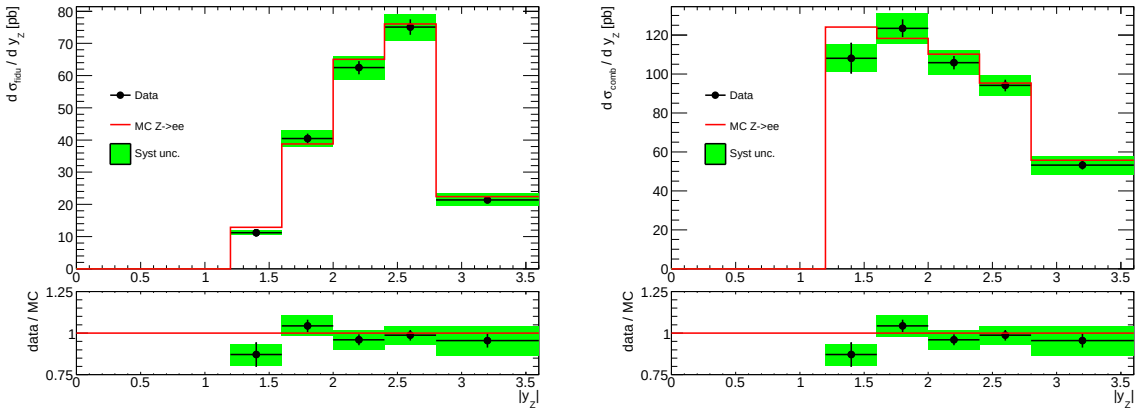

Figure 14.9: Fiducial (left) and combination (right) cross sections as a function of absolute di-electron rapidity $|y_Z|$ for the CF analysis. Symbols with error bars represent background subtracted data with statistical uncertainties. Lines show predictions of MC@NLO simulation.

$\lvert y_Z \rvert$	σ_{fidu} [pb]	σ_{comb} [pb]
1.20 - 1.60	$11.2 \pm 0.8 \pm 0.8$	$108.1 \pm 7.9 \pm 7.4$
1.60 - 2.00	$40.4 \pm 1.5 \pm 2.8$	$123.5 \pm 4.6 \pm 8.4$
2.00 - 2.40	$62.5 \pm 2.0 \pm 3.9$	$105.8 \pm 3.5 \pm 6.6$
2.40 - 2.80	$75.1 \pm 2.4 \pm 4.3$	$94.1 \pm 3.0 \pm 5.4$
2.80 - 3.60	$21.4 \pm 0.9 \pm 2.0$	$53.2 \pm 2.2 \pm 4.9$

Table 14.19: Fiducial and combination cross sections in the $Z \to e^+e^-$ CF channel. The first uncertainty is uncorrelated between $|y_Z|$ bins while the second one is correlated.

- $66 < m_{ll} < 116$ GeV

as discussed in Sec. 7.1 is used for all analyses.

14.4.1 Method description

Combinations of several cross sections are performed taking into account all sources of correlated and uncorrelated uncertainties. This was done using code originally developed for the HERA experiment [81] which was also used for combination of the $p_{T,Z}$ spectra [1].

Common average values m_i for all channels l for each bin i can be found by the χ^2 minimization method. The χ^2 is defined as:

$$\chi^2 = \sum_{i,j} \frac{[m^i - \sum j\gamma^i_{j,l} m^i b_j - \mu^i_l]^2}{\delta^2_{i,stat,l}\mu^i_l(m^i - \sum j\gamma^i_{j,l} m^i b_j) + (\delta_{i,uncor,l} m^i)^2} + \sum_i b_j^2. \tag{14.2}$$

Here i, l and j runs over bins, channels and systematic uncertainties respectively. μ^i_l is a measured value of the cross section in bin i of channel l. $\gamma^i_{j,l}$, $\delta_{i,stat,l}$, $\delta_{i,uncor,l}$ are relative correlated systematic, relative statistical and relative uncorrelated systematic uncertainties, respectively.

14.4.2 Combination result

The combined electron CC and CF cross sections are presented in Tab. 14.20. Tab. 14.21 shows the combination of the electron and muon channels (the cross section in muon channel was calculated only in the central region). All results are in good agreement with total $\chi^2/dof = 11.5/9$, and $\chi^2/dof = 4.19/3$ for electron channels separately.

Fig. 14.10 shows the combined cross sections for the CC and CF electron channels only (left) and for the electron and muon channels together (right).

$\lvert y_Z \rvert$ Bin	σ_{comb} [pb]	Uncor. Unc.	Corr. Unc.	Total Unc.
0.40 - 0.00	133.9	2.9	3.1	4.3
0.80 - 0.40	127.6	2.9	3.1	4.3
1.20 - 0.80	129.8	3.0	3.4	4.6
1.60 - 1.20	122.6	3.0	3.3	4.5
2.00 - 1.60	116.6	3.3	3.4	4.7
2.40 - 2.00	104.4	3.6	3.4	5.0
2.80 - 2.40	93.8	4.2	3.9	5.7
3.60 - 2.80	53.2	3.1	4.4	5.4

Table 14.20: The combined cross section for the CC and CF electron channels in $|y_Z|$ bins.

$\lvert y_Z \rvert$ Bin	σ_{comb} [pb]	Uncor. Unc.	Corr. Unc.	Total Unc.
0.40 - 0.00	129.4	2.0	1.4	2.5
0.80 - 0.40	129.5	2.0	1.5	2.5
1.20 - 0.80	126.4	2.0	1.2	2.3
1.60 - 1.20	119.1	2.0	1.2	2.3
2.00 - 1.60	113.1	2.2	1.5	2.7
2.40 - 2.00	104.5	2.9	2.2	3.7
2.80 - 2.40	92.8	4.2	3.5	5.5
3.60 - 2.80	53.0	3.1	4.3	5.3

Table 14.21: The combined cross section for both CC and CF electron channels together with the muon channel in $|y_Z|$ bins.

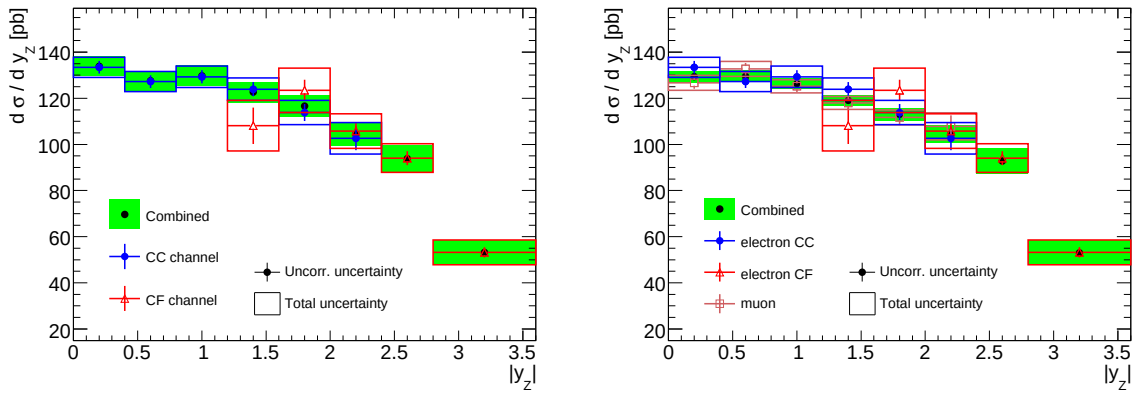

Figure 14.10: The combined cross section for the CC and CF electron channels (left) and electron-muon channels combination (right).

14.5 Comparison with theory

14.5.1 Method description

The calculation of the cross section for Z boson production in pp collisions can be factorized into hard subprocess and PDFs:

$$d\sigma = \int_{\Gamma} \sum_{p} \sum_{f_1,f_2} d\Gamma(\alpha_s(Q^2))^p q_{f_1}(x_1,Q^2) q_{f_2}(x_2,Q^2) \hat{\sigma}_{f_1,f_2}(x_1,x_2,Q^2), \tag{14.3}$$

where Γ is a phase space, $\hat{\sigma}_{f_1,f_2}(x_1,x_2,Q^2)$ is a cross section of the hard subprocess, q_{f_1} and q_{f_2} are PDFs of the quarks f_1 and f_2 respectively, $\sum_p$ runs over all orders of the perturbation theory and $\sum_{f_1,f_2}$ runs over all possible subprocesses. The integration over the phase space is generally achieved numerically by summation over hard subprocess event weights sampled from the phase space,

$$d\sigma = \sum_{p} \sum_{f_1,f_2} \sum_{m=1}^{N} w_{m,f_1,f_2}(x_{1m},x_{2m},Q_m^2)^{(p)} (\alpha_s(Q^2))^p q_{f_1}(x_{1m},Q_m^2) q_{f_2}(x_{2m},Q_m^2). \tag{14.4}$$

Some symmetries in the hard process are used to replace the summation over the 13×13 possible initial state parton products, with a summation over a smaller number of their linear combination. The weights are calculated using matrix elements taking from MCFM program [82].

For the following calculation the APPLgrid program interfaced to the MCFM programs were used. The APPLgrid approach [83] is to store the weights generated in the integration over the phase space in a grid and perform the convolution with PDFs externally. The grid should be created for each analysis bin separately.

The grid calculation was performed on the farm. Statistical uncertainties were estimated by the toy MC method, which was also used for the uncertainty estimation of the calibration (see Sec. 12.1). For this estimation, the grid was calculated several (∼50) times with different seed random numbers. The uncertainties are estimated as the standard deviation of the cross

sections, calculated using these grids. Fig. 14.11 shows the result of this calculation. The statistical uncertainty of the MCFM predictions is about 0.2% for each bin in y_Z.

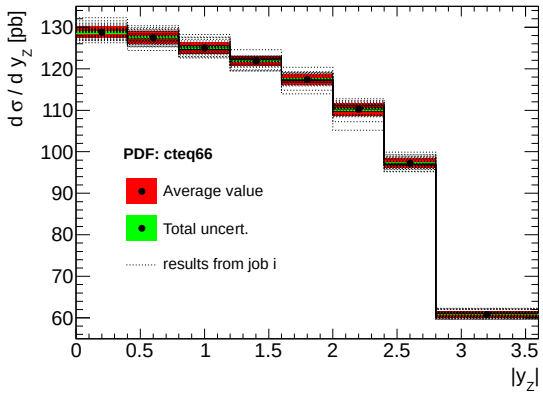

Figure 14.11: Cross sections of the $Z \to e^+e^-$ process in $|y_Z|$ bins, which were calculated 50 times using APPLgrid with different seed numbers. The red band shows average values with statistical uncertainties.

14.5.2 Results

The APPLGRID tables were used to calculate cross-section predictions using CTEQ6.6 and HERAPDF1.0 PDF sets. Fig. 14.12 presents a comparison between the combined electron and muon channel cross section, and the theoretical calculated values. Compared to HERAPDF1.0, CTEQ predictions show a better agreement. The shape of the y_Z rapidity distribution depends on contributions from various quark densities, see Fig. 2.7. In particular, the strange sea quark density has relatively large impact on the distribution and its contribution is relatively poorly constraint. Indeed, a comparison of the PDF decomposition of the HERAPDF1.0 and CTEQ6.6 sets show that the later has significantly higher strange sea density which is preferred by the ATLAS data.

The sensitivity of the Z cross-section measurement to the PDF decomposition was explored further by a dedicated QCD analysis of the HERA and ATLAS data, performed using HERAFitter package [84]. The PDF fits are performed to the combined Z as well as W data. This analysis shows that the ATLAS have novel sensitive to the strange density [85]. The maximum sensitivity of the ATLAS data is reached at $y_Z = 0$ which corresponds at leading order to $x = M_Z/\sqrt{s} = 0.013$ for $Q^2 = M_Z^2$. The ATLAS result is expressed in terms of the ratio $R = 0.5(s + \bar{s})/\bar{d}$ which provides relative suppression of the strange to down sea quark density. The ATLAS data supports un-suppressed strangeness:

$$R = 1.00^{+0.09}_{-0.10} \tag{14.5}$$

where the uncertainty includes data and theoretical uncertainty. The large strange density supports models in which the sea density is flavour symmetric at low x.

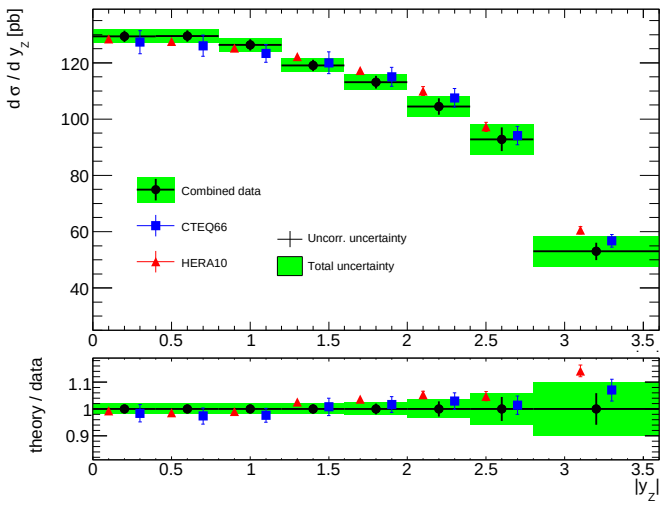

Figure 14.12: Comparison between the combined electron and muon channel cross section with the theoretically calculated values.The CTEQ6.6 and HERAPDF10_EIG PDFs were used for theoretical calculations.

CHAPTER 15

Summary

In this thesis an analysis of $Z \to e^+e^-$ data collected with ATLAS detector at the LHC in 2010 with an integrated luminosity of 36.2 pb^{-1} was presented. The cross-section measurement are presented in both CC and CF channels.

The calibration of EM calorimeter was performed in η_e bins with 0.5% statistical uncertainty and up to 2% systematic uncertainty. The dominant systematic uncertainty comes from the energy linearity and from extra material in the detector. The systematic uncertainty of the cross section due to the energy calibration is significant only for the CF analysis, while the values for the CC analysis are about 0.1%.

Efficiency corrections included corrections for the TG, electron reconstruction, ID and Iso efficiencies. Calculations of the electron ID and Iso corrections were presented. The main uncertainty comes from the background estimation. The ID efficiency correction leads to the dominant systematic uncertainties on the cross section in both CC and CF selections.

Several methods of background subtraction were described. The shape of the QCD background was studied using data with selection, suppressing the signal contamination. Precise background estimation is essential for cross-section calculation and efficiency measurement as well. Large background fractions and small statistics for the CF analysis lead to large systematic uncertainties on the cross section.

Comparisons of different MC generators with different PDFs and different shower models were presented. The cross-section systematic uncertainty due to MC differences is not small and could be dominant for analysis of future data.

Several other sources of the cross-section systematic uncertainties were studied as well. An imperfect description of data resolution, the pileup modeling and the modeling of the problematic regions of the EM calorimeter have small but not negligible contribution to the systematic uncertainties.

Finally the cross-section measurement is presented inclusive and single differentially in $|y_Z|$ in fiducial and combination volumes. Both CC and CF cross sections are in good agreement with MC calculation. The combination of the CC and CF results provides a test of compatibility and shows agreement with the muon channel measurement was obtained.

The combined results obtained from the electrons and muon channels can be used for PDFs

fits.

Bibliography

[1] [ATLAS Collaboration], *Measurement of the transverse momentum distribution of Z bosons in pp collisions at $\sqrt{s} = 7$ TeV with the ATLAS detector*, Phys. Lett. **B705** (2011) 415–434, `arXiv:1107.2381 [hep-ex]`. 2, 39, 119

[2] [ATLAS Collaboration], *Electron performance measurements with the ATLAS detector using the 2010 LHC pp collision data*, Eur. Phys. J. **C72** (2012) 1909, `arXiv:1110.3174 [hep-ex]`. 2, 47, 48, 50, 77, 85, 89, 95, 99, 110

[3] [ATLAS Collaboration], *Measurement of the inclusive $W^{\pm}$ and Z cross sections in the electron and muon decay channels in pp collisions at $\sqrt{s} = 7$ TeV with the ATLAS detector*, `arXiv:1109.5141 [hep-ex]`. 30 pages (43 including author list), 19 figures, 26 tables, final version to appear in Phys. Rev. D. 2

[4] F. Yndurain, *The theory of quark and gluon interactions*. Springer, 2006. Fourth Edition. 3, 8

[5] M. Peskin and D. Schroeder, *An introduction to quantum field theory*. Addison-Wesley, 1995. 3

[6] S. Weinberg, *The quantum theory of fields*. University of Texas at Austin, 1995. 5

[7] F. Halzen and A. Martin, *Quarks and leptons: An introductory course in modern particle physics*. Wiley, 1984. 5

[8] C. Yang and R. Mills, *Conservation of isotopic spin and isotopic gauge invariance*, Phys. Rev. **96** (1954) 191–195. 5

[9] M. Gell-Mann, *A schematic model of baryons and mesons*, Phys. Lett. **8** (1964) 214–215. 5

[10] N. Bogolubov, B. Struminsky, and A. Tavkhelidze, *On composite models in the theory of elementary particles*, JINR Preprint D-1968 (Dubna, 1965) . 5

[11] O. Greenberg, *Spin and unitary spin independence in a paraquark model of baryons and mesons*, Phys. Rev. Lett. **13** (1964) 598–602. 5

[12] K. Wilson, *Confinement of quarks*, Phys. Rev. D **10** (Okt, 1974) 2445–2459. 5

[13] J. Goldstone, A. Salam, and S. Weinberg, *Broken symmetries*, Phys. Rev. **127** (1962) 965–970. 5

[14] P. Higgs, *Broken symmetries and the masses of gauge bosons*, Phys. Rev. Lett. **13** (1964) 508–509. 5

[15] [Particle Data Group], *Particle physics booklet*, Journal of Physics G: Nuclear and Particle Physics **37** (2010) no. 7A, . Review of Particle Physics: The 2010 edition is published for the Particle Data Group as article number 075021 in volume 37 of Journal of Physics G: Nuclear and Particle Physics. 5, 6

[16] G. Altarelli and G. Parisi, *Asymptotic freedom in parton language*, Nucl. Phys. **B126** (1977) 298. 6

[17] J. Collins, *Renormalization*. Cambridge university press, 1984. 6

[18] G. 'tHooft and M. Veltman, *Regularization and renormalization of gauge theory*, Nucl. Phys. **B44** (1972) 189–213. 6

[19] R. Feynman, *Very high-energy collisions of hadrons*, Phys. Rev. Lett. **23** (1969) 1415. 7

[20] [H1 Collaboration], *A precision measurement of the inclusive ep scattering cross section at HERA*, The European Physical Journal C **64** (2009) 561–587. 8

[21] M. Bengtsson and T. Sjoestrand, *Parton showers in leptoproduction events*, Z. Phys. **C37** (1988) 465. 8

[22] S. Drell and T. Yan, *Partons and their applications at the high energies*, Annals of physics **66** (1971) 578–623. 8

[23] M. Aharrouche, A. Arbuzov, Bardin, et al., *Double differential Z,W cross sections and their ratios in the electron channels*, Tech. Rep. ATL-COM-PHYS-2010-325, CERN, Geneva, Jun, 2010. 10

[24] H. Bichsel, D. Groom, and S. Klein, *Passage of particle through matter*, Physics letters B **C71** (July 2008) 261–280. 13

[25] M. Davier, *Lepton universality*, Tech. Rep. CERN-OPEN-99-178, LAL-98-68, 1998. 13

[26] C. Lefevre, *LHC: the guide*, Jan, 2008. 15

[27] L. Evans and P. Bryant, *Imaging very high energy gamma-ray telescopes*, JINST **3** (2009) S08001. 16

[28] [ATLAS Collaboration], *Luminosity determination in pp collisions at* $\sqrt{s} = 7$ *TeV using the ATLAS detector at the LHC*, Eur. Phys. J. **C71** (2011) 1630. 16, 33

[29] *Summary of the analysis of the 19 September 2008 incident at the LHC*, tech. rep., CERN, Geneva, Oct, 2008. http://cdsweb.cern.ch/record/1135729/. 16

[30] [ATLAS Collaboration], *Performance of the ATLAS trigger system in 2010*, Eur. Phys. J. C **72** (Oct, 2011) 1849. 17, 34

[31] [ATLAS Collaboration], *Measurement of the rate of collisions from satellite bunches for the April-May 2010 LHC luminosity calibration*, Tech. Rep. ATLAS-CONF-2010-102, CERN, Geneva, Dec, 2010. 16

[32] [ATLAS Collaboration], *Updated luminosity determination in pp collisions at* $\sqrt{s} = 7$ *TeV using the ATLAS detector*, Tech. Rep. ATLAS-CONF-2011-011, CERN, Geneva, Mar, 2011. 16

[33] [ATLAS Collaboration], *ATLAS detector and physics performance: Technical Design Report, 1*, Tech. Rep. ATLAS-TDR-014, CERN-LHCC-99-014, CERN, Geneva. 19

[34] [ATLAS Collaboration], *The ATLAS experiment at the CERN large hadron collider*, JINST **3** (2008) no. 08, S08003. 19, 20, 22, 23, 24, 26, 27, 28

[35] [ATLAS Collaboration], *ATLAS pixel detector electronics and sensors*, JINST **3** (2008) no. 07, P07007. 21

[36] *The expected performance of the ATLAS inner detector*, Tech. Rep. ATL-PHYS-PUB-2009-002, ATL-COM-PHYS-2008-105, CERN, Geneva, Aug, 2008. 21

[37] [ATLAS Collaboration], *ATLAS liquid-argon calorimeter: Technical Design Report*, Tech. Rep. ATLAS-TDR-002, CERN-LHCC-96-041, CERN/LHCC 96-41, CERN, Geneva, 1996. 23

[38] H. Abreu, M. Aharrouche, M. Aleksa, et al., *Performance of the electronic readout of the ATLAS liquid argon calorimeters*, JINST **5** (2010) P09003. 25

[39] [ATLAS Collaboration], *ATLAS trigger performance: Status report*, Tech. Rep. CERN-LHCC-98-015, CERN, Geneva, Jun, 1998. 28, 29

[40] [ATLAS Collaboration], *ATLAS DAQ, EF, LVL2 and DCS: Technical progress report*, Tech. Rep. CERN-LHCC-98-016, CERN, Geneva, Jun, 1998. 28

[41] [ATLAS Collaboration], *Performance of the electron and photon trigger in pp collisions at* $\sqrt{s} = 7$ *TeV with the ATLAS detector at the LHC*, Tech. Rep. ATLAS-CONF-2011-114, CERN, Geneva, Aug, 2011. 30

[42] [ATLAS Collaboration], *Atlas computing : Technical design report*, Tech. Rep. CERN-LHCC-2005-022, CERN, Geneva, Mai, 2005. 30

[43] [LHC committee], *LCG project comprehensive review*, CERN/LHCC 2007-031 (23 November 2007) . 30

[44] [ATLAS Collaboration], *Athena. The ATLAS common framework*, . Developer Guide. version 8. 31

[45] [ROOT team], *ROOT. An object oriented data analysis framework*, http://root.cern.ch/ (December 2009) . User Guide 5.26. 32

[46] W. Verkerke and D. Kirkby, *The RooFit toolkit for data modeling*, ArXiv Physics e-prints , `arXiv:physics/0306116`. 32, 61

[47] P. Waller, *ATLAS data quality monitoring: experience with first collision data*, Tech. Rep. ATL-DAPR-PROC-2010-001, CERN, Geneva, Nov, 2010. 33

[48] T. Sjostrand, S. Mrenna, and P. Z. Skands, *PYTHIA 6.4 Physics and manual*, JHEP **0605** (2006) 026, `arXiv:hep-ph/0603175 [hep-ph]`. 35

[49] G. Corcella, I. Knowles, G. Marchesini, et al., *Herwig 6: an event generator for hadron emission reaction with interfering gluons*, JHEP **01** (Nov, 2000) 010. 35

[50] J. Butterworth, J. R. Forshaw, and M. Seymour, *Multiparton interactions in photoproduction at HERA*, Z. Phys. **C72** (1996) 637–646, `arXiv:hep-ph/9601371 [hep-ph]`. 35

[51] S. Frixione and B. Webber, *The MC@NLO 3.3 event generator*, `arXiv:hep-ph/0612272 [hep-ph]`. 35

[52] S. Alioli, P. Nason, C. Oleari, and E. Re, *NLO vector-boson production matched with shower in POWHEG*, JHEP **0807** (2008) 060. 36

[53] S. Frixione, P. Nason, and G. Ridolfi, *The POWHEG-hvq manual version 1.0*, `arXiv:0707.3081 [hep-ph]`. 36

[54] E. Barberio and Z. Was, *PHOTOS - a universal Monte Carlo for QED radiative corrections: version 2.0*, Computer Physics Communications **79** (1994) no. 2, 291–308. 36

[55] S. Agostinelli, J. Allisonas, and K. Amakoe, *GEANT4 - a simulation toolkit*, Nuclear Instruments and Methods in Physics Research A **506** (2003) 250–303. 37

[56] E. Richter-Was, D. Froidevaux, and L. Poggioli, *ATLFAST 2.0 a fast simulation package for ATLAS*, Tech. Rep. ATL-PHYS-98-131, CERN, Geneva, Nov, 1998. 37

[57] [Atlas Collaboration], *The simulation principle and performance of the ATLAS fast calorimeter simulation FastCaloSim*, Tech. Rep. ATL-PHYS-PUB-2010-013, CERN, Geneva, Oct, 2010. 37

[58] E. Barberio et al., *Fast simulation of electromagnetic showers in the ATLAS calorimeter: Frozen showers*, J. Phys. Conf. **160** (2009) 012082. 37

[59] P. M. Nadolsky et al., *Implications of CTEQ global analysis for collider observables*, Phys. Rev. **D78** (2008) 013004, arXiv:0802.0007 [hep-ph]. 37

[60] A. Martin, W. Stirling, R. Thorne, and G. Watt, *Parton distributions for the LHC*, Eur. Phys. J. **C63** (2009) 189–285, arXiv:0901.0002 [hep-ph]. 37

[61] B. Kersevan and E. Richter-Was., *Processing generated events with TAUOLA and PHOTOS using the Athena interface*, . 37

[62] Z. Was, *TAUOLA the library for tau lepton decay, and KKMC/KORALB/KORALZ/...*, . 37

[63] [ATLAS Collaboration], *ATLAS Monte Carlo tunes for MC09*, Tech. Rep. ATL-PHYS-PUB-2010-002, CERN, Geneva, Mar, 2010. 37

[64] [ATLAS Collaboration], *Charged particle multiplicities in p p interactions at $\sqrt{s}$=0.9 and 7 TeV in a diffractive limited phase-space measured with the ATLAS detector at the LHC and new PYTHIA6 tune*, Tech. Rep. ATLAS-CONF-2010-031, CERN, Geneva, Jul, 2010. 37

[65] [ATLAS Collaboration], *Study of the material budget in the ATLAS inner detector with K0S decays in collision data at $\sqrt{s} = 900$ GeV*, Tech. Rep. ATLAS-CONF-2010-019, CERN, Geneva, Jul, 2010. 37

[66] [ATLAS Collaboration], *Probing the material in front of the ATLAS electromagnetic calorimeter with energy flow from $\sqrt{s} = 7$ TeV minimum bias events*, ATLAS-CONF-2010-037 (2010) . 37

[67] C. Anastasiou, L. Dixon, K. Melnikov, and F. Petriello, *High precision QCD at hadron colliders: electroweak gauge boson rapidity distributions at NNLO*, Phys. Rev. **D69** (2004) 094008. 38

[68] J. Butterworth et al., *Single boson and di-boson production cross sections in pp collisions $\sqrt(s) = 7$ TeV*, ATL-COM-PHYS-2010-695 (2010) . 38

[69] U. Langenfeld, S. Moch, and P. Uwer, *Measuring the running top-quark mass*, Phys. Rev. **D80** (2009) 054009. 38

[70] [ATLAS Collaboration], *Measurement of the Transverse Momentum Distribution of W Bosons in pp Collisions at $\sqrt{s} = 7$ TeV with the ATLAS Detector*, Phys. Rev. **D85** (2012) 012005, arXiv:1108.6308 [hep-ex]. 39

[71] [ATLAS Collaboration], *Reconstruction and identification of electrons*, Tech. Rep. ATL-PHYS-PUB-2009-004, ATL-COM-PHYS-2009-170, CERN, Geneva, Apr, 2009. CSC PUB Note. 47

[72] [ATLAS Collaboration], *Electron and photon reconstruction and identification in ATLAS: expected performance at high energy and results at 900 GeV*, Tech. Rep. ATLAS-CONF-2010-005, CERN, Geneva, Jun, 2010. 47, 48, 50

[73] M. Kuna, *Electron and photon reconstruction and identification with the ATLAS Detector*, Tech. Rep. ATL-GEN-PROC-2010-018, CERN, Geneva, Dec, 2010. 47

[74] *Isolation tool*, https://twiki.cern.ch/twiki/bin/viewauth/AtlasProtected/EgammaIsolationMVATopTool. 50

[75] J. Hartert and I. Ludwig, *Electron isolation in the ATLAS experiment*, Tech. Rep. ATL-COM-PHYS-2010-070, CERN, Geneva, Feb, 2010. 50

[76] *DPD Maker*, https://twiki.cern.ch/twiki/bin/viewauth/AtlasProtected/PrimaryDPDMaker. 51

[77] S. Mehlhase, W. Ehrenfeld, and K. Leffhalm, *The German national analysis facility as a tool for ATLAS analyses*, Tech. Rep. ATL-SOFT-PROC-2011-009, CERN, Geneva, Jan, 2011. 52

[78] *Analysis tool (ZeeD)*, https://wiki-zeuthen.desy.de/ATLAS/Projects/ZeeD. 55

[79] M. Aharrouche, F. Ellinghaus, C. Goeringer, S. Koenig, R. Poettgen, and S. J. Wollstadt, *$Z \to e^+e^-$ cross-section measurement at forward rapidity in pp collisions at $\sqrt{s} = 7$ TeV with the atlas detector*, Tech. Rep. ATL-COM-PHYS-2011-171, 2011. 95, 99

[80] B. Efron, *Bootstrap methods: Another look at the Jackknife*, The Annals of Statistics **7** (1979) 1–26. 107

[81] A. Glazov, *Averaging of DIS cross section data*, AIP Conf. Proc. **792** (2005) 237–240. 119

[82] J. Campbell and R. Ellis., *A Monte Carlo for femtobarn processes at hadron collides (MCFM v5.6)*, . Users Guide. 121

[83] T. Carli, D. Clements, A. Cooper-Sarkar, C. Gwenlan, G. P. Salam, et al., *A posteriori inclusion of parton density functions in NLO QCD final-state calculations at hadron colliders: The APPLGRID Project*, Eur. Phys. J. **C66** (2010) 503–524, `arXiv:0911.2985 [hep-ph]`. 121

[84] *HERAFitter program*, http://herafitter.hepforge.org/. 122

[85] [ATLAS Collaboration], *Determination of the strange quark density of the proton from ATLAS measurements of the $W \to l\nu$ and $Z \to ll$ cross sections*, . Comments: 4 pages plus author list (18 pages total) 3 figures, accepted by Phys. Rev. Lett. 122

Acknowledgements

During the years of my PhD I was surrounded by very nice and interesting people, which were always ready to help me. I would like to acknowledge:

- PD. Dr. Alexandre Glazov for guidance during the years of my PhD,
- PD. Dr. Thomas Schörner-Sadenius für die Übernahme des Zweitgutachtens der Dissertation,
- Prof. Dr. Johannes Haller für die Übernahme des Zweitgutachtens der Disputation.
- My colleagues, who always answering my stupid questions and help me to check the spelling of this thesis (especially: Martin Goebel, Karl-Johan Grahn, James Dassoulas, George Sedov, Pavel Starovoitov, Voica Radescu, Sebastian Schmitt, Ringaile Placakyte, Stanislav Shushkevich, Anastasia Grebenyuk, Alexey Petrukhin)
- Concerning electron identification and reconstruction as well as other question to the ATLAS I thank: Jan Kretzschmar and Mohamed Aharrouche,
- Finally I thank my wife and my parents, which always inspire me.

Many thanks! and Vielen Dank!